Circulation Methods in Unsteady and Three-dimensional Flows

by

Jiankun Yuan

A Dissertation

Submitted to the Faculty

of the

WORCESTER POLYTECNHIC INSTITUTE

In partial fulfillment of the requirements for the

Degree of Doctor of Philosophy

in

Mechanical Engineering

by

_____

March 2002

APPROVED:

_____
Prof. David J. Olinger, Advisor

_____
Prof. Hamid Johari

_____
Prof. James C. Hermanson

_____
Prof. Mikhail Dimentberg

_____
Prof. Peder C. Pedersen

_____
Dr. Thomas J. Gieseke
Naval Undersea Warfare Center
Newport, RI

_____
Prof. Zhikun Hou
Graduate Committee Representative

Dedicated to the memory of my PARENTS

Abstract

The largely unstudied extension of ultrasonic circulation measurement techniques (UCMT) to determine instantaneous lift in unsteady and three-dimensional flows has been addressed in this work. A combined analytical-numerical-experimental approach was undertaken with the goal of developing methods to properly convert the measurable time-dependent bound circulation to instantaneous lift force in unsteady flows. The measurement of *mean* sectional lift distribution along structure spans in three-dimensional flows was also studied.

An unsteady correction method for thin airfoils was developed analytically and validated numerically (with finite element solutions) to properly convert bound circulation to instantaneous lift based on unsteady potential flow theory. Results show that the unsteady correction method can provide increased accuracy for unsteady lift prediction over the Kutta-Joukowski method used in previous unsteady flow studies. The unsteady correction model generally should be included for instantaneous lift prediction as long as the bound circulation is time-dependent.

Using the same framework, we also studied determination of instantaneous lift forces on stationary bluff bodies (circular cylinders) at low Reynolds number (Re=100). Various force models, including an approximate vortex force model, were studied. A new unsteady model, similar to that developed for the thin airfoils, using instantaneous bound circulation values, was proposed.

Another important issue studied in this thesis is the effect of acoustic path sensitivity on bound circulation determination, which we found to be crucial for

accurately predicting the instantaneous lift in both unsteady flat plate and cylinder flows. Proper path selection should take into account the location of boundary layers, attached and shed vortices. These findings will be useful in future experimental design of UCMT, PIV and LDV methods.

Finally, we used the UCMT method to experimentally study the *mean* spatial lift distribution along structures. Low Reynolds number low aspect ratio (AR) wings that have application in micro-aerial-vehicles (MAV) were studied. The spanwise circulation (lift) distribution along the MAV wings exhibits a peak (maximum), and deviates from predictions of Prandtl's lifting line theory. Although only 'linear' lift (due to bound circulation) was measured, comparison with force balance results showed that reasonable integrated lift values on low Re, low AR wings can be obtained using UCMT.

Acknowledgments

I would like to first express my deep gratitude to my advisor, Prof. David J. Olinger, for his excellent guidance and support in the development of this work detailed in this dissertation. Without his outstanding ability as a research advisor, this work would be impossible.

Thanks are also extended to the members of my thesis committee; Prof. Hamid Johari for his useful suggestions in the experimental work, and Prof. James Hermanson, Prof. Mikhail Dimentberg, Prof. Peder C. Pedersen, Dr. Thomas J. Gieseke and Prof. Zhikun Hou for their time and assistance in this work.

I also wish to thank Prof. Andreas N. Alexandrou for his guidance in using the finite element code. Thanks to Ganapathi R. Balasubramanian for help in numerical grid generation. I would like to acknowledge Francis J. Weber and Ken Desabrais for their help in the UCMT experiments. Thanks to Dr. Qingyun Zhang for his help to accommodate the lab work in my first year at WPI.

My eternal gratitude to my parents, my brother and sisters, for their endless love and support, I would not have made it this far without their encouragement. I also wish to acknowledge support from the Office of Naval Research (ONR) under the direction of Dr. Thomas Swean and the Mechanical Engineering Department during this work.

Finally, my deepest thanks to my wife Zhiying Hou and my lovely daughter Lin Yuan for their love, patience and understanding during the past few years. Thanks for their unconditional support and love despite my moods when the stress and intensity of this work overwhelmed me. For this, I will always be deeply indebted.

Table of Contents

List of Figures

$C_l^{(v)}$. Vortex lift is obtained from equation (4.10) within the selected wake domain. Quasi-steady lift is determined from K-J approximation. β is the phase angle between true lift and $C_l^{(1)} + C_l^{(v)}$.

List of Tables

Nomenclature

A	quasi-steady lift
AOA	angle of attack
AR	aspect ratio of finite wings
a	sound speed
B	unsteady lift term
$B^{(2)}$	unsteady lift term for approximation 2
b	span of finite wing
c	plate chord length
$c(z)$	local sectional chord length in experiments
C_l	local sectional lift coefficient for 2D flow or 'true' lift coefficient in numerical work
C_L	total lift coefficient for body in 3D flow
$C_l^{(1)}$	lift coefficient for quasi-steady approximation (1)
$C_l^{(2)}$	lift coefficient for unsteady approximation (2)
$C_l^{(3)}$	lift coefficient for corrected unsteady approximation (3)
$C_l^{(4)}$	lift coefficient including wake vortex lift – cylinder flow
$C_l^{(v)}$	vortex lift coefficient – Lighthill's concept
$C_{lw}^{(v)}$	wake vortex lift coefficient – Lighthill's concept
$\overline{C_l}$	mean lift coefficient
$\overline{C_N}$	mean normal force coefficient on a plate
$C(k)$	lift deficiency factor
d	diameter of circular cylinder
$E_n(t)$	n^{th} coefficient in trigonometry expansion of Glauert approach
$e(t)$	time dependent relative error
$e_{rms}^{(1)}$	root mean square error for $C_l^{(1)}$
$e_{rms}^{(2)}$	root mean square error for $C_l^{(2)}$
$e_{rms}^{(3)}$	root mean square error for $C_l^{(3)}$
$e_{rms}^{(4)}$	root mean square error for $C_l^{(4)}$
$F(t)$	instantaneous force
F_0	force amplitude
F_v	vortex force based on Lighthill's concept
g	gravitational acceleration
H	height of wind tunnel test section
$h(t)$	instantaneous location of oscillating plate

h_0 equilibrium location of the plate

h_a plate oscillation amplitude

K spring stiffness

KC Keulegan-Carpenter number, $KC = 2\pi y_o / d$

k reduced frequency

L 'true' lift force in numerical work

L_0 sectional lift force on plate at constant chord length

$L^{(v)}$ vortex lift based on Lighthill's concept

$L(z)$ local sectional lift force on plate

$L^{(1)}$ lift for quasi-steady approximation (1)

$L^{(2)}$ lift for unsteady approximation (2)

$L^{(3)}$ lift for corrected unsteady approximation (3)

$L^{(4)}$ lift including wake vortex lift – cylinder flow

L_{avg} mean lift

L_{rms} root mean square amplitude of lift force

l_p total length of a closed path

M mass per unit span

NM total element number in computational domain

NND total node number in computational domain

$\vec{n}$ normal vector of surface

p local static pressure in fluids flow

p_∞ static pressure of free-stream

p_l static pressure on lower surface of body

p_u static pressure on upper surface of body

R unsteady correction coefficient

Re Reynolds number

$\vec{r}$ position vector

S integral surface

T_{cw} transient time of a sound pulse along closed path clockwise

T_{ccw} transient time of a sound pulse along closed path counterclockwise

t time

t_c plunging time of a plate

Δt time-step set in numerical simulation

U free-stream velocity

u velocity component in x-direction

$\vec{V}$ local fluid velocity

$\vec{V_0}$ velocity of body reference frame

W width of wind tunnel test section

$W(x,t)$ local downwash

X,Y,Z coordinates in inertia reference frame

x,y,z coordinates in body reference frame

$y(t)$ displacement of body

y_0 body vibration amplitude

z_0 distance in which local chord length varying

Greek Symbols

α angle of attack

α_0 angle of attack - equilibrium state

α_a angle of attack amplitude - pitching plate

β viscous damping coefficient

$\Gamma(t)$ bound circulation

Γ_s circulation measured on closed path enclosing body

Γ_a circulation measured on closed path enclosing wake

Γ_k circulation of the kth vortex in wake

$\Gamma(x,t)$ circulation distribution along plate

$\gamma(x,t)$ local vortex element distribution along plate

ε solid blockage of testing plate

η plate shape function

θ angular coordinate

ρ fluid density

σ stress tensor

τ shear stress

ϕ_2^k phase angle between lift and vortex shedding event

$\overline{\overline{\Theta}}$ tensor related to velocity and its derivatives – Noca's work

Φ velocity potential

Φ_B velocity potential of body

Φ_w velocity potential of wake

$\Delta\Phi^{(1)}$ phase angle between $C_l^{(1)}$ and C_l

$\Delta\Phi^{(2)}$ phase angle between $C_l^{(2)}$ and C_l

$\Delta\Phi^{(3)}$ phase angle between $C_l^{(3)}$ and C_l

Ψ stream function

$\vec{\Omega}$ rate of rotation of body reference frame

$\vec{\omega}$ vorticity

ω angular frequency

Chapter 1

Introduction

1.1 Background

The determination of the lift force on aerodynamic bodies in a fluid flow is of fundamental importance in many engineering applications. These include fluid-structure interaction problems such as the flow-induced vibration of aircraft wings, tall buildings, long bridges, and offshore engineering structures including flexible marine risers, cables and ribbons (Fig.1.1). These flows are characterized by both unsteady effects (oscillation) and three-dimensional spatial variations (along the structure) in the flow. These effects also occur in other flows (pitching airfoils, low aspect ratio wings), making lift measurement under such conditions a topic of general interest. In this research, a sub-class of these flows that exhibit unsteadiness and spatial variation will be studied. These include oscillating flat plate flows, cylinder wake flows and low aspect ratio wings. Though many issues need to be studied for these types of flows, our focus will be mainly on the topic of lift force determination through circulation methods.

Determination of local, unsteady lift force in these flows is critical due to the nonlinear coupling that exists between the structure motion and fluid forces. As shown in Fig 1.2, the motion of the structure influences the flow dynamics in the wake. The flow dynamics, in turn, determine the fluid loading (lift force) and hence the structural motion. As a result, accurate lift determination is a key in modeling of flow-induced vibration. Modeling of this type has been studied by many investigators. Only a brief
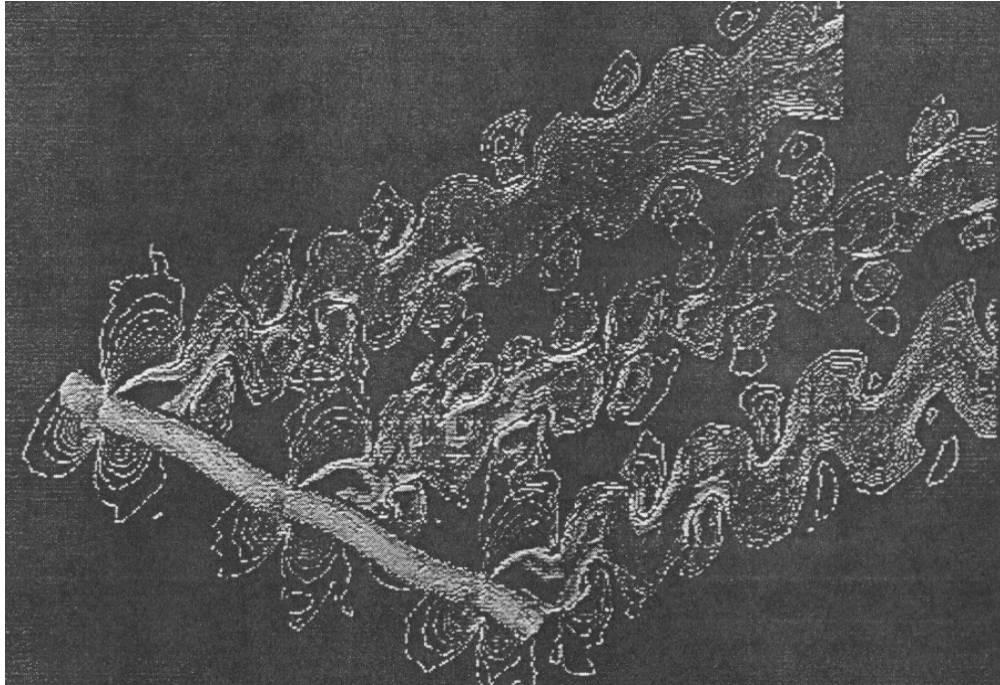
Fig. 1.1 Fluid-cable interaction by direct numerical simulation (Newman & Karniadakis, 1996)
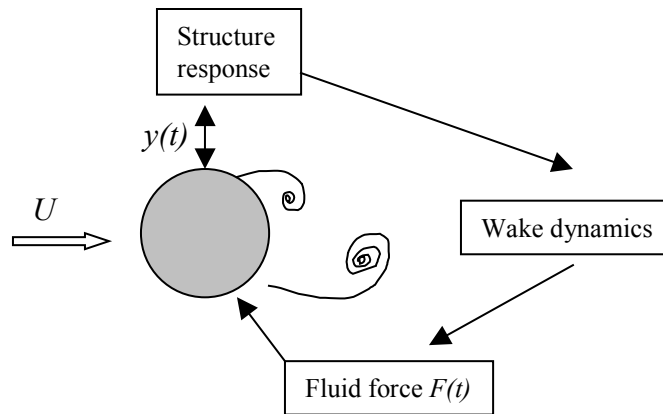
Fig. 1.2 Schematic of nonlinear coupling between fluid force, structural response and fluid loading

summary is given here. Detailed review of flow-induced vibration modeling can be found in Parkinson (1974), Iwan (1975), Blevins (1984), Sarpkaya (1979). For example, a spring-mass modeling system for the coupling between structure motion and the exciting fluid force was studied by Bearman (1984). The model can be expressed as

$$M\ddot{y} + \beta\dot{y} + Ky = F(t). \tag{1.1}$$

where y is the displacement of the body, M the mass per unit span, β the viscous damping coefficient associated with the springs and their mounting, K the stiffness of the springs, $F(t)$ the time-dependent fluid force. Physically, when a body is responding to vortex shedding, the fluid force must lead the excitation by some phase angle ϕ. The displacement and force $F(t)$ can be presented as

$$y = y_o \sin(\omega t); \quad F(t) = F_o \sin(\omega t + \phi). \tag{1.2}$$

where y_o is the body vibration amplitude, F_o the fluid force amplitude. As a result, accurate determination of lift amplitude F_o and phase angle ϕ are critical for modeling of flow-induced vibration.

Recently, Olinger (1998) developed a low-order dynamic model, based on circle maps, to study the dynamics of oscillating flexible cables. A spatial-temporal map lattice was used to predict the vortex shedding patterns and wake dynamics.

$$\frac{\partial^2 y}{\partial^2 t} = c^2 \frac{\partial^2 y}{\partial^2 z} + \frac{2C_l}{\pi\rho}\sin(2\pi\theta_n^k + \phi_n^k). \tag{1.3}$$

Here C_l is the fluid-induced lift force, ϕ_n^k is the phase between vortex shedding event and the lift force. As in the more traditional models described above, phase angle determination is again a critical element.

3

Lift determination is also important for study of three-dimensional spatial flow variations along the body span. Fluid-cable interaction is one of the cases that involve the spanwise variation of vortex shedding patterns and fluid forces. Ramberg and Griffin (1976) studied the effect of vortex coherence on flow-induced forces on vibrating cables. Newman and Karniadakis (1996) utilized a parallel spectral element Fourier method to numerically study the flow over a flexible oscillating cable at laminar and transitional Reynolds numbers. They quantified and compared the coupled cable-flow response for both forced and flow-induced cable vibrations. Three-dimensional patterns were also observed in the wake of two-dimensional bluff bodies (Triantafyllou, 1990). One such mechanism includes the three-dimensional patterns resulted from a two-dimensional non-uniformity, such as the spanwise variation in body sectional size (Nuzzi et al, 1992). Spatial lift distributions in a similar flow, a flat plate with an imposed spanwise chord non-uniformity will be described in later sections (Yuan and Olinger, 1999). Details of the three-dimensional patterns generated from two-dimensional bluff bodies were summarized in Williamson (1996).

Finally, lift force determination is directly related to the structural stress and moment distributions at each spanwise sectional location. Fundamental understanding of lift force on structures will be beneficial in the design and construction of structures that are safe, functional, economical and able to resist impact from the environment over a required period.

The fluid forces exerting on body immersed in a flow are derived from two sources: the normal pressure distribution exerted over the surface of the body and the

tangential shear stress distribution over the surface. The resultant force on a body can be decomposed into lift (transverse force) and drag (in-line force), relative to the flow direction over the body. Lift is defined as the force component perpendicular to the flow direction, and drag is the component parallel to the flow direction. In this work, we focus on the lift force. While experimental techniques exist to measure the time-average mean lift on structures, little effort has been placed on accurate, non-intrusive techniques to measure the instantaneous lift at each local section in these types of flows. This will be a focus in this thesis. The main goal is to address certain aspects of these issues through extension of the ultrasonic circulation measurement technique (UCMT) developed by Schmidt (1970, 1975) and Johari & Durgin (1998), to study unsteady and spatially varying flows. Details of UCMT will be described in a later section.

1.2 Review

Traditional research efforts in fluid dynamics generally can include three aspects; theoretical work based on mathematical description of physical phenomena leading to governing equations of fluid motion, experimental study, and numerical simulation of the theoretical governing equations. In the following literature review, we will focus primarily on the theoretical and experimental investigations on lift determination. However, we will also focus briefly on certain numerical techniques, namely discrete vortex methods, when necessary to understand important theoretical aspects of lift determination.

1.2.1 Theoretical work

It is well known that finding analytical solutions to equations of viscous fluid motion, associated with flow-structure interaction problems of practical importance, is often hindered by insurmountable mathematical difficulties. As a result, many past investigations involving the prediction of aerodynamic forces were simplified as much as possible to avoid the entanglement with the details of the viscous fluid motions. The assumption of potential flow (inviscid, incompressible, irrotational) has been a common simplification. Even so, theoretical work involving force prediction has been less common compared to other aspects of research.

The circulation theory of aerodynamic lift, the concept underlying a scientific breakthrough in understanding and calculation of lift, was first examined by Lanchester (1926). He suggested that flow over a lifting surface involved a circulating motion superimposed on the translation motion of the free stream. For example, a flow field over a lifting airfoil can be considered as two parts, a uniform flow and a circulatory flow. Lanchester theorized that the circulatory part of the flow could be analyzed by the conceptual vortex filaments first suggested by Helmholtz (1858), which were imagined as running along the span of the wing. Though Lanchester's work described the circulation as the cause of lift, it was essentially qualitative, and no substantive aerodynamic calculation of lift was provided.

Quantitative formula relating lift to circulation was developed by two researchers, Kutta (1902) and Joukowski (1906), working independently without any knowledge of Lanchester's work (Giacomelli, 1934). In their work, a model of the flow

over a lifting airfoil was conceived to consist of vortical motions; the bound circulation vortex was embedded along chord line. A relation for calculating the lift per unit span of an airfoil was mathematically expressed as

$$L = \rho U \Gamma .$$ (1.4)

where Γ is the bound circulation, $\Gamma = \oint \vec{V} \cdot d\vec{l}$, expressed as line integral of the flow velocity taken around any closed curve encompassing the airfoil. Equation (1.4) was a revolutionary development in theoretical aerodynamics, named as Kutta-Jukowski (K-J) theorem, a key component leading to development of the UCMT that will be discussed in detail in a subsequent section.

Use of the K-J theorem has been justified for steady, inviscid incompressible flows in the past. Because of the inviscid condition, the circulation around any closed curve enclosed the airfoil will remain constant and equal to the bound circulation within a curve that only encloses the airfoil for steady flow. In reality, however, the flow is viscous, and dissipation effects always exist. The circulation calculated within a curve far away from the model is thus zero, as is the circulation measured in a curve exactly matching the surface of the body due to the no-slip condition. Hence, an issue in applying this theorem in practice is selecting the proper closed curve that can provide the bound circulation for lift determination. Also the question of availability of this theorem under time dependent conditions is critical for unsteady flow study and is a major topic of our research. For example, Glauert (1959) and Katz and Plotkin (1991) found that an additional term to count for the unsteady effect of the circulation has to be included in the total lift force determination.

With incompressible unsteady potential flow theory; Katz and Plotkin (1991) have summarized earlier work by Theodorsen (1935) and von Karman & Sears (1938) on a two-dimensional unsteady flow around an oscillating flat plate. We will also use this flow as a representative unsteady flow in later sections. The unsteady potential theory assumes the flow is inviscid, time-dependent, and flow can be modeled with combinations of singularities (point vortex, source, doublet) as in steady potential flow theory. With the concept of velocity potential Φ and stream function Ψ, the complex potential theory can provide a good mathematical tool for analytical study. In the stress integration method, unsteady Bernoulli equation can act as the bridge to connect the circulation to lift force.

$$\frac{p_\infty - p}{\rho} = \frac{1}{2}\left|\vec{V}\right|^2 + gZ + \frac{\partial \Phi}{\partial t} \quad . \tag{1.5}$$

where p_∞ is the static pressure of the free-stream flow, p is the static pressure on the surface of the airfoil, Φ is the velocity potential, $\vec{V} = \nabla\Phi$ is the velocity field. gZ is the gravitational potential energy which can be ignored for air flow. With $\Gamma = \oint \vec{V} \cdot d\vec{l} = f_1(\Phi)$, $L = \oint p \cdot ds = f_2(\Phi)$, circulation Γ can be related with lift L. By using a time derivative transformation between body frame (x,y,z) and inertial frame (X,Y,Z) (Fig 1.3).

$$\frac{\partial}{\partial t_{inertial}} = -[\vec{V}_0 + \vec{\Omega} \times \vec{r}] \cdot \nabla + \frac{\partial}{\partial t_{body}} \quad . \tag{1.6}$$

8
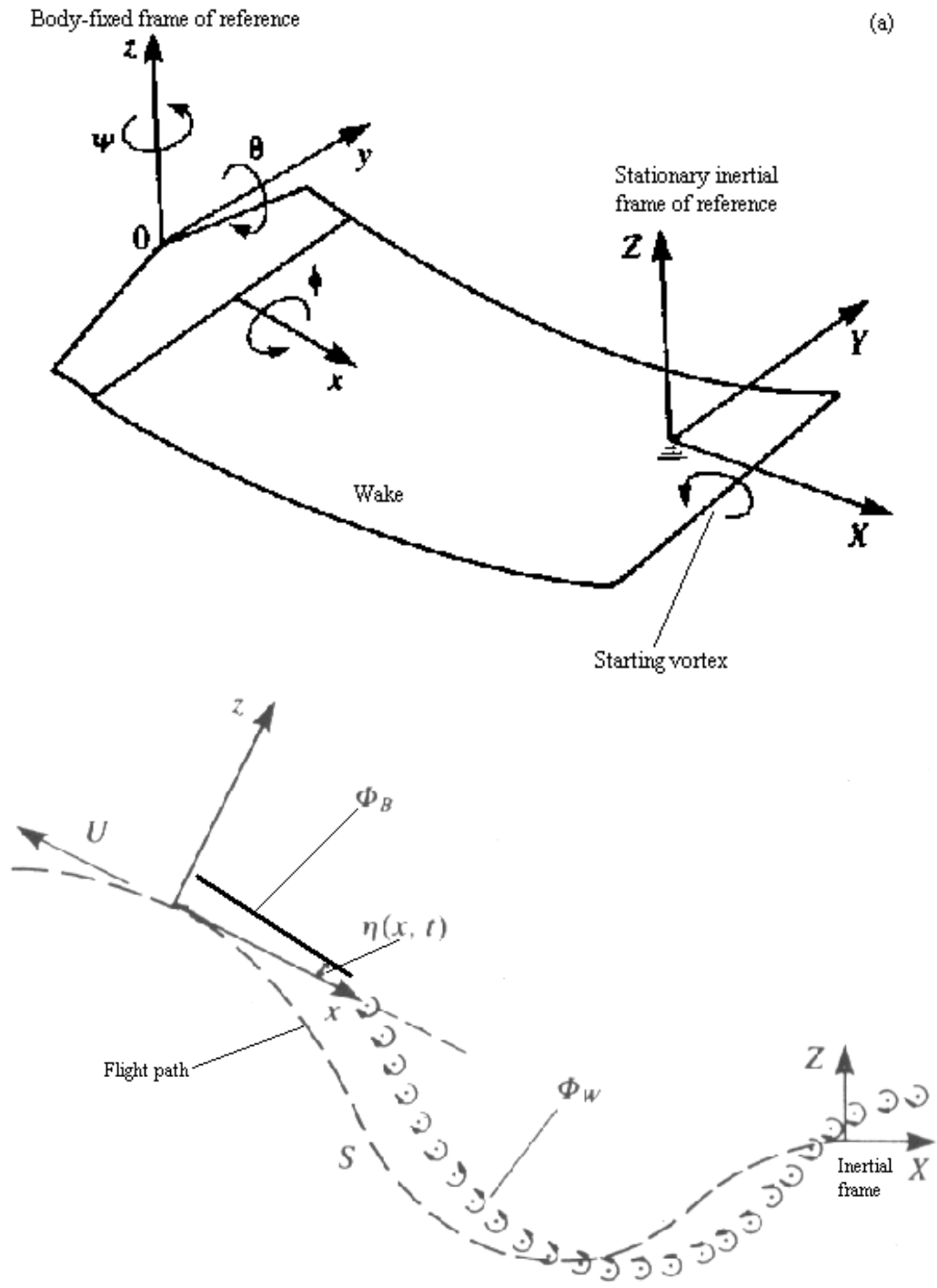
Fig. 1.3 (a) Body (*xyz*) and Initial (*XYZ*) coordinate systems (Fig13.1 of Katz &Plotkin(1991)).
(b) 2D view with nomenclature (Fig. 13.14 of Katz & Plotkin (1991))

The unsteady Bernoulli equation can also be expressed as

$$\frac{p_\infty - p}{\rho} = \frac{1}{2}(\nabla\Phi)^2 - (\vec{V}_0 + \vec{\Omega}\times\vec{r})\cdot\nabla\Phi + \frac{\partial\Phi}{\partial t} \ . \tag{1.7}$$

where $\vec{V}_0, \vec{\Omega}$ is the velocity, rate of rotation of the airfoil, $\vec{r}$ is the position vector in the body's frame of reference. The continuity equation can be expressed as

$$\nabla^2\Phi = 0 \ . \tag{1.8}$$

for an airfoil that is not rotating and only moving with velocity $\vec{V}_0 = U(t)\vec{i}$. With higher order small quantities eliminated, (1.7) can be simplified as

$$\frac{p_\infty - p}{\rho} \approx U(t)\frac{\partial\Phi}{\partial x} + \frac{\partial\Phi}{\partial t} \ . \tag{1.9}$$

hence, the pressures on the lower and upper surface of the airfoil will be

$$p_l = p_\infty - \rho\left(U(t)u(x,0-,t) + \frac{\partial\Phi(x,0-,t)}{\partial t}\right) \tag{1.10}$$

$$p_u = p_\infty - \rho\left(U(t)u(x,0+,t) + \frac{\partial\Phi(x,0+,t)}{\partial t}\right). \tag{1.11}$$

and the pressure difference across airfoil can be expressed as

$$\Delta p = p_l - p_u = \rho\left[U(t)\big(u(x,0+,t) - u(x,0-,t)\big) + \frac{\partial}{\partial t}\big(\Phi(x,0+,t) - \Phi(x,0-,t)\big)\right]. \tag{1.12}$$

According to the thin airfoil theorem, $u(x,0+,t) = \frac{\gamma(x,t)}{2}$, $u(x,0-,t) = -\frac{\gamma(x,t)}{2}$,

and $\Phi(x,0+,t) - \Phi(x,0-,t) = \int_0^x \gamma(s,t)ds = \Gamma(x,t)$. Finally, the lift expression can be obtained through the pressure integration around the body as

$$L = \int_0^c \Delta p \, dx = \underbrace{\rho U(t)\Gamma(t)}_{} + \underbrace{\rho \int_0^c \frac{\partial}{\partial t}\Gamma(x,t)dx}_{B} \; . \qquad (1.13)$$

where part A is the quasi-steady part and B is the unsteady part. $\Gamma(t)$ is the total instantaneous bound circulation around the body, and $\int_0^c \gamma(s,t)ds = \Gamma(t)$. The measurement of $\Gamma(x,t)$, the circulation distribution along the airfoil chordline, in this equation is a challenge in experimental studies. This measurement will be discussed further in future sections.

While the work of Katz & Plotkin (1991) will serve as the theoretical framework for later work in chapter 2, we also review other previous developments in the theory of lift determination that will also be applicable to our work. Wu (1981) developed a general theory for aerodynamic forces and moment, through a rigorous analysis of the viscous flow equations based on control volume concept, combined with vorticity transport and decay. When his theory is applied to steady flow over a flat plate or airfoil, a formula similar to Kutta-Joukowski theorem was obtained

$$L = \rho U (\Gamma_s + \Gamma_{a)} \; . \qquad (1.14)$$

where circulation in two distinct regions is considered. Γ_s is the total vorticity (circulation) in the area just before the trailing edge, and Γ_a is the vorticity in the wake between the trailing edge and somewhere in the wake where the fluid velocity has recovered to the free stream velocity. Concerned about the viscous dissipation and decay, this work showed that for bound circulation determination, the selection of closed curves enclosing aerodynamic bodies is crucial. Later we will use a similar

technique of considering circulation in distinct flow regions when studying instantaneous lift forces for a circular cylinder flow.

Lighthill (1986) analyzed the fundamental aspects of the wave loading acting on offshore structures; The main concept leading to an important advance in understanding of lift on bodies in an unsteady flow was developed to separate the total loading into a potential-flow force and an vortex-flow force. The potential flow force is related to the drag on structures and expressed as the well-known Morison equation, which is not a concern in this research. The vortex flow force is derived from the momentum of the vortex flow component, which can be expressed as $\frac{1}{2}\rho\int \vec{r}\times\vec{\omega}d\forall$, where $\vec{r}$ is the position of a vortex element with volume $d\forall$ and vorticity $\vec{\omega}$ in fluid flow. Similar to the Newton's second law, the time derivative of the moment equals to the force. A more accurate vector expression for vortex force is given by

$$F_v = -\frac{d}{dt}\left[\frac{1}{2}\rho\int \vec{r}\times\vec{\omega}d\forall\right] . \tag{1.15}$$

Rockwell (1996) applied Lighthill's results and equation (1.15) to the experimental study of flow around an oscillating cylinder, based on the flow field information obtained from particle image velocimetry techniques. Govardhan & Williamsom (2000) used it while investigating the vortex modes and frequency response for a freely vibrating cylinder. In later section, we will study the application of Lighthill's results to estimate the instantaneous lift force on a circular cylinder at low Reynolds number. Our interest will be in determining if information measurable using the UCMT technique can be converted to an accurate lift estimation via equation (1.15).

Recently, more advanced techniques to obtain the flow velocity field experimentally have been used, such as the Particle Image Velocimetry (PIV). While discussion of experimental lift determination techniques will be reserved in section 1.2.2, use of PIV has motivated a theoretical advance in this area. A theoretical expression for the evaluation of instantaneous forces on circular cylinder in an incompressible flow was put forward by Noca (1997). Based on a momentum principle, it can be expressed as

$$\vec{F} = -\frac{1}{N-1}\frac{d}{dt}\int_{V(t)}\vec{r}\times\vec{\omega}d\forall + \oint_{S(t)}\vec{n}\cdot\overline{\overline{\Theta}}dS - \frac{1}{N-1}\frac{d}{dt}\oint_{S_b(t)}\vec{r}\times(\vec{n}\times\vec{u})dS. \qquad (1.16)$$

where N is the dimension of the space under consideration (N=2 in a two-dimensional space), $\overline{\overline{\Theta}}$ is a tensor related to velocity, vorticity and viscous shear stress, V(t) is a volume bounded by a non-material surface S(t) moving with velocity $\vec{u}$. The first term in the right hand side of the equation is similar to the vortex force by Lighthill (1986). Application of Eq. (1.16) to cylinder wake experiments will be discussed in section 1.2.2.

Further investigations to develop refined theories for aerodynamic force prediction in unsteady flows have been undertaken in the past. Sarpkaya (1975) applied a numerical discrete vortex method to develop a lift expression for two-dimensional potential flow. The complex potential function and Joukowski transformation were used for the mathematical manipulation, and the generalized Blasius theorem (which apply the integration of derivative of the complex potential along a closed curve enclosing an aerodynamic body to calculate the normal and tangential force in a potential flow) was

used to determine the drag and lift. The lift includes two parts, quasi-steady and unsteady, it can be expressed as

$$L = -\rho \sum_{k=1}^{m} \Gamma_k (-U - u_k - u_{k_i}) - \rho \sum_{k=1}^{m} r_{k_i} \frac{\partial \Gamma_k}{\partial t}.$$ (1.17)

where, U is the free stream velocity, Γ_k and u_k are the circulation and velocity in the x-direction of the kth vortex in the wake, while u_{k_i} and r_{k_i} are the velocity and location of the corresponding image vortex. Given that this is a numerical technique, it is difficult to apply in an experiment since the vorticity and velocity of each vortex element would need to be measured. However, we will later return to this equation to interpret some of our later results.

1.2.2 Experimental work

Several methods exist to obtain fluid forces acting on an aerodynamic body in experiments. In the following sections, the force balance method, pressure integration methods, particle image velocimetry (PIV) method and the ultrasonic circulation measurement technique (UCMT) are described.

Force balance measurement systems have been commonly used in aerodynamic research for many years. The term "balance" is generally used to describe instruments designed to measure forces on aerodynamic bodies with a relative high degree of accuracy. The first rough mechanical balance for measuring fluid forces was invented by Mariotte (Giacomelli, 1934) to study the forces created by a moving fluid impacting on a flat surface. Based on his investigation, he proved that the force of impact of the

fluid on the body varied with the square of the flow velocity. This is an early breakthrough in the history of aerodynamics. Later, it was derived theoretically based on the mathematical laws advanced by Newton in his Principia (1867).

Since the invention of wind tunnel, aerodynamic research can be conducted in a controlled air stream under laboratory conditions. Correspondingly, various forces balances were developed for different force measurement requirements in various investigations. Six-component balances (three forces and three moments) are the most sophisticated set-up for aerodynamic research, but one, two or three-component balances are also used. However, a deficiency of force balances is that they are generally limited to measuring of total lift force on a structure, equivalent to integrating the local sectional forces along the span of an aerodynamic body. Force balance cannot isolate sectional lift forces that are important for determining the motion of flexible slender structures. As a result, an alternative method is required to measure the local sectional lift force. This is a goal of the present work, which will be addressed in a later section.

Force balances generally operate on the principle of amplifying the effects that small structural deflections have on the capacitance, inductance, or resistance of measuring devices, such as strain gauges, load cells, or electromagnetic balances. The advantage of these types of balance is that the data can be acquired and processed more easily and automatically with the aid of modern computers.

Pressure integration methods involve obtaining forces directly from body surface pressure distribution, or from the pressure distribution along wind tunnel walls based on a control volume theorem.

The surface pressure distribution integration method is more suitable for two-dimensional flow measurements. Beyond the force acquisition capability, pressure measurement can also provide fundamental information related to the fluid motion around the body such as the velocity variation, separation effects and shear layer or vortex development. Experimentally measurement of the pressure distribution is generally carried out by covering the body with an array of pressure sensors. In some cases, however, the geometry of the model may be too small to permit the use of a sufficient number of sensors.

The 'pressure averaging' method is another type of measurement technique based on pressure integration. In this technique, two sets of pressure taps are located around each half circumference of the cylinder. Each set of the taps is connected to a common reservoir (pressure averager), such that the average pressure over half the cylinder is obtained with insignificant distortion and phase shift. Then, by subtracting the integrated average pressure obtained on opposing sides of the cylinder, the net instantaneous transverse force is obtained (Surry & Stathopoulos, 1977; Bearman & Luo, 1988; Waker, 1990). This technique is more suitable for force measurement on two-dimensional rigid body that spans the tunnel test section. For sectional force measurement on flexible slender body, this method may not work.

The force on a model in a closed tunnel can also be determined from the reaction on the boundaries of the working section by measuring the distribution of the static pressure along the walls. The theoretical basis for this wall pressure method is the integral momentum equation.

The integral momentum equation states that the time rate of change of momentum due to unsteady fluctuations of flow properties inside a control volume plus the net flow of momentum out of the control volume across control surface is equal to the total force acting on the fluid enclosed in the control volume. When the momentum theorem is applied to a control volume enclosing an aerodynamic body in a wind tunnel, the walls will be the control surfaces and the pressure variation on these surfaces can be used to determine lift, through the integration of the wall pressure difference (Doenhoff & Abbott, 1947). The only parameter one needs to measure is the pressure distribution along wall from infinite upstream to infinite downstream theoretically, based on the location of the test model. Practically, the measured range is only several times of the model scale. The error caused by this finite measured range can be corrected by a momentum scheme coefficient. For the measurement of pressure distribution along the walls, a multi-tube manometer or a series of pressure transducers can be used for steady flows. For unsteady flow, fast response pressure transducers must be used. The wall pressure measurement method can also be explained with Newton's third law; the lift acting on the body is of the same magnitude of that acting on the walls, but with opposite direction. The fluid is only acting as a medium to transfer the lift force.

This method has been broadly applied for about seven decades. Recently, Yuan (1994) used it to validate a novel velocity integration method for the correction of wind tunnel wall interference for test models with larger blockages. The corrected force and pressure distribution on the cylinder was very good even for a 17% blockage. Linn (1999) used a similar method to measure lift on a oscillating pitching NACA 0012 airfoil by integrating the pressure distribution along the tunnel walls at different angle of attack. The goal was to investigate the effects of reduced frequency and amplitude on the final lift force. As for the force balance measuring system, this pressure integration method is also more suitable for measure the averaged lift for two-dimensional flow around a rigid body. For local sectional lift measurement, alternative methods are still required.

As described above, the traditional force measurement methods are not effective for local sectional lift measurements. Hence, one has to resort to some other methods that have the capability for sectional lift measurement under non-intrusive (natural) conditions. Recently developed techniques such as the particle image velocimetry (PIV) method and ultrasonic circulation measurement method have addressed this issue.

Particle image velocimetry (PIV) is a technique for simultaneously measuring three components of fluid flow velocity at points on a two-dimensional plane. Generally PIV includes several components. First, the fluid flow being measured is seeded with small tracer particles that can follow the fluid velocity fluctuations. Second, the flow is illuminated by a sheet of laser light at least twice. Third, the particle positions during each illumination are recorded by camera. The flow speed within the light sheet can be

calculated approximately by measuring the distance particles moved between each illumination. In identify corresponding particles between two images, more advanced techniques are needed. One of them is the autocorrelation method, in which the resulting peak represents the most likely particle distance.

Given the measured velocity field, forces on an aerodynamic body in the flow can be obtained by using various theoretical equations described in previous section. Lin & Rockwell (1996, 1997, 1999) used laser scanning and PIV techniques to investigate the relationship between the vortex formation and fluid loading for a two-dimensional streamwise oscillating rigid cylinder in steady current. Lighthill's equation (1.15), Noca's equation (1.16) and Sarpkaya's equation (1.17) were used respectively to calculate the transverse forces, which were obtained from the integration of the velocity or vorticity in a control volume enclosing the body (stationary or oscillating). The results were compared with forces obtained from other methods such as pressure average technique, Kutta-Joukowski theorem and Blasius formula. The amplitude and phase shift were studied and the instantaneous vortex structures were related to the instantaneous force at various times. However, the influence of the size and shape of the PIV control volume used for integration was not studied.

While the PIV technique provide instantaneous velocity field information which can illuminate important physical process in a flow, its use in lift determination is less well developed. Noca (1997) conducted an experiment in a water tunnel with a two-dimensional rigid circular cylinder as the model. The PIV technique was applied for measuring velocity field around the cylinder, and force balance was used to obtain the
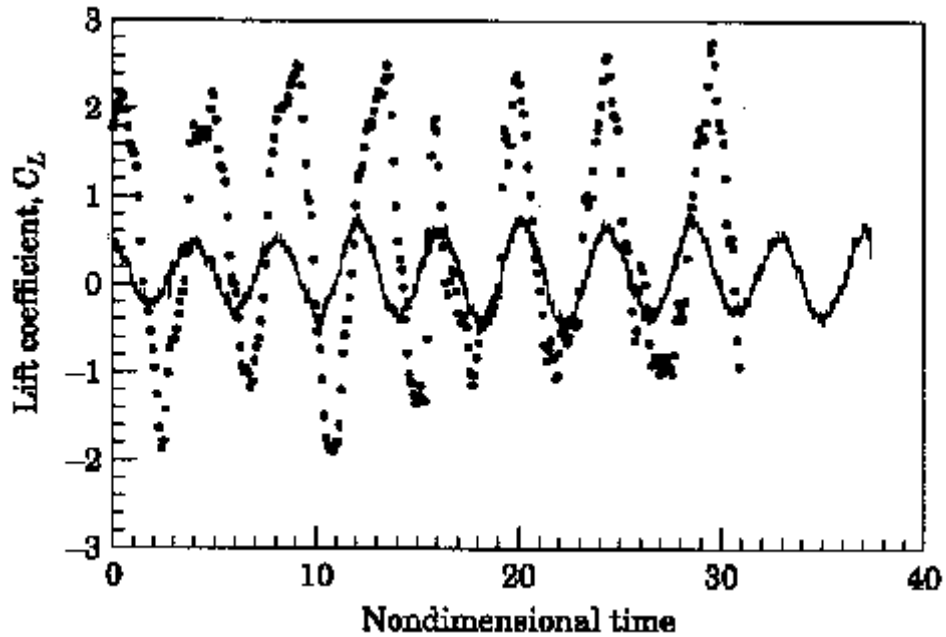
Fig. 1.4 Lift force comparison. ····· DPIV data; —— Force balance data (Fig.2 of Noca et al (1997))

spanwise-average lift force to validate equation (1.16). The force was converted from the velocity field measured in a square domain enclosing the cylinder and translating with it. The results show that 500% error exists in lift values between PIV and force balance results (Fig 1.4). Another disadvantage of the PIV is the cost of instruments and the complex alignment and operation of the system.

In recent years, a novel method, ultrasonic circulation measurement technique (UCMT) has been developed that may prove useful in resolving some issues of lift measurement in unsteady flows. In this section, we will first introduce the basic principle of this technique, and then review some past investigations that used UCMT.

The possibility of expanding the capabilities of UCMT for the unsteady and spatial varying flows is then examined.

It is well known that lift can be related to circulation within an enclosing curve of an aerodynamic body through the Kutta-Jukowski theorem under appropriate conditions. This opens a way to experimentally obtain lift data through acquiring circulation data. Instead of obtaining circulation through the velocity measurement along a closed path and mathematical integration, the possibility of measuring circulation directly and non-intrusively using ultrasound was introduced by Schmidt (1970,1975). In the past thirty years, ultrasound circulation measurement technique (UCMT) has been improved significantly and verified as an effective way to measure flow circulation. A detailed review can be found in Johari & Durgin (1998). A simple introduction to this technique is described below.

UCMT is based on the measurement of the time difference for two sound waves traveling oppositely along a closed path that encloses a body immersed in moving fluid
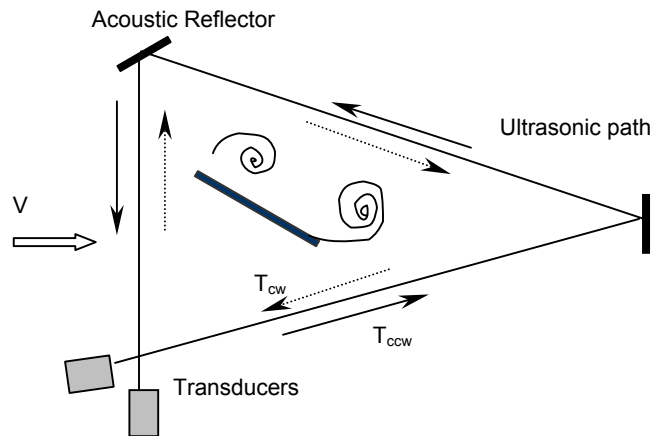
Fig.1.5 Schematic of a closed sound path for UCMT

as shown in Fig. 1.5. Two ultrasonic transducers and two acoustic reflectors (mirrors) are generally employed to establish the closed path that encloses the bluff body. Each transducer acts as both emitter and receiver. The sound pulse emitted by the first transducer is redirected by the reflectors and received by the second transducer. The propagation speed of the sound wave is the sum of the local sound speed and the local fluid velocity. Hence, if the sound pulse travels in the same (opposite) direction as the local fluid speed, the sound transit time will be decreased (increased). This process is repeated by emitting a pulse in the opposite direction along the closed path. The transit times of the pulse in the two directions around the closed path are

$$T_{cw=}\oint\frac{dl}{a+V} \quad ; \quad T_{ccw}=\oint\frac{dl}{a-V} . \tag{1.18}$$

$$\Delta T = T_{cw} - T_{ccw} = \frac{2}{a^2}\oint\frac{Vdl}{1-\left(V^2/a^2\right)} = \frac{2\Gamma}{a^2} . \tag{1.19}$$

$$\Sigma T = T_{cw} + T_{ccw} = \frac{2}{a}\oint\frac{dl}{1-\left(V^2/a^2\right)} = \frac{2}{a}P . \tag{1.20}$$

From Eq. (1.19) and (1.20), the local sectional circulation can be given as

$$\Gamma = \oint\vec{V}\cdot d\vec{l} = 0.5 \ a^2 \Delta T = 0.5(\frac{2l_p}{\Sigma T})^2 \Delta T = 2[\frac{l_p}{\Sigma T}]^2 \Delta T . \tag{1.21}$$

where l_p is the total length of the sound path, a is the sound speed, V is the local fluid velocity. In the derivation of eq (1.19), (1.20), the assumption $V/a \ll 1$ is applied, limiting the technique to low speed incompressible flow. A major advantage beyond the non-intrusive nature of UCMT is its low cost. A typical UCMT system costs one to

two orders of magnitude less than a PIV system. While the PIV technique does yield more detailed local flow information (velocity, vorticity fields); In this thesis, we will attempt to show how global correlation measurements can also be very useful for lift determination in unsteady and three-dimensional flows.

In the past, UCMT has been used for experimental studies of various flows including free surface vortices in aqueous flows, delta wing circulation determination, wing tip vortex effects and lift study of airfoils with/without oscillation. Smith *et al* (1995) conducted experiments to study the swirl strength of free surface vortical flow. A Rankine vortex model was used to validate the circulations measured from the UCMT technique. Moreira & Johari (1997) studied the leading edge vortex effects on a delta wing. Circulation behavior was examined as it related to primary vortex burst location. Linear and nonlinear regimes were found at different range of angle of attacks (AOA). Test results highlighted the need for more rigorous models of circulation incorporating primary vortex behavior. Desabrais & Johari (1998) further studied wing tip vortex behavior on a sharp-edged NACA 0012 wing. The effects of the size of closed ultrasound path was examined, they found that the circulation distribution achieved its maximum level when the sound path surrounds the whole vortex. The comparison of the lift measured from a load cell and the lift from UCMT showed a better agreement in streamlined flow with angle of attack of less 10 degree. Beyond that AOA, fair agreement was observed. For the airfoil lift study, Purutyan (1990) used UCMT with a simplified single leg path to study the behavior of a plunging airfoil, the motion of the airfoil was always leading the lift by a phase angle. Weber (1995) used

the similar single leg path to investigate the stall behavior of a NACA 4418 airfoil undergoing pitching oscillation. At lower oscillation frequency, hysteresis loops was observed. Maximum lift increased linearly with the reduced frequency. Comparison of these results with other investigators yielded some disagreements in lift measurements.

While past research did provide interesting results using UCMT technique, a primary concern is the conversion of the measured circulation to the lift force. The Kutta-Joukowski theorem is applicable to steady flow. However, it was also applied using a quasi-steady assumption, $L = \rho U \Gamma(t)$, in the work of Purutyan (1990), Weber (1995). Here $\Gamma(t)$ represents the measured unsteady circulation with an acoustic path enclosing the body. UCMT has not been applied to measure lift distributions along structure spans in three-dimensional flows or unsteady flows. Hence, extending this technique for unsteady and spatial varying fluid flows, while addressing the issues introduced above, is the major intent of this research.

1.3 Major goals

Our introductory sections have highlighted the need for accurate lift determination on aerodynamic bodies in unsteady flows. In particular, the fundamental importance of the lift force in understanding nonlinear coupling between structural motions and flow dynamics in fluid-structure interaction problems has been addressed. At the same time, deficiencies exist in current experimental techniques available to measure lift forces. These deficiencies are most acute in the areas of instantaneous lift measurement, and measurement of local, sectional lift forces along structural spans.

However, these two effects, unsteadiness and spatial variation, are also key characteristics of lift forces in fluid-structure interaction problems.

An experimental method with the potential to address these deficiencies, the ultrasonic circulation measurement technique (UCMT), has been developed in recent years. This method has been applied primarily to measure *mean* (time-averaged) lift in experiments on various flows. However, the extension of the UCMT methods to measure time-varying lift forces in unsteady flows has remained largely unstudied. The UCMT methods have also not been applied to measure local, sectional lift forces along structural spans. The major goals of this thesis are to address these concerns by;

- studying the extension of the UCMT methods to determine instantaneous lift values in unsteady aerodynamic flows using a combined analytical-numerical approach.

- applying UCMT methods to measure mean lift distributions along the spans of structural elements in experiments on low speed, incompressible flows.

- study the issue of dependence of UCMT lift measurements on the specific acoustic path used to determine bound circulation values.

To accomplish these goals, an integrated analytical-numerical-experimental approach outlined in the following paragraphs is used. Table 1.1 summarizes the research matrix. In Chapter 2, an analytical study of the flow over an oscillating thin airfoil (flat plate) is described. This flow serves as a representative unsteady flow. We address the issue of the proper method needed to convert instantaneous circulation measurements (of the type attainable from a UCMT experiment) to instantaneous lift values. The work of Theodorsen (1935), Karman & Sears (1938), Katz & Plotkin

(1991), based on unsteady potential flow theory, is extended to develop this proper conversion method, which we name the unsteady correction method. The unsteady correction method incorporates an additional unsteady term in addition to the quasi-steady Kutta-Jukowski term that has been utilized in past investigations using UCMT. The accuracy of the unsteady correction method compared to the quasi-steady Kutta-Jukowski approach is studied. RMS lift amplitudes and phase angles determined resulting time traces of instantaneous lift force are compared. After establishing this basic framework, we analytically study additional unsteady flows, including pitching flat plates, plunging flat plates, and impulsively started flat plates, in a similar manner.

In Chapter 3 we use numerical simulations to verify that the developed unsteady correction method can properly predict instantaneous lift values in viscous, unsteady flows. While our eventual goal is application of the unsteady correction method to circulation data from experiments, we choose to first perform this verification using numerical techniques. Numerical techniques offer certain advantages including the capability to obtain independent lift values through integration of surface stress distributions. Also, in the numerical simulations we can easily mimic the acoustic path that would be utilized in an experimental UCMT set-up. Study of the effect of variation of the acoustic path on lift measurements is conducted. The dependence of lift measurements on the prescribed acoustic path has not been systematically studied prior to the present work.

The finite element simulation of viscous flow over an oscillating flat plate is conducted at Reynolds numbers (based on plate chord-length) on the order of 100. The

study is conducted at low Reynolds numbers to avoid complexities arising from turbulent, three-dimensional flows, such as the need for phase-averaging of lift measurements. Also, since our correction methods are based on inviscid theory, we believe that a highly viscous flow at low Reynolds number represents a 'worst-case' scenario, and that the developed the correction method would yield even better results for higher Reynolds number flows. Also, many open questions regarding vortex formation and flow-induced vibration still exist even at these low Reynolds numbers. The velocity flow fields from the simulation are analyzed to determine the instantaneous circulation by integrating local velocity vectors along the enclosing acoustic path. This bound circulation is then converted to instantaneous lift using the developed unsteady correction methods and the quasi-steady Kutta-Joukowski approximation. These lift values are compared to instantaneous lift values (true lift) determined from integration of the unsteady surface stress distribution.

Given the success of this validation using the numerical techniques, we next study the application of the unsteady correction method of Chapter 2 to correct instantaneous circulation data from a previous experimental UCMT study on rotational oscillations of a thin airfoil (Weber 1995).
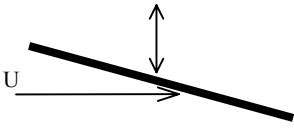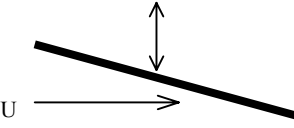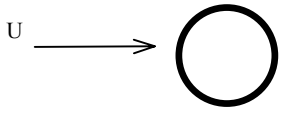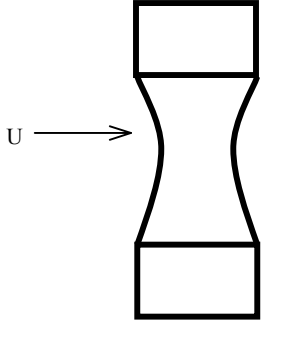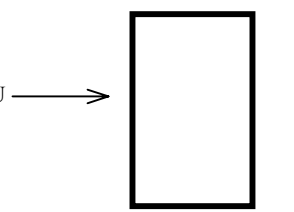
Having achieved a better understanding of lift determination in unsteady thin airfoil flows, in Chapter 4 we study another important flow, low Reynolds number vortex shedding from a stationary bluff body (circular cylinder), using similar techniques. We study whether instantaneous circulation values (of the type attainable from UCMT experiments) can be properly converted to instantaneous lift values in this

flow. Motivated by earlier work of Wu (1981), we study various force models including a quasi-steady Kutta-Jukowski method, a vortex flow force model (Lighthill, 1986), and a new unsteady correction model similar to that developed for the thin airfoil flow of Chapters 2 and 3. Finite element simulations for flow over a circular cylinder at Re = 100 are once again performed in order to obtain true instantaneous lift values (from surface stress integration), which are then compared to various combinations of the force models. We study whether UCMT measurements can provide the necessary data in experiments to properly apply the vortex flow force model.

In the previous chapters, we used theory and simulations to study the issue of converting circulation to instantaneous lift force for unsteady flows. In chapter 5, we turn our focus to experimental UCMT studies of lift variation in three-dimensional flows.

Again, a flat plate airfoil is studied since three distinct regimes exist depending on the angle of attack (AOA). At small AOA, streamlined flow exists, at intermediate AOA, stalled flow, and at larger AOA, bluff body flow. To verify our UCMT methods, various flat plates with constant chord length or imposed chordlength non-uniformity are studied. The *mean* lift distributions along the plate span are measured with UCMT. The near wake vortex structure is also visualized with smoke visualization techniques. Once the experimental methods are verified, we study low Reynolds, low aspect ratio (AR) finite wings related to Micro Aerial Vehicle (MAV) applications. MAVs are small flying wing aircraft (with maximum dimensions less than 12") that operate at low Reynolds number. Rectangular wings with Re < 42,000 and AR < 3 are studied and

Table 1.1   Research matrix giving details of proposed work

Goal	Flow cases	Parameters	Description
Develop correction method to properly convert instantaneous circulation to lift.	U →	Low angle of attack α, Low amplitude h_a/c, Low reduced frequency k	*Analytical work.* (chapter 2)
Verify the above methods applied to both streamlined and bluff body flows. Investigate the effect of the size and location of the integral path used to determine the bound circulation.	U → U → ○	Low angle of attack α, Low amplitude h_a/c, Low reduced frequency k	*Numerical work.* Use a finite element code to obtain pressure, integrated lift and velocity field. Develop logic to determine circulation within integral path and convert to instantaneous lift. (chapter3 & 4)
Measure mean circulation distribution along span of spatially varying flows (3D flows)	U →	3D flat plates flows, sinusoidal chord variation for UCMT verification studies.	*Experimental work.* UCMT techniques in wind tunnel for mean lift measurement. (chapter 5)
	U →	Low aspect ratio b/c, low $Re \cong 10000$, flat plate flows with applications to micro-aerial vehicles	

compared with Plandtl's lifting line theory. Finally, the integrated lift force on low Re low AR wings will be compared with results from force balance measurements and previous investigations.

The conclusions will be presented in chapter 6.

Chapter 2

A Method for Converting Circulation to Lift
Based on Unsteady Potential Flow Theory

2.1 Introduction

In this chapter, we develop analytical methods to properly convert instantaneous circulation measurements (of the type that can be obtained from UCMT experiments) to determine the instantaneous forces (lift) on a structure oscillating in a two-dimensional fluid flow. This section will focus on issues related to unsteady aerodynamics by analyzing various motions of a streamlined aerodynamic body. Following Theodorsen (1935), von Karman & Sears (1938) and Katz & Plotkin (1991), we primarily study an oscillating thin airfoil (flat plate) as a representative flow, concentrate on extending the UCMT techniques to measure lift in unsteady flows, and leave any discussions of spatial variation effects to later chapters.

The connection between lift and fluid circulation within an area enclosing an aerodynamic body is given by the Kutta-Joukowski (K-J) theorem for steady flows. An experimental method based on the K-J theorem, the ultrasonic circulation measurement technique (UCMT), first proposed by Schmidt (1975) to measure the circulation around airfoil, has unique advantages. Details of UCMT method have been described in chapter 1. While most of the research based on this method has focused on measuring *mean* (time-averaged) circulation and lift, less emphasis has been placed on developing methods to measure instantaneous circulation and lift required for unsteady fluid flows. Several studies have been attempted in this direction. Purutyan (1990) applied UCMT method on a plunging NACA-0012 airfoil at Reynolds number of 5.8×10^5, and Weber

(1995) investigated the dynamic stall characteristic of an NACA-4418 airfoil undergoing rotational pitching oscillation with Reynolds number in range of $6.7 \times 105 \sim 6.7 \times 10^{5}$. However, these investigations made several simplifications to the basic UCMT set-up described in chapter 1. First, they used a single acoustic path to enclose the airfoil (Fig 2.1a). This is not a proper assumption for steady or unsteady flows such as pitching and plunging airfoil where a continuously generated vortex wake forms behind the airfoil. An closed ultrasound path (Fig 2.1b) used recently is the proper choice (Johari & Durgin,
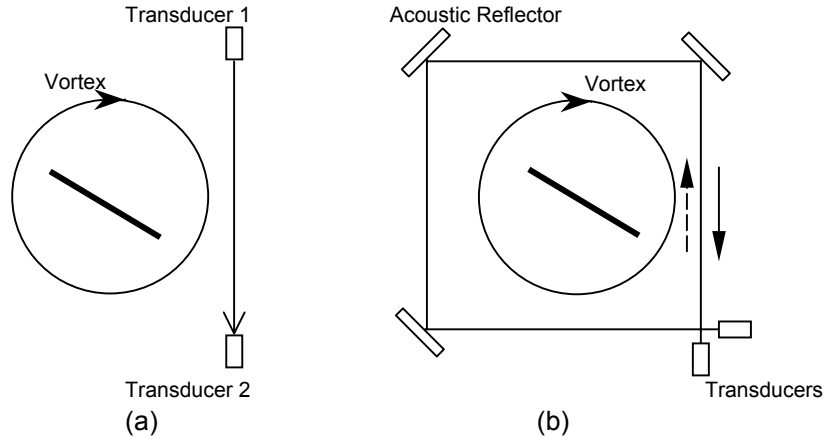
Fig 2.1 Schematic of a straight path (a) and closed path (b) for UCMT method

1998; Desabrais & Johari, 1998). Also, the conversion from time-dependent circulation into lift was carried out by using a quasi-steady K-J approximation

$$L = \rho U(t) \Gamma(t) \quad .$$ (2.1)

where $U(t)$ and $\Gamma(t)$ are the instantaneous free-stream velocity and circulation respectively. Here, $U(t) = U_{o} =$ constant. In a quasi- steady assumption, one assumes that variations of circulation occur slowly enough so that the K-J theorem (valid for steady
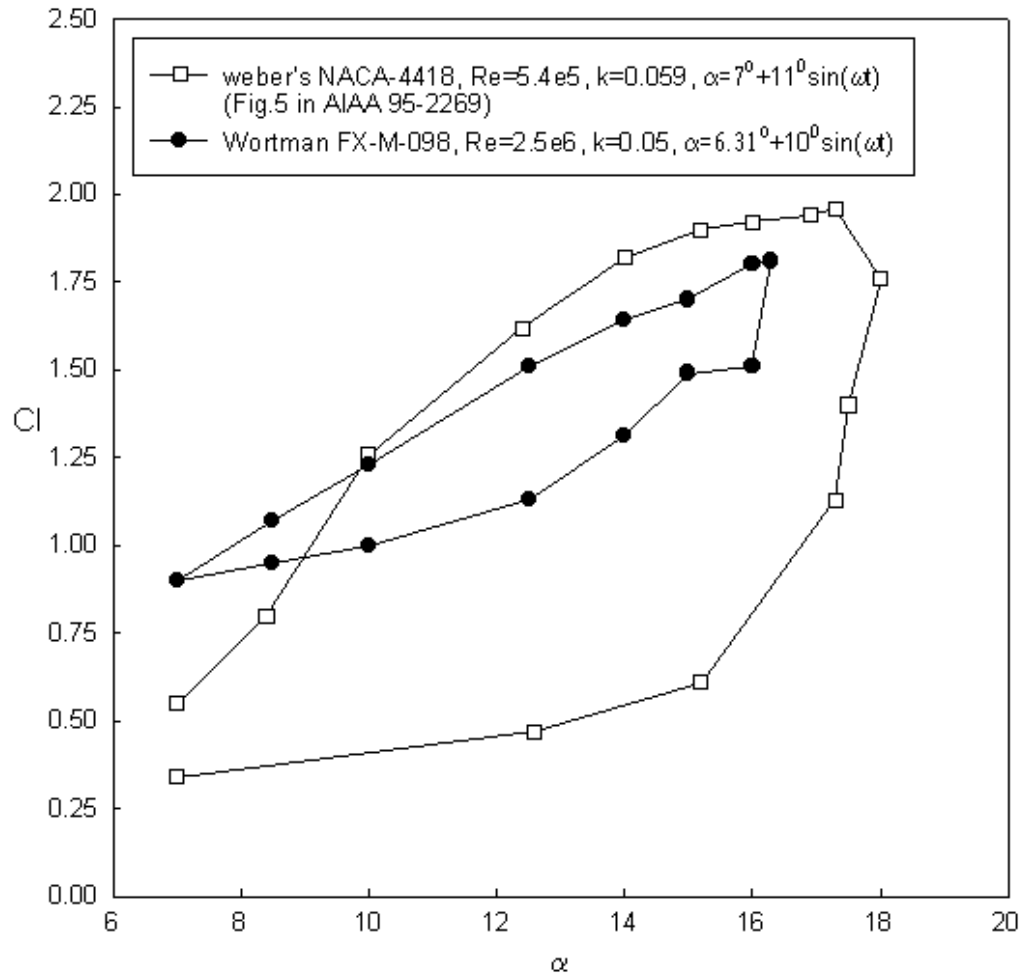
Fig. 2.2 Unsteady lift values during pitching motion of thin airfoil measured with UCMT, from Weber (1995)

flows) can be applied at each instant of time. Additional unsteady effects are ignored. A typical result from Weber's work is shown in Fig. 2.2. The deviation of Weber's lift results from other investigations suggests that equation (2.1) is not valid for unsteady flows. One goal of this chapter is to determine how much error is introduced when a quasi-steady K-J theorem is applied for unsteady flow.

In this work, we further develop the ultrasonic circulation measurement technique to improve lift measurement techniques in two-dimensional unsteady flows. Our analysis will use unsteady potential flow theory to develop a method to properly convert the instantaneous bound circulation into lift based on the work of Katz and Plotkin (1991), hence open a new way to experimentally study unsteady flows.

In next section, we will first study the relationship between the instantaneous circulation and lift based on unsteady potential flow theory. We then apply the results to a representative two-dimensional unsteady flow, a flat plate airfoil undergoing low frequency oscillation, plunging, or pitching motions, with small-amplitude in the x-z plane (Fig 2.3). The instantaneous angle of attack $\alpha(t)$ and the vertical displacement $h(t)$ of the pivot axis located at x=a, are expressed as

$$\alpha = \alpha_0 + \alpha_a \sin(\omega t), h = h_0 + h_a \sin(\omega t). \tag{2.2}$$

The subscript "0" denotes the initial value and the subscript "a" denotes the oscillation amplitude. ω denotes angular frequency of the oscillating plate.
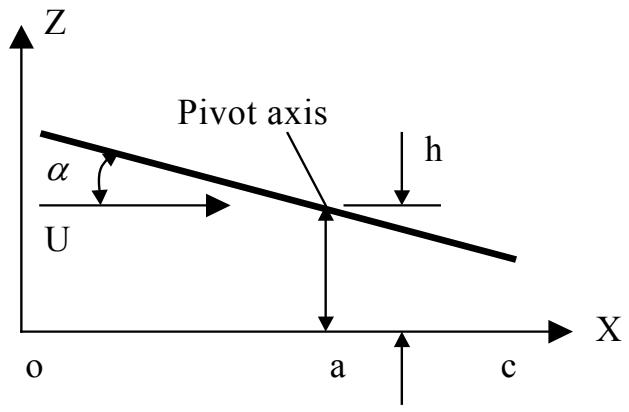
Fig 2.3 Nomenclature for the oscillating motion of the flat plate
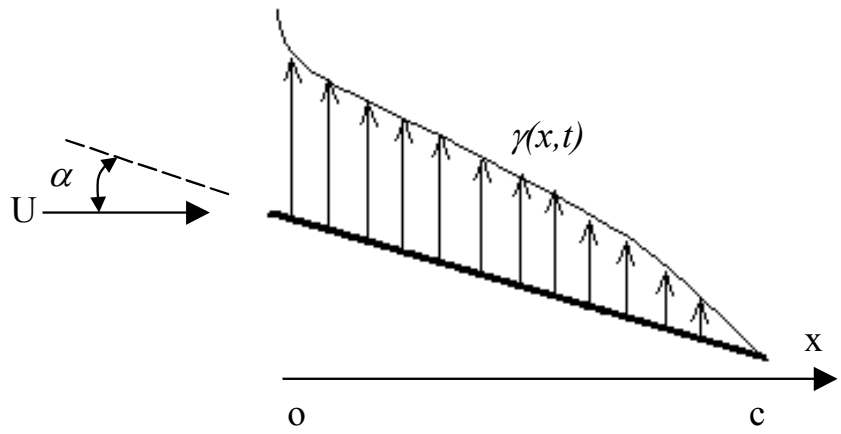
Fig 2.4 The plate chordwise circulation distribution required for determination of $\Gamma(x,t)$

2.2 Unsteady Lift

Theodorsen (1935) and Von Karman & Sears (1938) have studied the unsteady fluid forces on thin airfoils based on two-dimensional unsteady potential flow theory. Recently Katz & Plotkin (1991) have also summarized this work. In this section, we briefly review their work (part of their work has been introduced in chapter 1).

The lift force on a plate airfoil is given by

$$L = \int_0^c \Delta p \, dx = \underbrace{\rho U \Gamma(t)}_{A} + \underbrace{\rho \int_0^c \frac{\partial}{\partial t} \Gamma(x,t) dx}_{B} \quad . \tag{2.3}$$

As introduced in chapter 1, the first term A is due to the instantaneous bound circulation used when a quasi-steady K-J theorem is applied, and the unsteady term B includes the contribution from time derivative of $\Gamma(x,t)$, which can be expressed as

$$\Gamma(x,t) = \int_0^x \gamma(s,t) ds \quad . \tag{2.4}$$

Here, $\gamma(x,t)$ is the chordwise circulation distribution (Fig2.4).

Based on the classic approach of Glauert, $\gamma(x,t)$ can be approximated by a chordwise trigonometric expansion at any time instant as

$$\gamma(\theta,t) = 2U[E_o(t)\frac{1+\cos\theta}{\sin\theta} + \sum_{n=1}^{\infty} E_n(t)\sin(n\theta)] . \tag{2.5}$$

Using the standard transformation

$$x = \frac{c}{2}(1-\cos\theta) . \tag{2.6}$$

The parameters $E_o(t)$, $E_n(t)$ are coefficients of a Fourier series,

$$E_o(t) = -\frac{1}{\pi}\int_0^\pi \frac{W(x,t)}{U}d\theta \qquad\qquad n = 0$$

$$E_n(t) = \frac{2}{\pi}\int_0^\pi \frac{W(x,t)}{U}\cos(n\theta)d\theta \qquad n = 1,2,3...$$

$$\text{(2.7)}$$

where $W(x,t)$ is the local downwash, which is related to the motion of flat plate and the velocity potential. Applying a time-dependent boundary condition (no normal flow across the surface of flat plate) and after some mathematical manipulation, it can be expressed as

$$W(x,t) = \frac{\partial \Phi_B}{\partial z} = (\frac{\partial \Phi_B}{\partial x} + \frac{\partial \Phi_W}{\partial x} + U)\frac{\partial \eta}{\partial x} - \frac{\partial \Phi_W}{\partial z} + \frac{\partial \eta}{\partial t}$$

$$\approx U\frac{\partial \eta}{\partial x} - \frac{\partial \Phi_W}{\partial z} + \frac{\partial \eta}{\partial t}$$

$$\text{(2.8)}$$

where the higher order small quantities are neglected. Φ_B, Φ_W, η are the plate potential, wake potential and plate shape function respectively (see Fig. 1.3(b)).

Substituting Eq.(2.4) - (2.7) in Eq.(2.3) and after some mathematic manipulation, yields

$$L = A + B$$

$$A = \pi\rho cU^2(E_o + \frac{E_1}{2})$$

$$B = \frac{\pi\rho c^2}{4}[3\frac{\partial}{\partial t}(UE_o) + \frac{\partial}{\partial t}(UE_1) + \frac{1}{2}\frac{\partial}{\partial t}(UE_2)]$$

$$\text{(2.9)}$$

For the unsteady plate flow in Fig. 2.3, the chord line shape function can be expressed as

$$\eta(t) = h(t) - \alpha(t)(x - a) \quad.$$

$$\text{(2.10)}$$

where $h(t)$, $\alpha(t)$ and a have been defined in section 2.1. This formulation allows for study of various plate motions including oscillating, plunging, pitching through the $h(t)$ and

$\alpha(t)$ terms. Substitute Eq. (2.10) into (2.8) and (2.9), after some mathematic manipulation, Katz & Plotkin (1991) find

$$
\left.
\begin{aligned}
L &= A + B \\
A &= \pi \rho c U C(k)[U\alpha - \dot{h} + (\frac{3}{4} - \frac{a}{c})c\dot{\alpha}] \\
B &= \pi \rho c^2 [\frac{3}{4}(U\dot{\alpha} - \ddot{h}) + (\frac{1}{2} - \frac{a}{c})c\ddot{\alpha}]
\end{aligned}
\right\}.
\tag{2.11}
$$

Here $k = \dfrac{\omega c}{2U}$ is the reduced frequency, $C(k)$ is called the lift deficiency factor which is related to wake potential Φ_W, The lift deficiency factor was originally introduced in studies of airfoil flutter mechanisms, and later approximated by using an asymptotic method (Theodorsen, 1935; Von Karman & Sears, 1938). It can be expressed as

$$
C(k) = \begin{cases}
\sqrt{\left(1 - \dfrac{0.165}{(1+\frac{0.0455}{k})^2} - \dfrac{0.335}{(1+\frac{0.3}{k})^2}\right)^2 + \left(\dfrac{\frac{0.0075}{k}}{(1+\frac{0.0455}{k})^2} + \dfrac{\frac{0.1005}{k}}{(1+\frac{0.3}{k})^2}\right)^2} & ; k \le 0.5 \\[4ex]
\sqrt{\left(1 - \dfrac{0.165}{(1+\frac{0.041}{k})^2} - \dfrac{0.335}{(1+\frac{0.32}{k})^2}\right)^2 + \left(\dfrac{\frac{0.0068}{k}}{(1+\frac{0.041}{k})^2} + \dfrac{\frac{0.1072}{k}}{(1+\frac{0.32}{k})^2}\right)^2} & ; k \ge 0.5
\end{cases}
\tag{2.12}
$$

A detailed derivation of C(k)an be seen in appendix B.

Katz & Plotkin then summarized results for a flat plate oscillating vertically with a constant angle of attack, plate motion equation (2.2) will become as

$$
\alpha = \text{cons}\tan t; \qquad h = h_0 + h_a \sin(\omega t) \qquad .
\tag{2.13}
$$

Here h_0 is the equilibrium location of the plate before the oscillating, and h_a is the oscillation amplitude. Substitution of Eq. (2.13) into Eq.(2.11), yields

$$A = \pi \rho c U C(k)[U\alpha - \frac{2Uh_a k}{c}\cos(\frac{2Uk}{c}t)] \quad . \tag{2.14}$$

$$B = \pi \rho c^2 [\frac{3}{4}(\frac{2Uk}{c})^2 h_a \sin(\frac{2Uk}{c}t)] \quad . \tag{2.15}$$

$$L(t) = \underbrace{\pi \rho c U C(k)[U\alpha - \frac{2Uh_a k}{c}\cos(\frac{2Uk}{c}t)]}_{A} + \underbrace{\pi \rho c^2 [\frac{3}{4}(\frac{2Uk}{c})^2 h_a \sin(\frac{2Uk}{c}t)]}_{B}. \tag{2.16}$$

Typical time traces of the various lift component L, A and B obtained from Eq. (2.14)-(2.16) are presented in Fig.2.5. The plate angle of attack is $\alpha_0 = 2^0$, the non-dimensional vibrating amplitude $h_a/c = 0.08$, and the reduced frequency is $k = 0.35$. From the plot, we find that phase differences exist between *L, A* and *B*, with the phase of A leading L, and the phase of B always lagging L. It clearly shows that the unsteady lift term B is a significant portion of the total lift L for typical $\alpha_0, h_a/c, k$ values. As a result, the unsteady lift term must be carefully studied.

2.2.1 Limitation of UCMT for *Γ(x,t)* determination

In Eq.(2.3), the unsteady term B includes the time derivative of the circulation distribution $\Gamma(x,t)$. When $x=c$

$$\Gamma(c,t) = \Gamma(t) = \int_0^c \gamma(s,t)ds . \tag{2.17}$$

which is the total bound circulation within a region enclosed by the acoustic path in a UCMT experiment (Fig. 2.6).
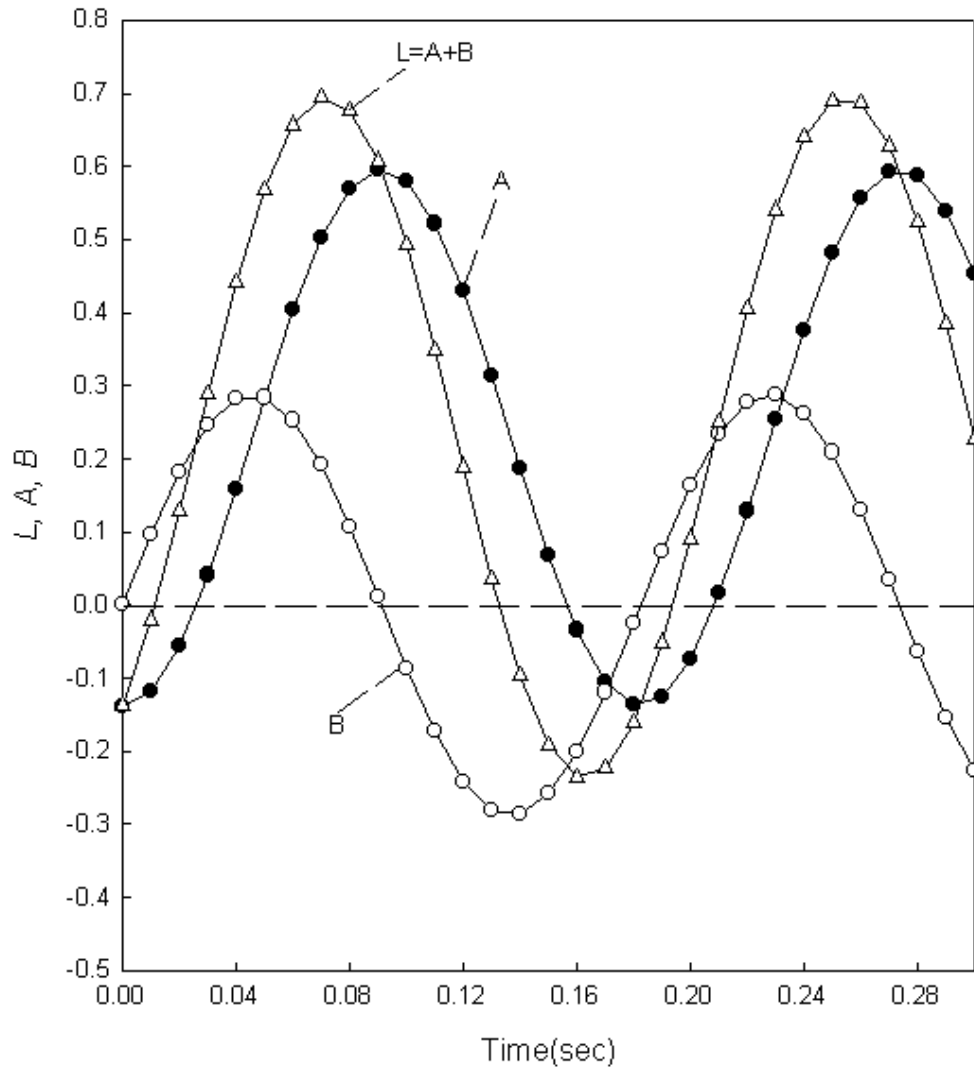
Fig 2.5 A typical lift variation with time using Katz & Plotkin's (1991) analysis of an oscillating thin airfoil (U=5m/s, c=4", k=0.35, h_a /c=0.05, $\alpha=2^0$)

Due to the limitations in applying the ultrasonic measurement technique (UCMT), the measurement of chordwise circulation distribution $\gamma(x,t)$ and circulation $\Gamma(x,t)$ is a difficult challenge in UCMT experiments. In an experiment, it would require openings along the chord line to construct an ultrasound closed path to measure the circulation distributions $\gamma(x,t)$ and $\Gamma(x,t)$ (Fig. 2.6a). As a result, one could only measure the local circulation distributions at limited chordwise locations. The measured circulation distributions may be inaccurate because the existence of physical openings would affect the flow pattern and fluid forces on the plate. The experiment would be very challenging if the plate were oscillating. However, the instantaneous bound circulation $\Gamma(t)$ around the plate is measurable with UCMT technique (Fig 2.6b). This motivates us to study if the bound circulation $\Gamma(t)$ can be used to accurately approximate the instantaneous lift on the plate.

(a) $\Gamma(x,t) = \int_0^x \gamma(s,t)ds$ (b) $\Gamma(t) = \int_0^c \gamma(s,t)ds$
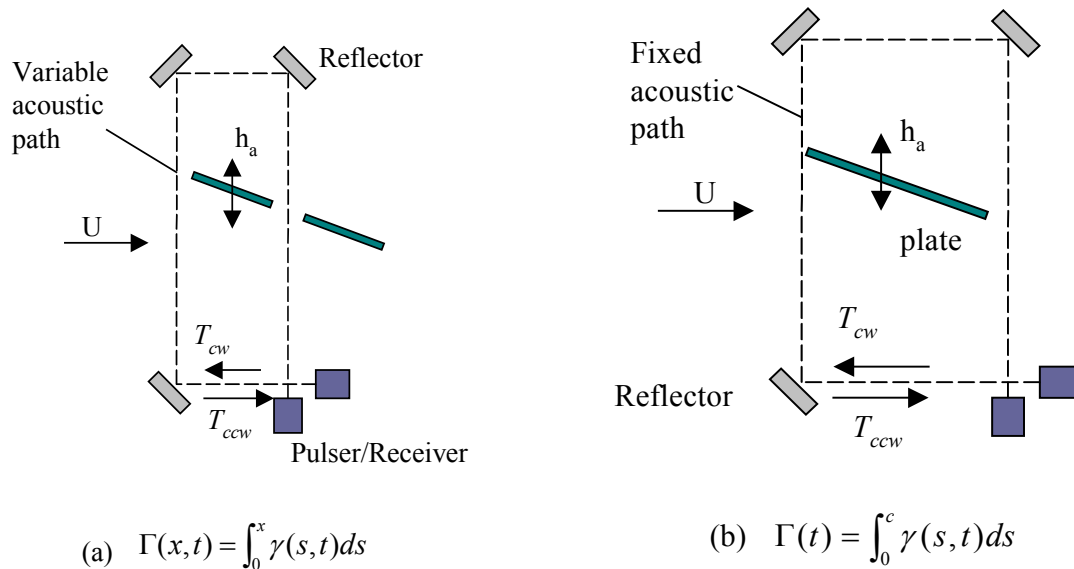
Fig 2.6 (a) Required set-up to measure $\Gamma(x,t)$ using UCMT. (b) $\Gamma(t)$ measurement using UCMT

It essence we will make an approximation which studies whether accurate lift predictions can be made even if the detailed information from the chordwise circulation distribution (e. g. $\gamma(x,t)$ and $\Gamma(x,t)$) required in equation (2.3) is unavailable. This detailed information is replaced in favor of the attainable total bound circulation $\Gamma(t)$. This assumption is reflective of difference between the UCMT and PIV techniques. The PIV, which provides local flow fields, could be used to measure $\Gamma(x,t)$. However, UCMT generally provides global information such as $\Gamma(t)$.

2.3 Approximations

In the previous section, we discussed the inappropriate utilization of K-J theory in unsteady flows, and the difficulty in applying UCMT methods to experimentally measure $\Gamma(x,t)$, a crucial component of the unsteady part of lift B. We next investigate these issues by developing approximations that will be applied to the oscillating plate flow of Fig 2.3.

Approximation 1: In this approximation, the quasi-steady part A of Eq. (2.3) is assumed to describe the lift on the oscillating plate through

$$L^{(1)} = A = \rho U \Gamma(t) = \pi \rho c U^2 (E_o + \frac{E_1}{2}).$$ (2.18)

Inserting Eq. (2.10) into (2.18), yields

$$L^{(1)} = \pi \rho c U C(k)[U\alpha - \dot{h} + (\frac{3}{4} - \frac{a}{c})c\dot{\alpha}] \quad .$$ (2.19)

Substituting Eq. (2.13) into (2.19), yields

$$L^{(1)} = \pi \rho c U C(k)[U\alpha - \frac{2Uh_a k}{c}\cos(\frac{2Uk}{c}t)] \; . \tag{2.20}$$

Approximation 2: From Eq.(2.17) and Fig 2.6b, we know that bound circulation $\Gamma(t) = \Gamma(c,t)$ can be measured using the UCMT technique. In approximation 2, we replaced $\Gamma(x,t)$ by $\Gamma(c,t) = \Gamma(t)$ in the unsteady B term of Eq. (2.3). Now $\frac{\partial}{\partial t}\Gamma(t)$ is only a function of time, so the unsteady B term in Eq.(2.3) will be

$$B^{(2)} = \rho\int_0^c \frac{\partial}{\partial t}\Gamma(c,t)dx = \rho c\frac{\partial}{\partial t}\Gamma(t) \; . \tag{2.21}$$

Total lift will be

$$L^{(2)}(t) = \underbrace{\rho U\Gamma(t)}_{A} + \underbrace{\rho c\frac{\partial\Gamma(t)}{\partial t}}_{B^{(2)}} \; . \tag{2.22}$$

We will seek to determine the error that is introduced by applying these approximations to determine instantaneous lift values.

From Eq.(2.6) and (2.17), we have

$$\frac{\partial}{\partial t}\Gamma(t) = \frac{\partial}{\partial t}\int_0^c \gamma(x_o,t)dx_o = \frac{\partial}{\partial t}\int_0^\pi \gamma(\theta_o,t)\frac{c}{2}\sin\theta_o d\theta_o . \tag{2.23}$$

Inserting $\gamma(\theta,t)$ from Eq.(2.5) into Eq.(2.23), and noticing that

$$\int_0^\pi \sin^2(\vartheta)d\vartheta = \frac{\pi}{2}; \qquad \int_0^\pi \sin(n\vartheta)\sin(\vartheta)d\vartheta = 0$$

yields

$$\frac{\partial}{\partial t}\Gamma(t) = \pi c[\frac{\partial}{\partial t}(UE_o) + \frac{1}{2}\frac{\partial}{\partial t}(UE_1)] \; . \tag{2.24}$$

Substituting this relation into (2.21), result in

$$B^{(2)} = \rho \int_0^c \frac{\partial}{\partial t}\Gamma(c,t)dx = \rho c \frac{\partial}{\partial t}\Gamma(t) = \rho \pi c^2 [\frac{\partial}{\partial t}(UE_o) + \frac{1}{2}\frac{\partial}{\partial t}(UE_1)] \quad . \tag{2.25}$$

Again inserting Eq. (2.10) yields

$$B^{(2)} = \pi \rho c^2 [(U\dot{\alpha} - \ddot{h}) + (1 - \frac{a}{c})c\ddot{\alpha}]. \tag{2.26}$$

$$L^{(2)}(t) = \underbrace{\pi \rho c U C(k)[U\alpha - \dot{h} + (\frac{3}{4} - \frac{a}{c})c\dot{\alpha}]}_{A} + \underbrace{\pi \rho c^2 [(U\dot{\alpha} - \ddot{h}) + (1 - \frac{a}{c})c\ddot{\alpha}]}_{B} \quad . \tag{2.27}$$

Inserting Eq. (2.13) yields

$$B^{(2)} = \rho c \frac{d\Gamma(t)}{dt} = \pi \rho c^2 [(\frac{2Uk}{c})^2 h_a \sin(\frac{2Uk}{c}t)] \quad . \tag{2.28}$$

$$L^{(2)}(t) = \underbrace{\pi \rho c U C(k)[U\alpha - \frac{2Uh_a k}{c}\cos(\frac{2Uk}{c}t)]}_{A} + \underbrace{\pi \rho c^2 [(\frac{2Uk}{c})^2 h_a \sin(\frac{2Uk}{c}t)]}_{B^{(2)}} \quad . \tag{2.29}$$

Further discussion of Eq. (2.29) can be seen in Yuan & Olinger (2002). A comparison of the resultant lifts of approximation 1 and approximation 2 to the true lift are presented in Fig. 2.7 for the case of $U=5m/s$, $\alpha = 2^0$, $h_a/c=0.05$, $k=0.35$. It is observed from the peak lift values that the quasi-steady lift, $L^{(1)}$ (Eq. (2.20)), underestimate much of the true lift, L (Eq. (2.16)). However, the lift of approximation 2, $L^{(2)}$ (Eq.(2.29)), slightly overestimates the true lift L. It is also observed that a larger phase angle exists between the lift curves L and $L^{(1)}$, and L is always leading the phase of $L^{(1)}$. However, L is always lagging the phase of $L^{(2)}$ and the phase angle between them is much small. Based on the above qualitatively comparison, we believe $L^{(2)}$ is a better approximation to the true lift.

In order to quantitatively and systematically analyze these approximations, we define $\Delta\Phi^{(1)}$ as the absolute value of phase angle between lift $L^{(1)}$ and L; $\Delta\Phi^{(2)}$ as absolute value of phase angle between $L^{(2)}$ and L. In addition to the phase angle analysis, we also need to study the amplitude errors between those lift curves. Hence, we define relative errors as

$$e^{(1)}(t) = \frac{L^{(1)}(t) - L(t)}{L(t)}; \qquad e^{(2)}(t) = \frac{L^{(2)}(t) - L(t)}{L(t)} \ . \qquad (2.30)$$

Root mean square error as

$$e_{rms}^{(1)} = \left| \frac{L_{rms}^{(1)} - L_{rms}}{L_{rms}} \right|; \qquad e_{rms}^{(2)} = \left| \frac{L_{rms}^{(2)} - L_{rms}}{L_{rms}} \right| \ . \qquad (2.31)$$

where the definition of the root mean square lift amplitude is

$$L_{rms} = \sqrt{\frac{1}{T}\int_0^T [L(t) - \overline{L(t)}]^2 \, dt} \ . \qquad (2.32)$$

Mean lift is defined as

$$\overline{L(t)} = \frac{1}{T}\int_0^T L(t) \, dt \ . \qquad (2.33)$$

Next, those observations in Fig.2.7 will be further quantified based on the definitions of phase angle and rms errors.
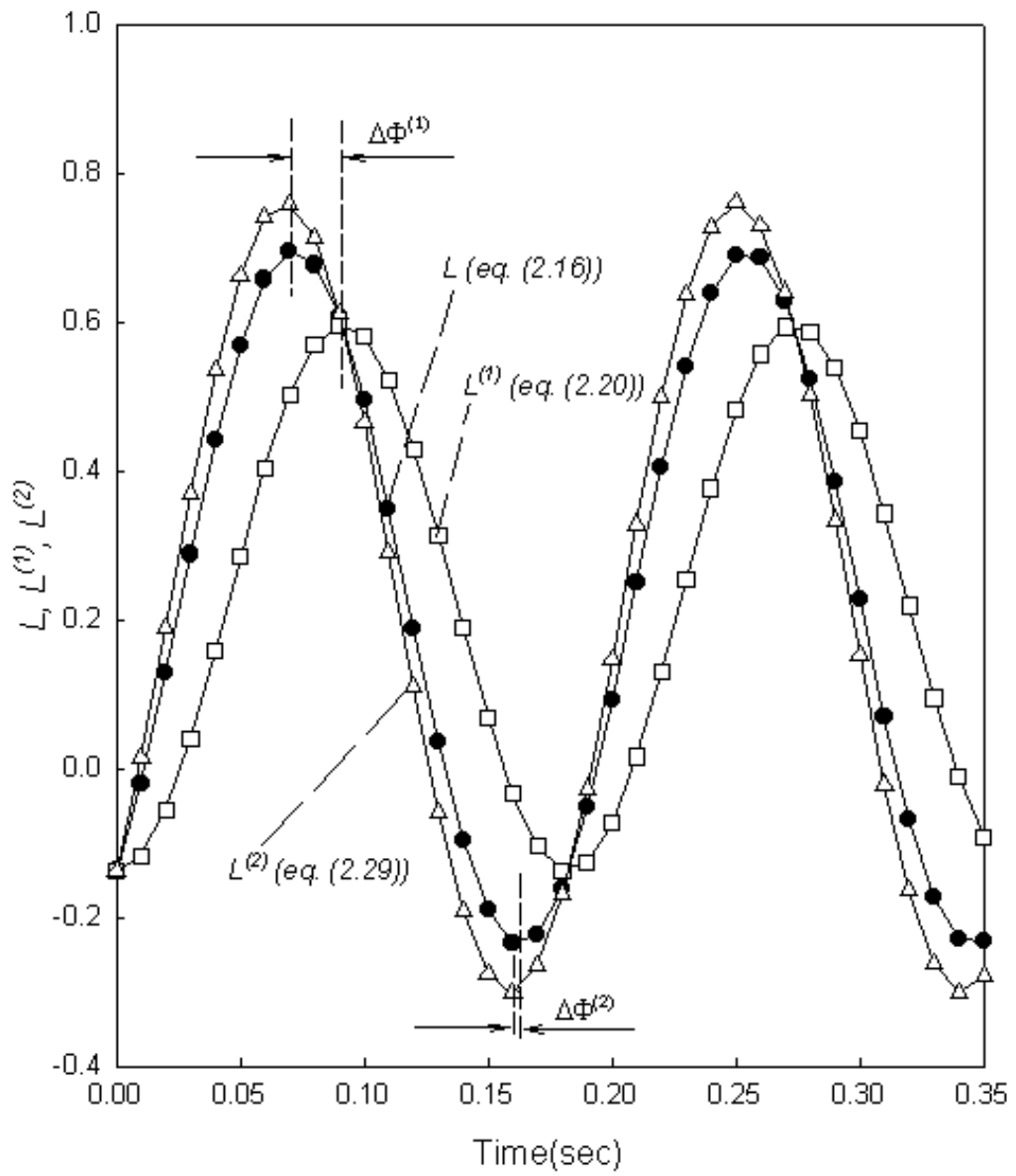
Fig. 2.7 Typical time traces of lift curves for quasi-steady (K-J) lift $L^{(1)}$, unsteady approximation $L^{(2)}$ compared to true lift curve L for oscillating plate ($U=5m/s$, $\alpha=2^0$, $k=0.35$, $h_a/c=0.05$)

2.4 Results and discussion

In this section we study the errors that are introduced (in rms lift amplitude and phase angle behavior) when the quasi-steady and unsteady approximations of the previous section are applied to an oscillating flat plate with chord length of *c=10.16cm* and *U=5m/s* to match typical experimental values attainable in typical wind tunnel tests (see chapter 5). The effects of the oscillation amplitude, initial angle of attack and the reduced frequency are studied.

The comparison of the relative errors in Fig. 2.8 shows the phase difference between $e^{(1)}(t)$ and $e^{(2)}(t)$ is almost π. Another interesting result is that at any time, the absolute value of $e^{(2)}(t)$ is always one third of $e^{(1)}(t)$, or

$$e^{(2)}(t) = -\frac{1}{3}e^{(1)}(t) \quad . \tag{2.34}$$

This clearly shows that approximation 2 is a better approximation for the unsteady plate flow.

Fig. 2.9 presents the phase angle variations with plate oscillating amplitude h_a/c, reduced frequency *k* and plate angle of attack α. For all the cases, the phase angle of approximation 2, $\Delta\Phi^{(2)}$, is always less than phase angle of approximation 1, $\Delta\Phi^{(1)}$. At a typical case of *k=0.3*, $h_a/c=0.1$, $\Delta\Phi^{(1)}$ is almost 40^0, but $\Delta\Phi^{(2)}$ is just 8^0, that means approximation 2 can improve the phase angle by almost 80% ($\frac{\Delta\Phi^{(1)} - \Delta\Phi^{(2)}}{\Delta\Phi^{(1)}} \approx 80\%$).

This shows that approximation 2 is more accurate than approximation 1 (quasi-steady K-J approximation). The behavior of phase angle variation shows that they do not change

with the plate oscillating amplitude and angle of attack (Fig. 2.9a, Fig 2.9c), but increase with the increase of the plate reduced frequency (Fig. 2.9b).

Fig. 2.10 presents the variations of rms errors of those approximations with plate oscillating amplitude h_a /c, reduced frequency k and plate angle of attack α. Fig. 2.10a and Fig 2.10b show that $e_{rms}^{(1)}$ and $e_{rms}^{(2)}$ increase with the increase of plate oscillating amplitude h_a /c and reduced frequency k, but decrease with the plate angle of attack (Fig. 2.10c). The reason can be found from Eq. (2.16), (2.20) and (2.29), the capability of the unsteady term contributes much to the total lift with the increase of plate oscillating amplitude and frequency, compared to the quasi-steady term. However, with the increase of angle of attack, the contribution from the quasi-steady term increases, hence the effects of the unsteady term relatively decreases, this cause the rms errors decrease with angle of attack. From quantitative comparison, $e_{rms}^{(1)}$ is always larger than $e_{rms}^{(2)}$ for all the cases. At a typical case of $k=0.4$, h_a /c=0.1, $e_{rms}^{(1)}$ is almost 0.3, but $e_{rms}^{(2)}$ is just 0.191, that means approximation 2 can improve the rms error by almost 35%. This again confirms that approximation 2 is a more accurate than the quasi-steady K-J approximation 1 for unsteady lift prediction. Hence, approximation 2 is more favorable and we will study $e_{rms}^{(2)}$ variation in detail next.

Fig. 2.11 presents the 3D plots of $e_{rms}^{(2)}$ variation with plate angle of attack α, vibration amplitude h_a /c and reduced frequency k. The general trend is that $e_{rms}^{(2)}$ decrease with plate angle of attack, this can be observed from change of $e_{rms}^{(2)}$ peak values from $e_{rms}^{(2)}=0.22$ at $\alpha=2^0$ to $e_{rms}^{(2)}=0.11$ at $\alpha=8^0$. Another characteristic is $e_{rms}^{(2)}$ decreases with

decrease of plate oscillating amplitude h_a /c and reduced frequency k. This 3D plots also show that $e_{rms}^{(2)}$ may reach unacceptable high values ($e_{rms}^{(2)} > 15\%$) for specified larger plate oscillating amplitude and reduced frequency. This fact will motivate further development of a corrected unsteady approximation later in section 2.5.

So far, we know that approximation 2 is favored and the behavior of its rms error $e_{rms}^{(2)}$ variation with plate oscillating amplitude, reduced frequency and plate angle of attack. However, in real UCMT experiments, it should have some guidance for initial test design so that the errors may be kept in a reasonable range at first. This needs more quantitative data of $e_{rms}^{(2)}$ and we present them in Fig. 2.12, the 2D contour of $e_{rms}^{(2)}$ as a function of k, h_a /c and α. If we define $e_{rms}^{(2)} \leq 5\%$ as acceptable domain of the combination of k and h_a /c at different AOA, these 2D contours can clearly show the acceptable area and unacceptable area ($e_{rms}^{(2)} \geq 5\%$). Interesting is that the unacceptable domain dramatically decreases with the increase of AOA, this contributes to the decrease of the contribution from unsteady term B and increase of contribution from quasi-steady term A, with increase of AOA. This kind plot can guide investigators using UCMT for quick estimation of errors to be introduced in experiments.

49
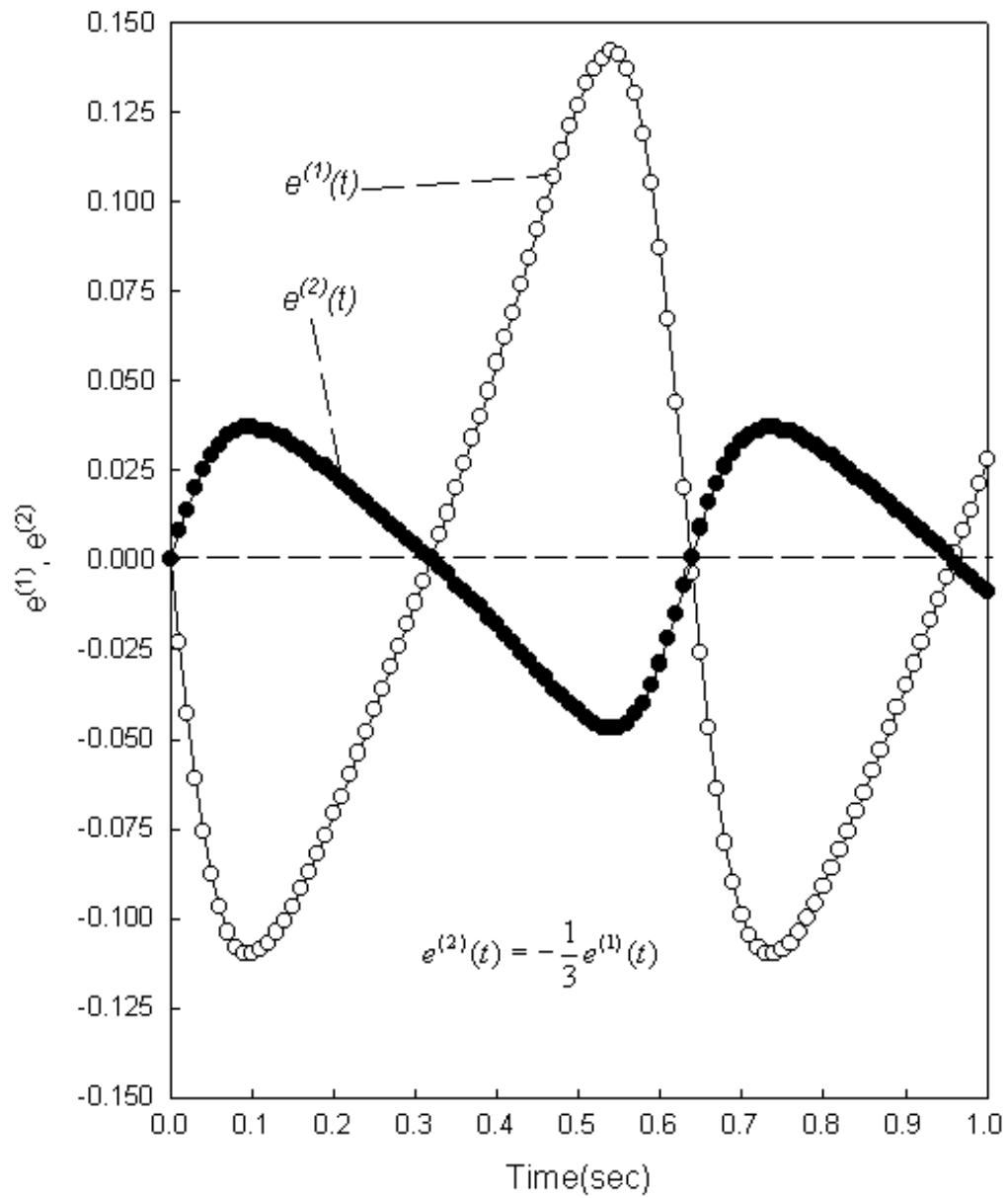
Fig 2.8 Time traces of the relative errors for approximation 1 and approximation 2 for the case of $U=5m/s$, $\alpha=2^0$, $k=0.1$, $h_a/c=0.1$.
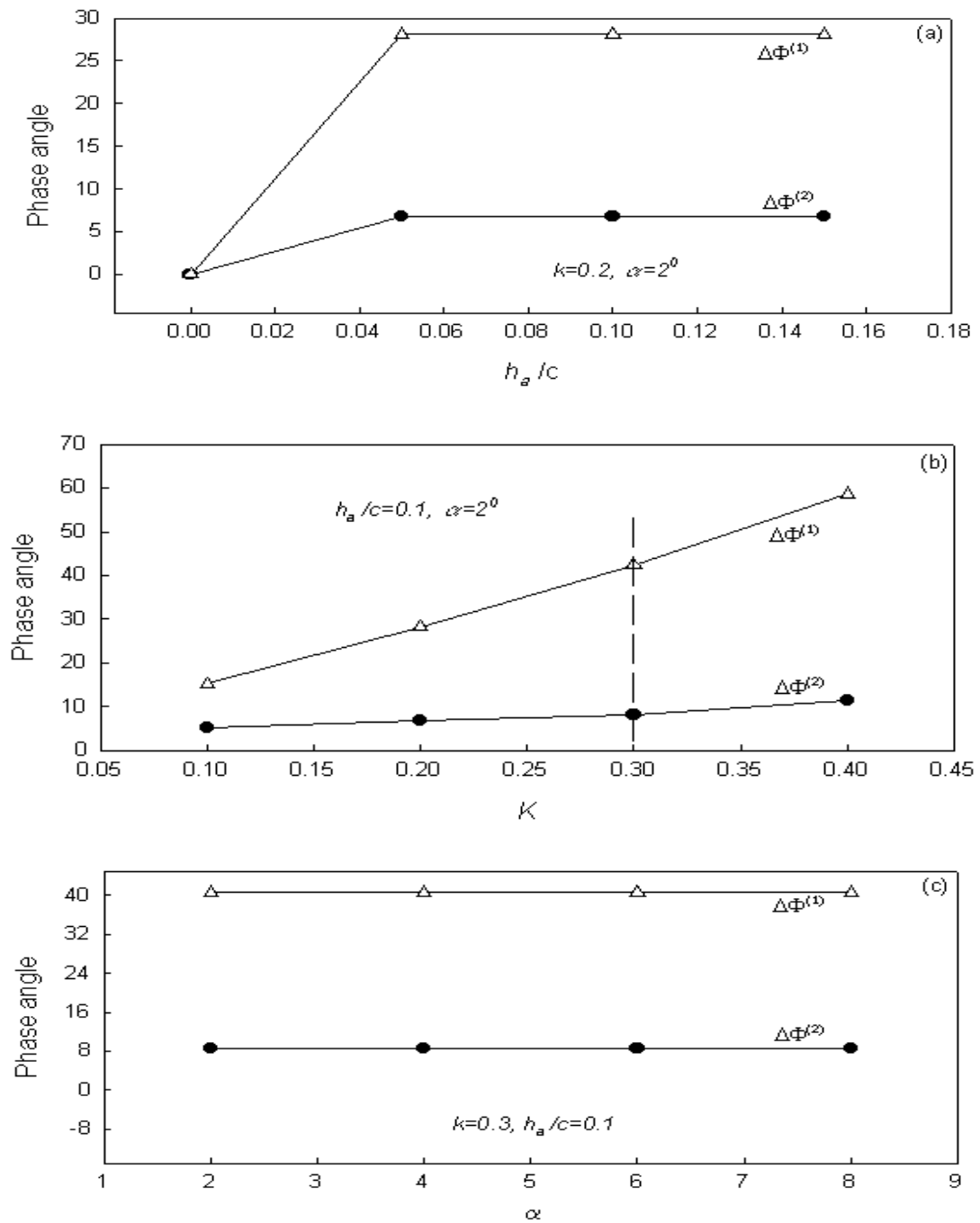
Fig 2.9 Variation of phase angle with key parameters. a) effect of plate oscillating amplitude

h_a/c . (b) effect of reduced frequency k. (c) effect of angle of attack α.
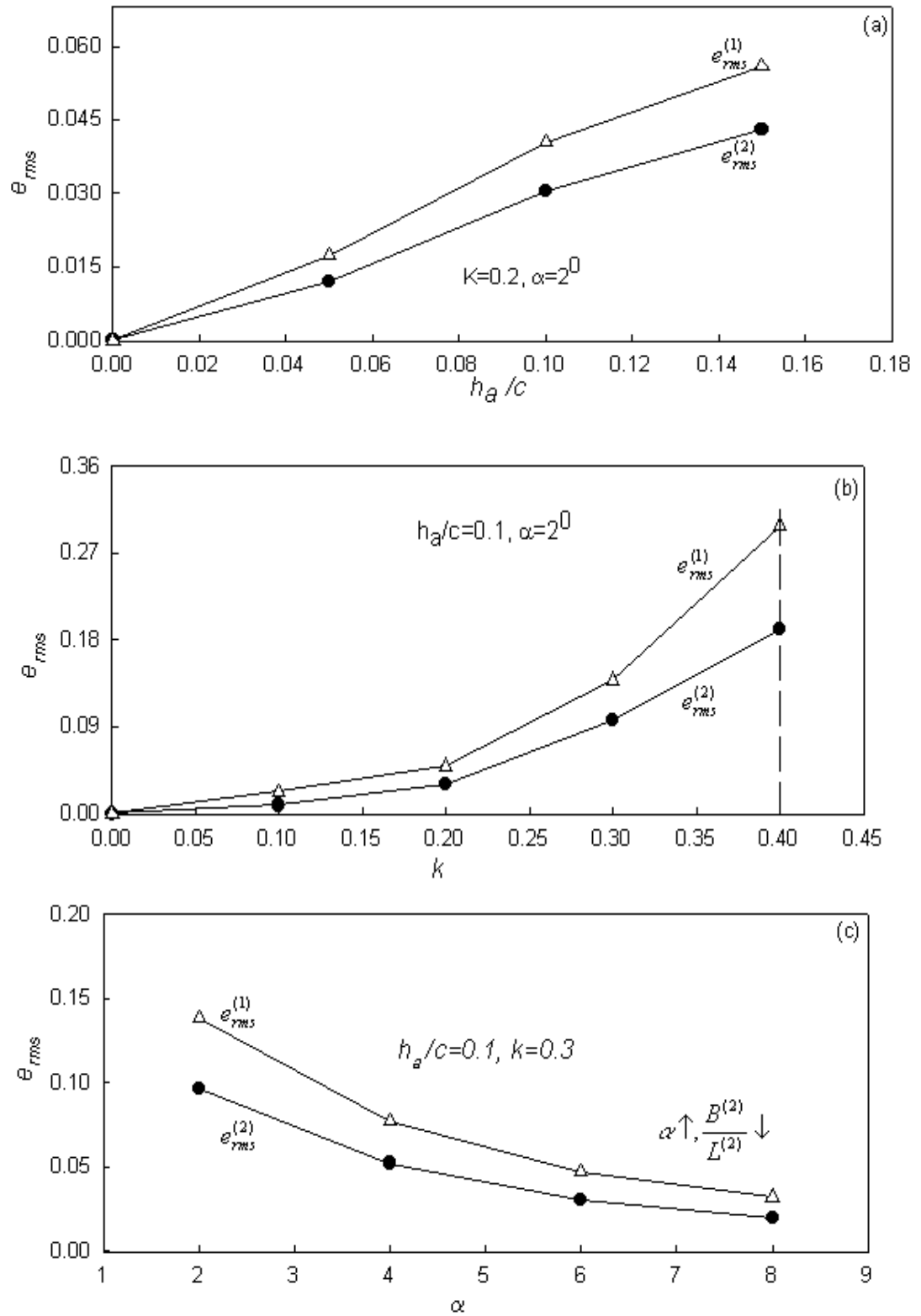
Fig 2.10 Variation of rms error with key parameters. (a) effect of plate oscillating amplitude h_a/c. (b) effect of reduced frequency k. (c) effect of angle of attack α.

52

(a) $\alpha=2^0$

(b) $\alpha=4^0$

(c) $\alpha=6^0$

(d) $\alpha=8^0$
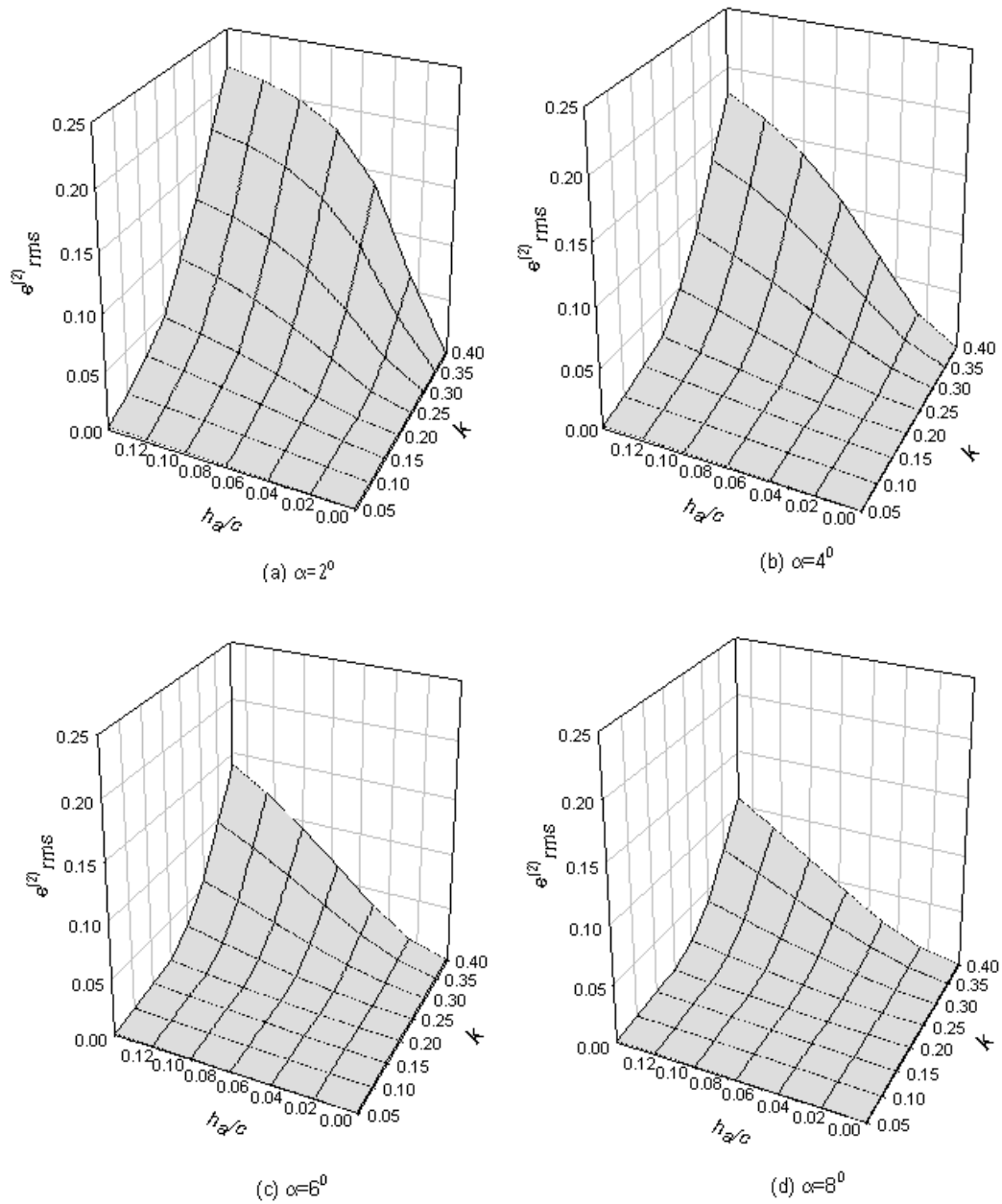
Fig. 2.11 3D plots of $e^{(2)}_{rms}$ variation with plate oscillation frequency k, amplitude h_a/c at different angle of attack α.
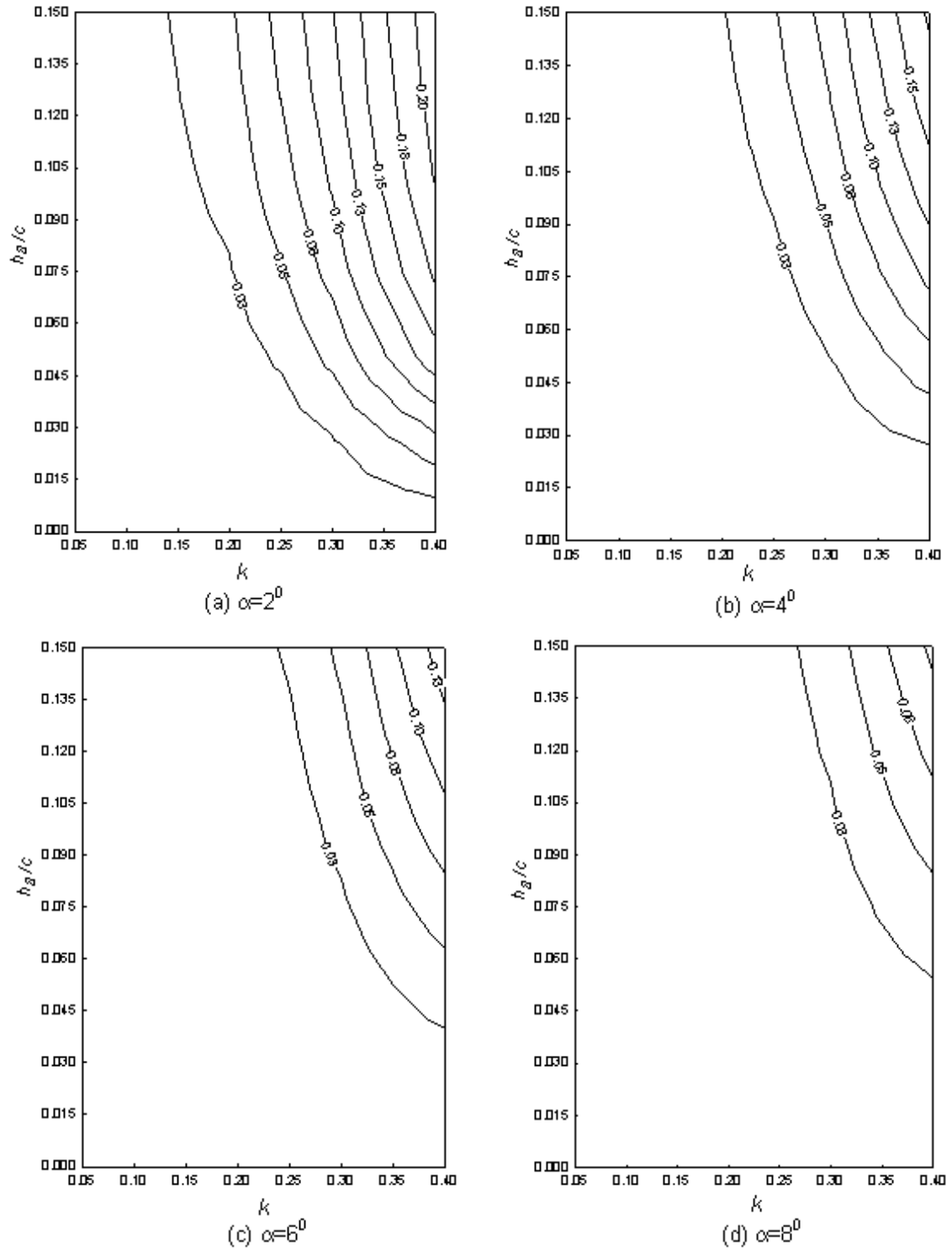
Fig. 2.12 Contour of $e_{rms}^{(2)}$ variation with plate oscillating frequency k, amplitude h_a/c at different angle of attack α.

2.5 Corrected unsteady approximation

The previous section has detailed the effects of including the unsteady term (B) in Eq. (2.3) on the resultant lift about an unsteady oscillating flat plate. It, therefore, serves as a guide for determining whether inclusion of the unsteady term B as opposed to a quasi-steady approximation is appropriate.

Analysis in previous sections does verify that inclusion of the unsteady term is appropriate and approximation 2 is more favorable. However, in this section, we will extend our results to develop a 'corrected' unsteady approximation for predicting lift more accurately. Previously we have

$$B = \pi \rho c^2 [\frac{3}{4}(\frac{2Uk}{c})^2 h_a \sin(\frac{2Uk}{c}t)] \quad . \tag{2.15}$$

$$B^{(2)} = \rho c \frac{d\Gamma(t)}{dt} = \pi \rho c^2 [(\frac{2Uk}{c})^2 h_a \sin(\frac{2Uk}{c}t)] \quad . \tag{2.28}$$

$$L^{(2)}(t) = \underbrace{\rho U \Gamma(t)}_{A} + \underbrace{\rho c \frac{\partial \Gamma(t)}{\partial t}}_{B^{(2)}} \quad . \tag{2.22}$$

If we define R (see appendix A) as unsteady correction factor as

$$R = \frac{B}{B^{(2)}} \quad . \tag{2.35}$$

Then accurate lift can be expressed as

$$L^{(3)}(t) = \underbrace{\rho U \Gamma(t)}_{A} + \underbrace{R \rho c \frac{d\Gamma(t)}{dt}}_{B} \quad . \tag{2.36}$$

From Eq. (2.15) and (2.28), yields R value for oscillating plate as

$$R = \frac{B}{B^{(2)}} = \frac{3}{4} \quad . \tag{2.37}$$

Eq. (2.36) will be the key equation for properly converting the measurable bound circulation $\Gamma(t)$ to instantaneous lift $L(t)$ in circulation based methods such as UCMT, PIV and LDV. It will serve as an important result in our further studies in unsteady flow. Comparison of Eq. (2.36) and Eq. (1.17) shows that the B term in Eq. (2.36) is similar to the final unsteady term in Sarpkaya's lift equation. In chapter 3, we will utilize numerical simulation of flow over an oscillating flat plate at low Reynolds number to validate the effectiveness of the corrected unsteady approximation of Eq. (2.36) in determining instantaneous lift values. However, prior to this, we would like to first show that this framework can be applied to other unsteady flows in next section.

2.6 Correction in other unsteady flows

In this section, we will present our analytical results for plunging flat plate flow, pitching flat plate flow and summarize results of Katz & Plotkin (1991) for impulsive started plate flows. The goal is to expand our understanding of lift approximations to other unsteady flows.

2.6.1 Plunging flat plate flow

This type of flow has been studied with UCMT experiments by Purutyan (1990), we try to confirm if quasi-steady K-J approximation was appropriately used in the UCMT lift determination.

The motion of the plate can be described with following equation

$$\left.\begin{aligned}
&\alpha = const. \\
&h(t) = h_0 - (\frac{h_0 - h_1}{t_c})t, 0 \leq t < t_c \\
&h(t) = h_1, \qquad t \geq t_c
\end{aligned}\right\} .$$

(2.38)

Here h_0, h_1 are the plate initial and final (altitude) locations, t_c is the plate plunging time (Fig 2.13). A similar derivation (see Appendix A) as discussed in section 2.3, yields

$$\left.\begin{aligned}
&R = 0; \quad B = 0 \\
&L(t) = \underbrace{\rho U \Gamma(t)}_{A}
\end{aligned}\right\} .$$

(2.39)

The result shows that for plunging plate flow, no unsteady correction is necessary, and the quasi-steady K-J approximation can predict the lift force accurately.
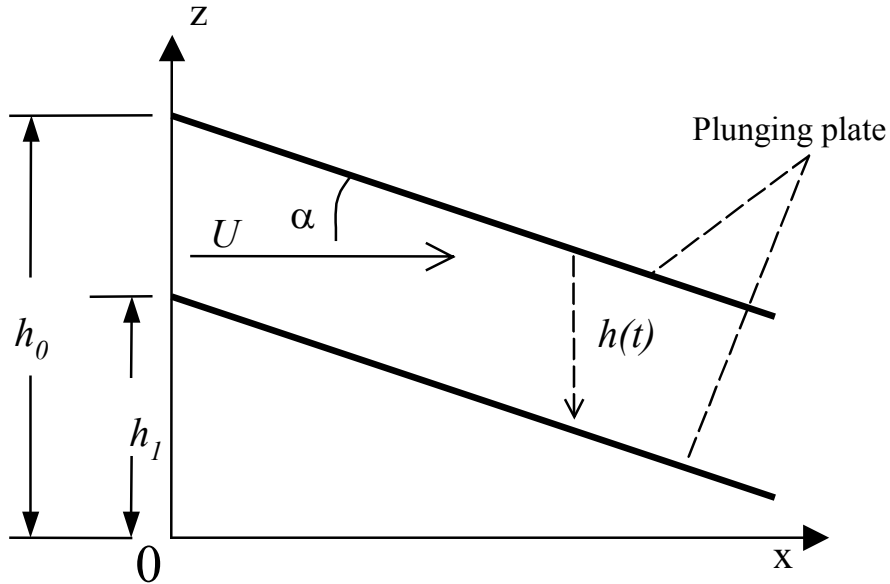
Fig. 2.13 Schematic of a plunging flat plate

2.6.2 Pitching flat plate flow

In this case, the flat plate undergoes a periodic pitching motion about a pivot axis located at $x=a$, and the motion of plate can be expressed as

$$\alpha = \alpha_o + \alpha_a \sin(\omega t); \qquad h = h_0 = \text{constant}.$$ (2.40)

Here α_0 is the plate's initial angle of attack before the oscillating, and α_a is the oscillation amplitude (Fig. 2.14). Weber (1995) studied this flow with UCMT techniques. The lift force was converted from bound circulation with a quasi-steady K-J approximation.
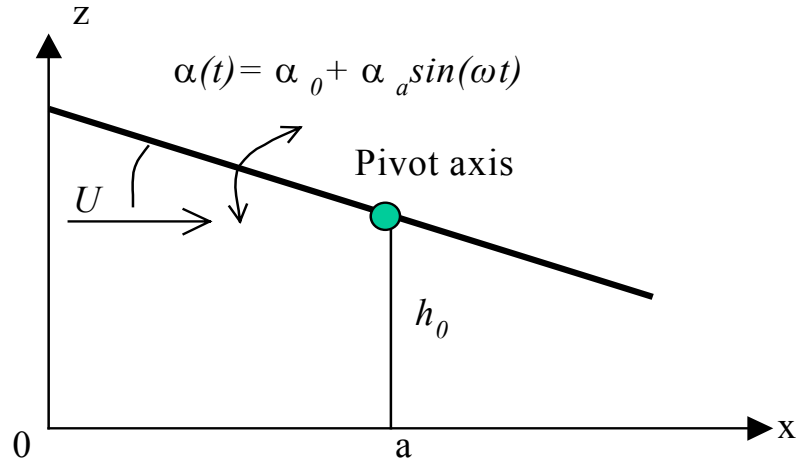
Fig. 2.14 Schematic of pitching plate flow

Using the same mathematical manipulation, yield

$$
\left.
\begin{array}{l}
A = \pi\rho c U C(k)[U\alpha_o + U\alpha_a \sin(\dfrac{2Uk}{c}t) + c(\dfrac{3}{4} - \dfrac{a}{c})(\dfrac{2Uk}{c})\alpha_a \cos(\dfrac{2Uk}{c}t)] \\[3mm]
B = \pi\rho c^2[\dfrac{3}{4}U\alpha_a(\dfrac{2Uk}{c})\cos(\dfrac{2Uk}{c}t) - c(\dfrac{1}{2} - \dfrac{a}{c})\alpha_a(\dfrac{2Uk}{c})^2 \sin(\dfrac{2Uk}{c}t)] \\[3mm]
B^{(2)} = \pi\rho c^2[U\alpha_a(\dfrac{2Uk}{c})\cos(\dfrac{2Uk}{c}t) - c(1 - \dfrac{a}{c})\alpha_a(\dfrac{2Uk}{c})^2 \sin(\dfrac{2Uk}{c}t)] \\[3mm]
R = \dfrac{B}{B^{(2)}} = f(k,U,\dfrac{a}{c},t)
\end{array}
\right\}.
$$ (2.41)

Here the unsteady correction coefficient R is a complex function of reduced frequency, pivot location and freestream velocity. Hence, for this flow, an unsteady correction is more difficult to apply. However, $R \neq 0$ means that effect of the unsteady term B exists and quasi-steady K-J approximation can not predict lift accurately.

2.6.3 Impulsively started plate flow

We have studied unsteady correction term for oscillating plunging and pitching plates in our work, and found appropriate R values for each flow. Wagner (1925) and Katz & Plotkin (1991) also studied an impulsively started plate flow using similar techniques. Wagner (1935) places a single vortex flow at the plate quarter chord point to model circulation on the plate. Here we summarize their results.

The motion for this flow can be expressed as (Fig 2.15)

$$\left.\begin{array}{ll} u = 0, & t = 0 \\ u = U, & t > 0 \end{array}\right\}. \qquad (2.42)$$
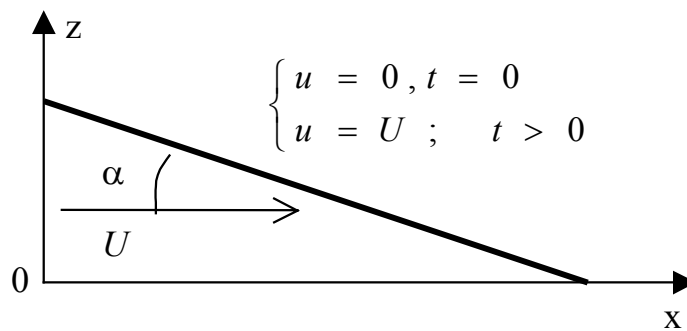
Fig. 2.15 Schematic of a impulsively started plate flow

59

Katz & Plotkin (1991) summarized the work of Wagner (1925), found that

$$\left. \begin{aligned} R &= \frac{B}{B^{(2)}} = 1 \\ L(t) &= L^{(2)}(t) = \underbrace{\rho U \Gamma(t)}_{A} + \underbrace{\rho c \frac{d\Gamma(t)}{dt}}_{B^{(2)}} \end{aligned} \right\} . \tag{2.43}$$

The results show that for impulsively started plate flows, approximation 2 can be used for lift prediction.

2.7 Summary

The work in this chapter leads to an important corrected unsteady approximation for instantaneous lift prediction in unsteady flows with low amplitude and frequency motions, given by

$$\boxed{L^{(3)}(t) = \underbrace{\rho U \Gamma(t)}_{A} + \underbrace{R \rho c \frac{d\Gamma(t)}{dt}}_{B}} . \tag{2.36}$$

This equation is the basis for our research work in this thesis. The value of unsteady correction factor R has been established for different unsteady flows.

The focus was on oscillating flat plate flow in this chapter. The results for this flow show that quasi-steady K-J approximation can not predict unsteady lift accurately. Our corrected unsteady approximation improves the lift prediction. We derived a concise expression for unsteady correction coefficient as $R = \dfrac{3}{4}$. The behavior of the phase angle and rms error can provide guidance for investigators using circulation method (UCMT) to keep measurement errors in a reasonable range. We found that

- The phase angle increased with plate reduced frequency, but was independent of oscillation amplitude and plate angle of attack.

- The rms error increased with increase of plate oscillation amplitude and reduced frequency, but decreases with angle of attack.

We also studied other types of unsteady flow using the framework developed for oscillating plate flow. The focus was on the determination of R for plunging plate flow, pitching plate flow and sudden accelerating plate flow. We found $R=0$ for plunging plate flow and $R=1$ for an impulsively started plate flow. However, for a pitching plate, R is a complex function of plate oscillating frequency, pivot location and freestream speed. It is more difficult to correct the unsteady lift for this type of flow.

In next chapter, we would like to apply numerical methods to further validate our developed corrected unsteady method. The advantages of numerical methods used to accomplish this will be described in chapter 3.

Chapter 3

Validation of Corrected Unsteady Approximation
Using Numerical Simulation

3.1 Introduction

In the previous chapter, we developed a method to properly convert the instantaneous circulation measurements (attainable in UCMT experiments) into the instantaneous lift force for several unsteady flows. We verified the Kutta-Joukowski theorem is only suitable for steady flows, though some of researchers still use it to investigate unsteady flows (Obasaju, Bearman and Graham, 1988; Weber, 1995; Unal, Lin and Rockwell, 1997). From our work in last chapter, we have learned that unsteady effects play an important role in lift force determination. Most importantly, we developed a method for determining the unsteady part of the lift due to the measurable bound circulation. In this chapter, we intend to further verify this corrected unsteady approximation by studying numerical simulation of flow over an oscillating flat plate. In these simulations, we will mimic the acoustic path used in UCMT experiments to determine bound circulation $\Gamma(t)$ which will be converted to lift $L(t)$ using the developed methods of chapter 2.

We pursue numerical simulations for several reasons. While our eventual goal is application of the corrected unsteady approximation in UCMT experiments, verification of the results of chapter 2 through numerical simulation has certain advantages. First, numerical simulation provides an independent method to determine instantaneous lift force, namely integration of stress tensor along the surface of aerodynamic body. This

method does not depend on measurement of circulation. This independent lift measurement is more difficult in experiments. Current deficiencies in force balance techniques have already been discussed in chapter 1. Secondly, in a numerical simulation the geometry of the mimicked acoustic sound path can be easily altered. This is important because the effect of varying acoustic path on the resulting circulation measurements has never been systematically studied in UCMT work. Because of the viscous dissipation effect, the circulation obtained within an enclosed curve far away from the body is zero, as it is for a curve along the exact surface of the lifting body due to no-slip boundary condition. This suggests that $\Gamma(t)$ measurement may be acoustic path sensitive. The acoustic path variation is difficult to apply in UCMT experiments. As a result, a primary goal of this chapter is to study this aspect of unsteady UCMT measurements. Finally, numerical simulations provide detailed velocity/vorticity field that can be used to determine the instantaneous circulation $\Gamma(t)$ by integrating tangential component of velocity vectors along the acoustic path. Hence, numerical simulation becomes our choice for investigating these issues.

In this section, we used a numerical simulation based on the Galerkin finite element method as the main tool for our study on an oscillating flat plate flow. The first goal is to verify the corrected unsteady approximation of chapter 2. The second goal is to study how the size varying and location of the closed acoustic path alters the bound circulation determination. The main function of the numerical simulation is to provide the unsteady flow field. Given this velocity field, an algorithm is developed to obtain the instantaneous bound circulation along different paths. Finally, we may validate our

developed correction method through comparison with the lift force obtained through pressure and stress integration.

3.2 Numerical formulation

The governing equations for an incompressible viscous flow that are solved in the finite element simulations are the continuity equation and Navier-Stokes equation

$$\nabla \cdot \mathbf{u} = 0. \tag{3.1}$$

$$\mathrm{Re}\frac{D\mathbf{u}}{Dt} = \nabla \bullet \sigma . \tag{3.2}$$

where $\sigma = -p\mathrm{I} + \tau$ is the stress tensor. Velocity vector $\mathbf{u}$ is non-dimensionalized using freestream velocity U, lengths with the chord length of the flat plate c, and time with c/U.

The numerical grids are generated through PATRAN software and shown in Figure 3.1, the mesh near the plate is much finer so that the detailed near wake flow information can be captured. The boundary conditions of the computational domain are set as follows. At the inlet, upper and lower grid boundaries, velocity is set as the free-stream velocity. At the surface of the plate, the no-slip condition is maintained. At the outlet boundary, a constant pressure condition is utilized following Malamataris (1991) and Olinger & Alexandrou (1995). The plate is aligned horizontally in line with the x-axis, the angle of attack is controlled through changing the free-stream incidence relative to the chord of the flat plate. Based on the principle of relative motion, the oscillating plate motion $h(t) = h_0 + h_a \sin(\omega t)$ can be applied numerically through an oscillating free-stream flow at the inlet boundary with velocity
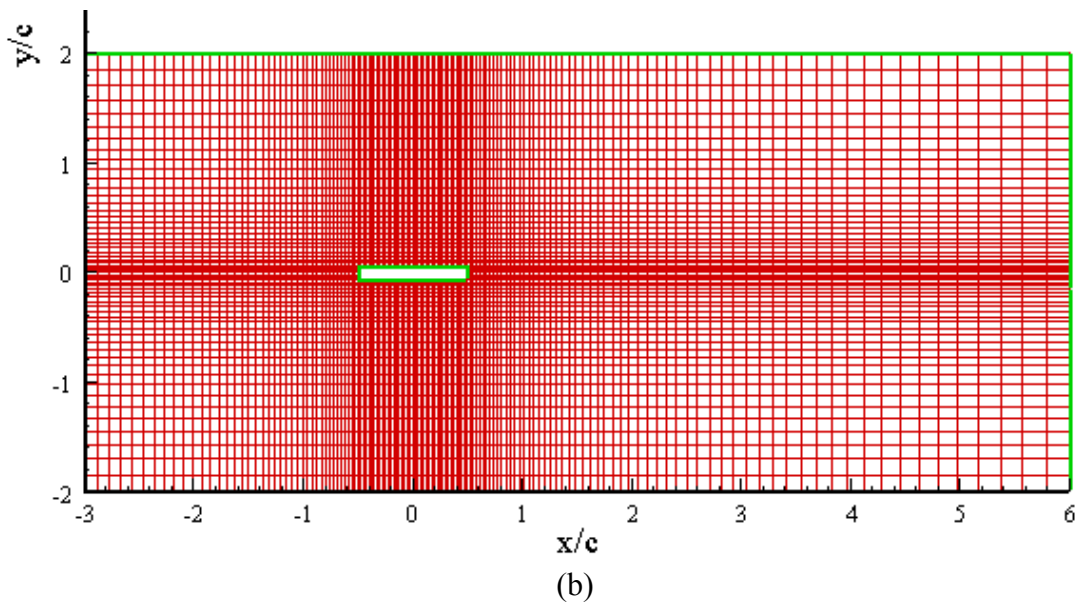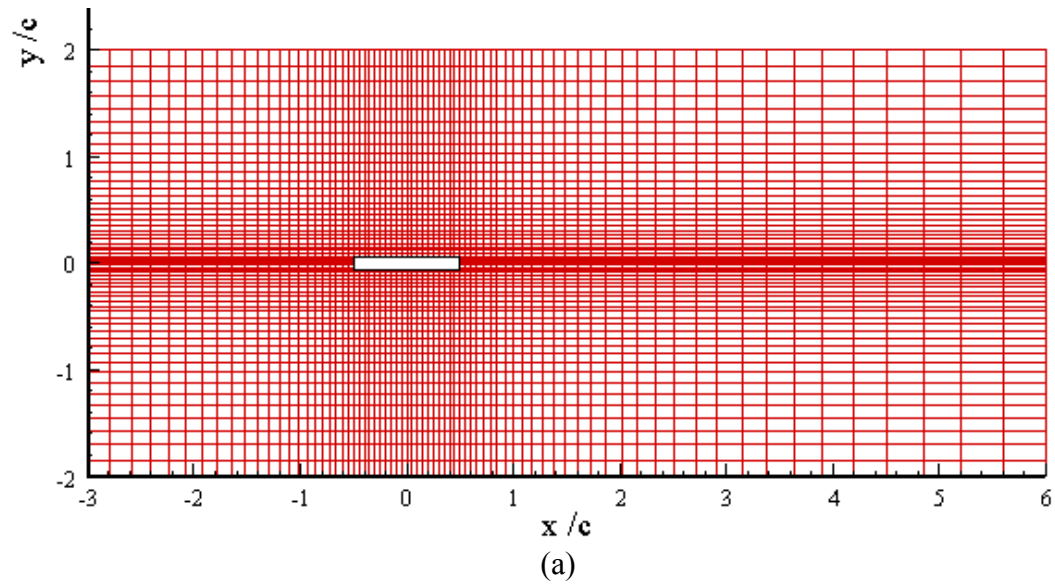
Fig 3.1 Numerical grids used in the finite element simulations for a domain –3<x/c<6, -2<y/c<2
(a) grid 1: NM=1043, NND=4330, (b) grid 2: NM=1970, NND=8124

$$u = U\cos(\alpha); \quad v = U\sin(\alpha) + h_a\omega\cos(\omega t); \quad \omega = \frac{2Uk}{c}. \tag{3.3}$$

here α is the angle of attack, k the reduced frequency, ω the angular frequency, U the free-stream velocity. u, v are the resultant velocity in x and y direction.

The non-linear Navier-Stokes equations are solved by using a classical Galerkin Finite Element approach, which has the advantage of unstructured meshes, element-by-element formulation and processing, simplicity and rigor of boundary conditions being incorporated with sophisticated automatic mesh generation, adaptive meshing and re-meshing, economical storage and improved solution techniques both in speed and accuracy (Lohner et al, 1984). The two primary unknowns, pressure and velocity, are solved using a segregated solution procedure, in which the conservation equations are solved to provide an intermediate velocity field at each time station through an explicit step after an initial guess for the pressure field

$$R_e \frac{\partial u_{p+1}^{n+1}}{\partial t} = (-R_e u\nabla \cdot u + \nabla \cdot \sigma)_p^{n+1} . \tag{3.4}$$

here n is the time counter, p the iteration counter. After applying the divergence theorem and integrating over the whole domain V, equation (3.4) can be written in finite element form as

$$\int_V \phi_i R_e \frac{\partial u_{p+1}^{n+1}}{\partial t} dV = \int_V (\phi_i[-R_e u\nabla \cdot u] - \sigma \cdot \nabla\varphi_i) dV + \int_A (\phi_i \sigma \cdot n)_p^{n+1} dA . \tag{3.5}$$

The mass conversation equation can be written as

$$\nabla \cdot (u_{p+1}^{n+1}) = 0 . \tag{3.6}$$

By combing Eq. (3.6) with (3.4), we can get the following equation

$$\nabla \cdot (R_e \ddot{u}_{p+1}^{n+1}) = 0 = \nabla \cdot (-R_e u \nabla \cdot u + \nabla \cdot \sigma)_p^{n+1} \ . \tag{3.7}$$

Substituting the stress tensor $\sigma = -p\mathrm{I} + \tau$, and applying the divergence theorem, equation (3.7) can be expressed as

$$\int_V \nabla \phi_i \cdot \nabla P dV = \int_V (-R_e u \nabla \cdot u + \nabla \cdot \tau)_{p+1}^{n+1} \cdot \nabla \phi dV - \int_A R_e \ddot{u}^{n+1} \cdot n dA \ . \tag{3.8}$$

The term $\nabla \cdot \tau$ can be evaluated separately as $\lambda = \nabla \cdot \tau$ by using finite element form

$$\int_V \phi_i \lambda dV = -\int_V \tau \cdot \nabla \phi dV + \int_A \phi_i \tau \cdot n dA \ . \tag{3.9}$$

For each time step, the iteration procedure is repeated within the same iteration loop until convergence is achieved, and the velocity field and pressure distribution at that time step is available for post processing. The traction vector is integrated over the body surface to calculate the resultant lift force at each time instant. The major parameters input to the FEM solver include Reynolds number, plate angle of attack, oscillating amplitude and reduced frequency. Further detailed information about the numerical scheme can be seen in Olinger et al (1995).

3.3 Circulation determination

Generally, circulation can be obtained through the line integration of velocity along a closed path, as long as the velocity field data is known. With the velocity field data at each time-step provided by the FEM solver introduced in section 3.2, we can calculate the circulation value along a mimicked ultrasound path in the flow. A description of the algorithm for circulation determination follows.
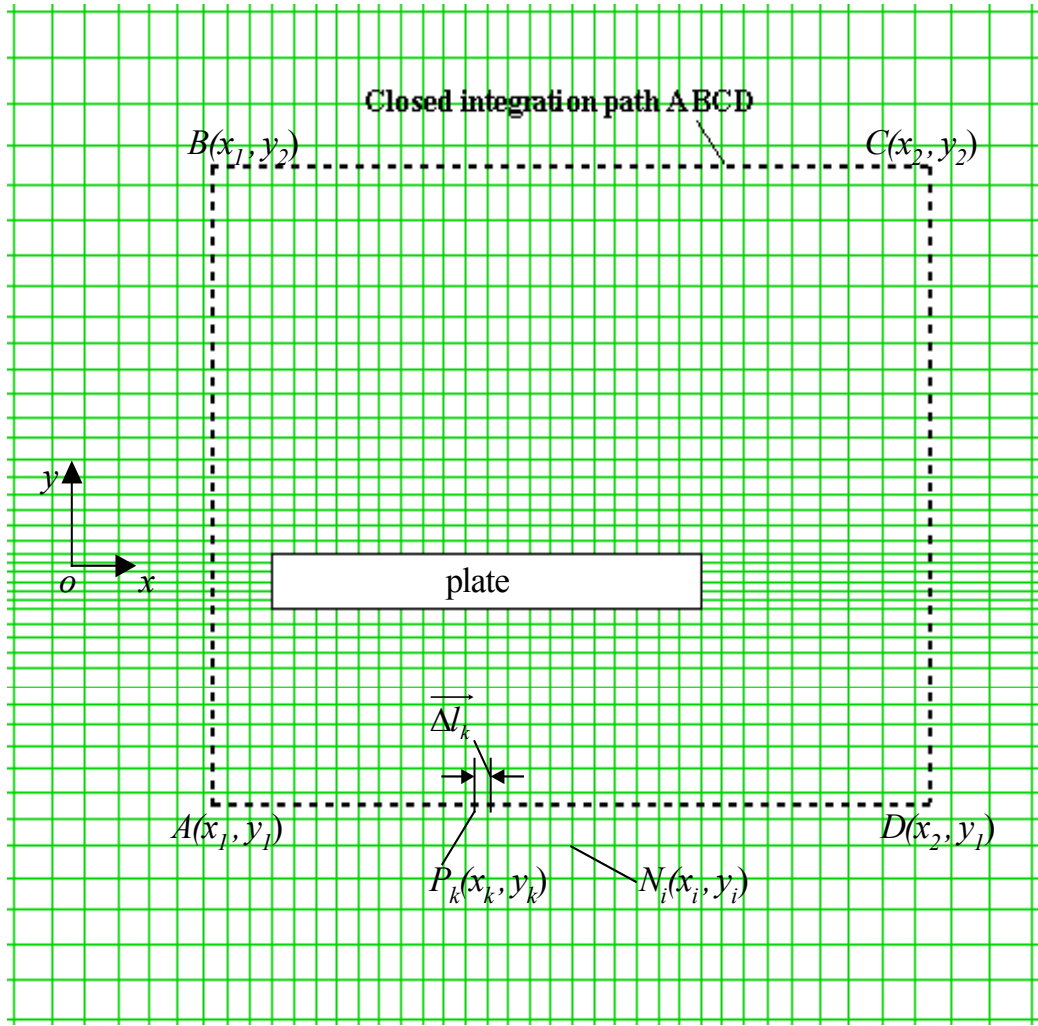
Fig 3.2 Schematic of circulation determination

Suppose a rectangular integration path is constructed with four points $A(x_1,y_1)$, $B(x_1,y_2)$, $C(x_2,y_2)$, $D(x_2,y_1)$, and the coordinates x_1, y_1, x_2, y_2 are arbitrarily selected in order to study the size and location of the ultrasound path effects on determination (Fig.3.2). The circulation in the area enclosed by $ABCD$ can be obtained through the following expression with discrete method the bound circulation

$$\Gamma_{ABCD} = \oint_{ABCD} \vec{V} \cdot \vec{dl} = \sum_{k=1}^{M} \vec{V}_{P_k} \cdot \overrightarrow{\Delta l_k} \ . \tag{3.10}$$

where P_k represents any points which is located on the ultrasound path, $\vec{V}_{Pk}$ means the velocity at point P_k (x_k,y_k) ($x_1 \le x_k \le x_2$; $y_1 \le y_k \le y_2$). The parameter $\overrightarrow{\Delta l_k}$ is the infinitesimal distance along the path at point P_k, and M is the total number of the discrete points on the closed path.

Due to arbitrarily selection of the ultrasound path $ABCD$, the coordinates of point P_k (x_k,y_k) may not match any one of the mesh nodes at which the velocity and pressure data are determined. Hence, we use the flow information at the nearest node to represent the flow at P_k. The nearest node is determined by finding the minimum distance between P_k and node $N_i(x_i, y_i)$ through

$$l_{ki} = \left| P_k N_i \right| = \sqrt{(x_k - x_i)^2 + (y_k - y_i)^2} \quad . \tag{3.11}$$

Here N_i represents an arbitrary node position in the computational domain, l_{ki} is the distance between point P_k and N_i. When l_{kj} reaches a minimum value, then that node in the domain will be selected as the most representative of point P_k on the ultrasound path, The velocity at that node is then used to calculate the circulation around the arbitrarily selected path $ABCD$. A subroutine was developed and inserted into the FEM

solver introduced in section 3.2 to provide the circulation value at any time step. These methods will be used for further validation of the analytical results of chapter 2 for unsteady lift force determination.

3.4 Code validation

The finite element simulation of viscous flow over an oscillating flat plate is conducted at Reynolds numbers (based on plate chord-length) on the order of 100. The study is conducted at low Reynolds numbers to avoid complexities arising from turbulent, three-dimensional flows, such as the need for phase-average of lift measurements. Also, since our correction methods are based on inviscid theory, we believe that a highly viscous flow at low Reynolds number represents a 'worst-case' scenario, and that the developed correction method would yield even better results for higher Reynolds number flows. The low Reynolds number also implies large boundary layer thickness. This will become important in our later acoustic path sensitivity study where we wish to resolve the effect of the boundary layer on determined circulation values. Also, many open questions regarding vortex formation and flow-induced vibration still exist even at these low Reynolds numbers.

Before any further study, the numerical codes must be first validated to ensure that simulation results are grid and time step independent. This validation is conducted for flow around a stationary flat plate at angle of attack $\alpha=6^0$ first, then for plate oscillating with non-dimensional amplitude as $h_a/c=0.05$ and reduced frequency $k=0.15$, with intention to check if the numerical code can provide reasonable lift force
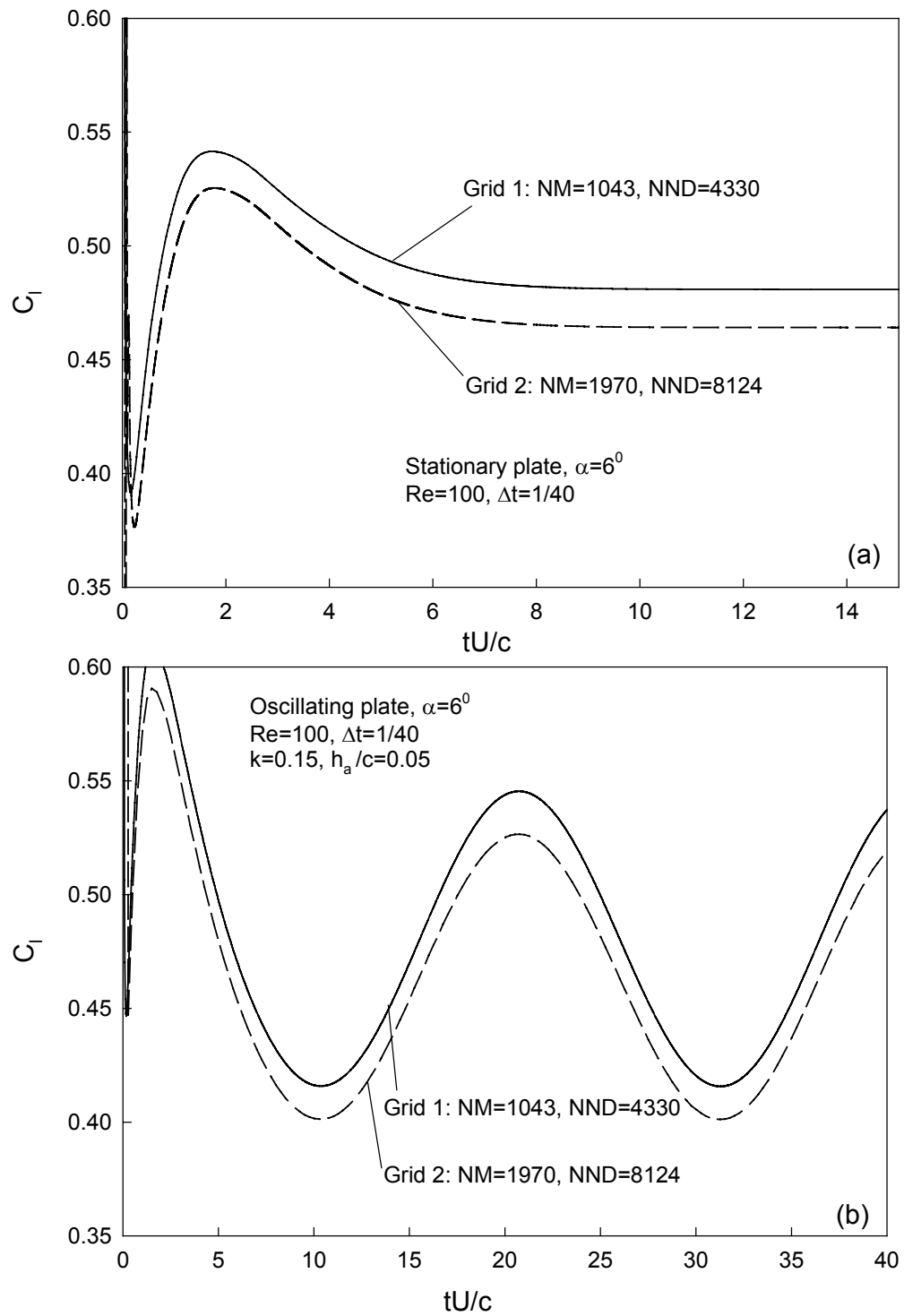
Fig. 3.3 Grid effect on results with Δt=1/40, (Grid 1: NM=1043,NND=4330; Grid 2: NM=1970, NND=8124). (a) Stationary plate. (b) Oscillating plate with k=0.15, h$_a$/c=0.05

predictions that are independent of grid and time steps resolution. The plate thickness is set at $t/c=0.12$. This was done to preliminarily incorporate some airfoil thickness effects (that will occur in experiments) into the flow, while also eliminating some numerical difficulties (mesh generation).

3.4.1 Grid effects

The numerical grid resolution may affect the final numerical results dramatically. Theoretically, higher resolution grids yield more accurate results. However, increase in grid resolution will increase the CPU run time for the codes. Hence, a proper grid should be selected that fulfills both requirements of providing accurate results with reasonable CPU running time.

Here we study two grids as shown in Fig 3.1. The number of elements for grid 1 is *NM1=1043*, total nodes number is *NN1= 4330*. Grid 2 essentially doubles the grid resolution of grid 1, with *NM2=1970, NN2=8124*.

Fig 3.3 presents this comparison. The trend of the numerical data for a stationary plate in Fig. 3.3 (a) is similar; the lift forces will gradually converge to a final constant lift coefficient after the initial transient process. Grid 1 results in $\overline{C_L} \cong 0.4808$; grid 2 leads to $\overline{C_L} \cong 0.4642$. That means the difference between them is about 3.6%. Fig. 3.3(b) shows the grid effect on lift for a sinusoidal oscillating plate with amplitude $h_a/c=0.05$ and reduced frequency k=0.15. After the initial transient period of time, the lift curves gradually follow the sinusoidal nature of the plate motion. The lift coefficient from grid 1 is always larger than that from grid 2. However, the difference between
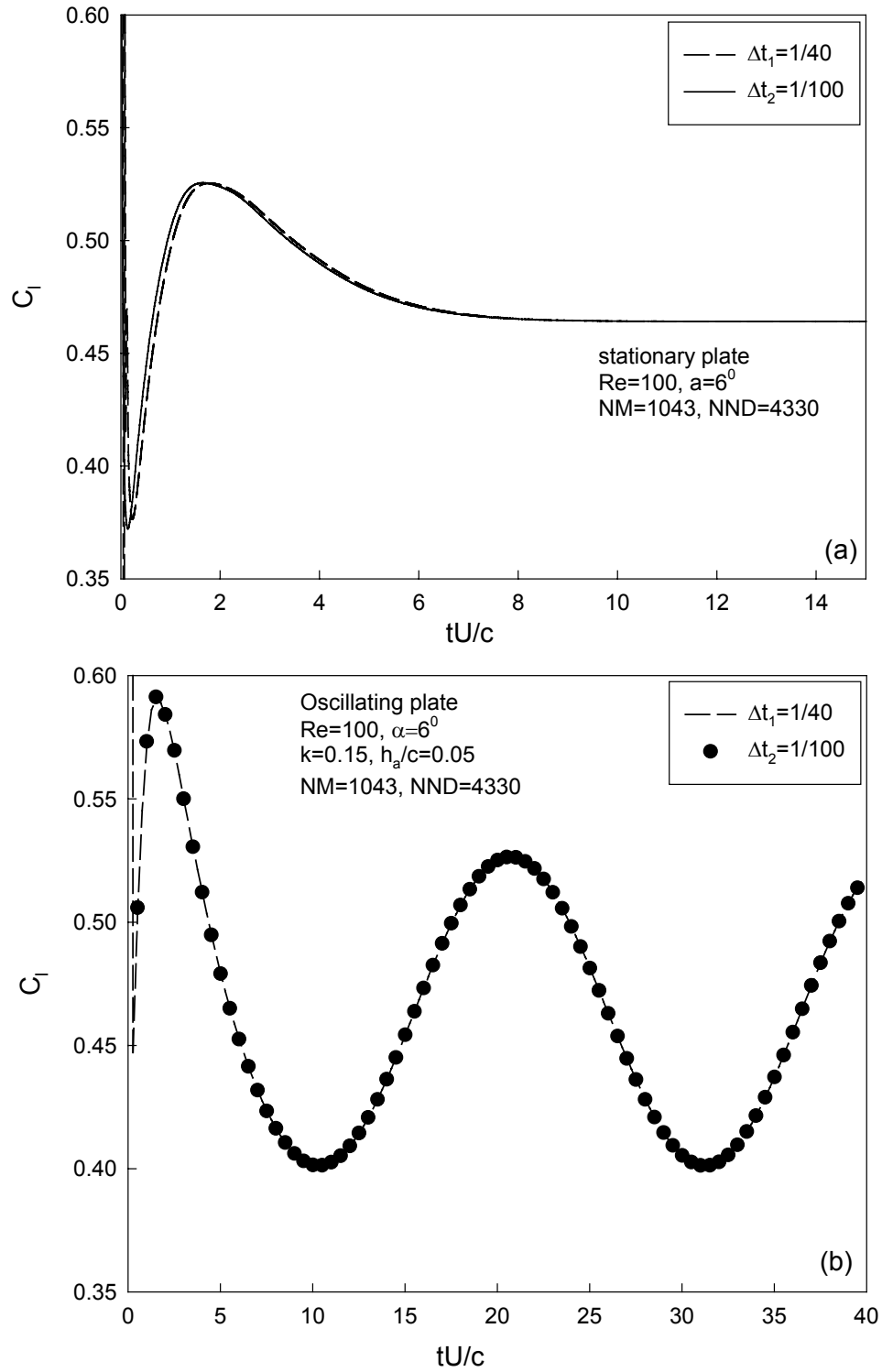
Fig 3.4 Time step effects on the results with Grid1:NM=1043, NND=4330, $\alpha=6^0$ (Δt_1=1/40, Δt_2=1/100). (a) For stationary plate. (b) For oscilating plate at k=0.15 and h_a/c=0.05.

them is approximately 3.6%, same as the difference in Fig.3.3 (a) for the stationary plate. With such small difference exist between these two grids and consideration of shorter running time, we select grid 1 to be used in our numerical simulation.

3.4.2 Time step effects

We also studied the effect of varying the time step on the numerical results. We seek to determine an optimum time step balancing the conflicting trends of more accurate solution but longer codes running times with smaller time steps.

Fig 3.4 presents the time traces of the lift forces for $\Delta t_1 = 1/40$ and $\Delta t_2 = 1/100$. The numerical solutions are largely independent of the variation in time step, hence $\Delta t_1 = 1/40$ will be used in the present work in order to yield shorter run times. The final grid and grid are set as grid 1 ($NM=1043, NND=4330, \Delta t_1 = 1/40$).

Beyond the validations and convergence studies described here, we also note that the same numerical formulation and similar resolution grids have been used in numerical studies of oscillating cylinder flows in Olinger et al (1993) and Olinger et al (1995).

3.5 Bound circulation determination

3.5.1 Background

In this section, we address in detail the issue of whether UCMT circulation measurements in viscous flows are dependent on the chosen acoustic path (for example, paths C_1 and C_2 in Fig 3.5). This acoustic path sensitivity was introduced earlier, but has

never been addressed in a systematic fashion. In a study of forces, circulation and vortex patterns around a circular cylinder in oscillating flows, Obasaju, Bearman and Graham (1988) determined the bound circulation through velocity measurement along a square closed path around a circular cylinder, with the leg length as 1.35d (d is cylinder
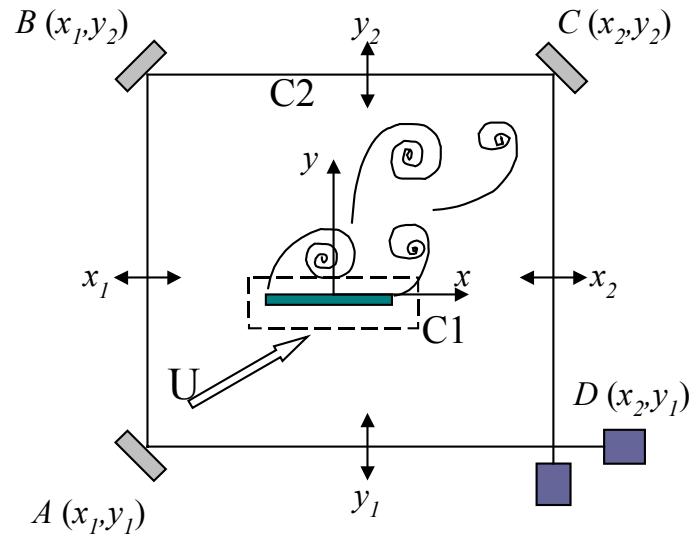
Fig 3.5 Schematic of sound path effects on bound circulation determination

diameter), however no justification was given for this selection. In a study of evaluation of time-dependent fluid dynamic forces on bluff bodies, Noca (1997) used a momentum-based control volume formulation to process velocity fields measured through the Particle Image Velocimetry technique. Different results were obtained with three domains of different size, and the author indicated that the largest domain couldn't yield right answer. In the investigation of bound and wake circulation on a helicopter rotor, Bhagwat & Leishman (2000) measured the circulation with Laser Doppler Velocimetry techniques. They pointed out that circulation measurements are very sensitive to the shape and size of the integration path, but offered no satisfactory

guidelines for choosing the right integration paths. Hence, a systematic study of path

selection in force determination through circulation methods is needed.

3.5.2 Effect of closed integration path variation

As introduced in last section, the lack of previous guidelines for acoustic path

selection, to some extend, is the result of the lack of systematical study of the path size

effects, due to the limitations in experiments to adjust the path size. However, in

numerical simulations, the path size and location can be easily adjusted, as introduced

in section 3.3.

Arbitrarily, we can select any closed path around the body, composed by four

corners at $A(x_1, y_1)$, $B(x_1, y_2)$, $C(x_2, y_2)$, $D(x_2, y_1)$ in Fig. (3.5). We chose to fix three of the

legs, and then study the circulation variation when changing the location of the

remaining leg. Here we present the results in Fig 3.6 for flow around a stationary plate

at angle of attack of 6^0. Fig.3.6 (a) presents the circulation variation with movement of

leg AB. Fig3.6 (b) (c) (d) shows similar results for variation of leg CD, AD and BC. In

Fig 3.6(a), but characteristics of all the plots, we see that a stable region exists where

the circulation result is independent of the precious location of the leg, and these stable

regions can provide a basis for path selection. The fast drop of bound circulation with

the increase if distance away from leading edge may be due to some numerical

boundary effects on bound circulation values. In Fig. 3.6(b), x_2 /c leg must remain in

near wake to avoid effect of shed vorticity in wake. In Fig. 3.6(c) and (d), the stable

regions have some relation with the thickness of boundary layers. We estimated the thickness of boundary layer at the plate trailing edge based on equation

$$\frac{\delta}{c} = \frac{5.2}{\sqrt{\text{Re}}} \ .$$

(3.13)

it yields $\delta/c = 0.52$ for Re=100. Considering the thickness of the plate $t/c = 0.12$ and the origin of coordinate system is located in center of the plate, the thickness of boundary layer above and under plate should be $y_\delta/c = \pm 0.58$ and this has been marked in Fig. 3.6c and Fig. 3.6d. The relative location between boundary layer and the stable regions suggest that the path selection should be at the edge of the boundary layer, and this is reasonable and consistent with inviscid potential flow theory used for developing our corrected unsteady method in chapter 2. In potential flow, 'surface velocity' is at the body surface, but in real viscous flow, it is actually at edge of the boundary layers. These findings also have implications for PIV and LDV studies. For example, due to resolution and body interference problem, it's hard to obtain the vorticity values within boundary layers in PIV and LDV studies. For bound circulation determination, it should be a good method to use $\Gamma = \oint \vec{V} \cdot \vec{dl}$ on a path just outside the boundary layer to replace the traditional method using $\Gamma = \iint \vec{\omega} \cdot \vec{dA}$ operated within boundary layers. Based on the results from Fig. (3.6), we schematically present the reasonable region for acoustic path selection shown in shadow region in Fig. (3.7).

While these results are obtained at a single angle of attack $\alpha=6^0$, we believe they will provide reasonable estimates for proper path selection for angle of attack in the
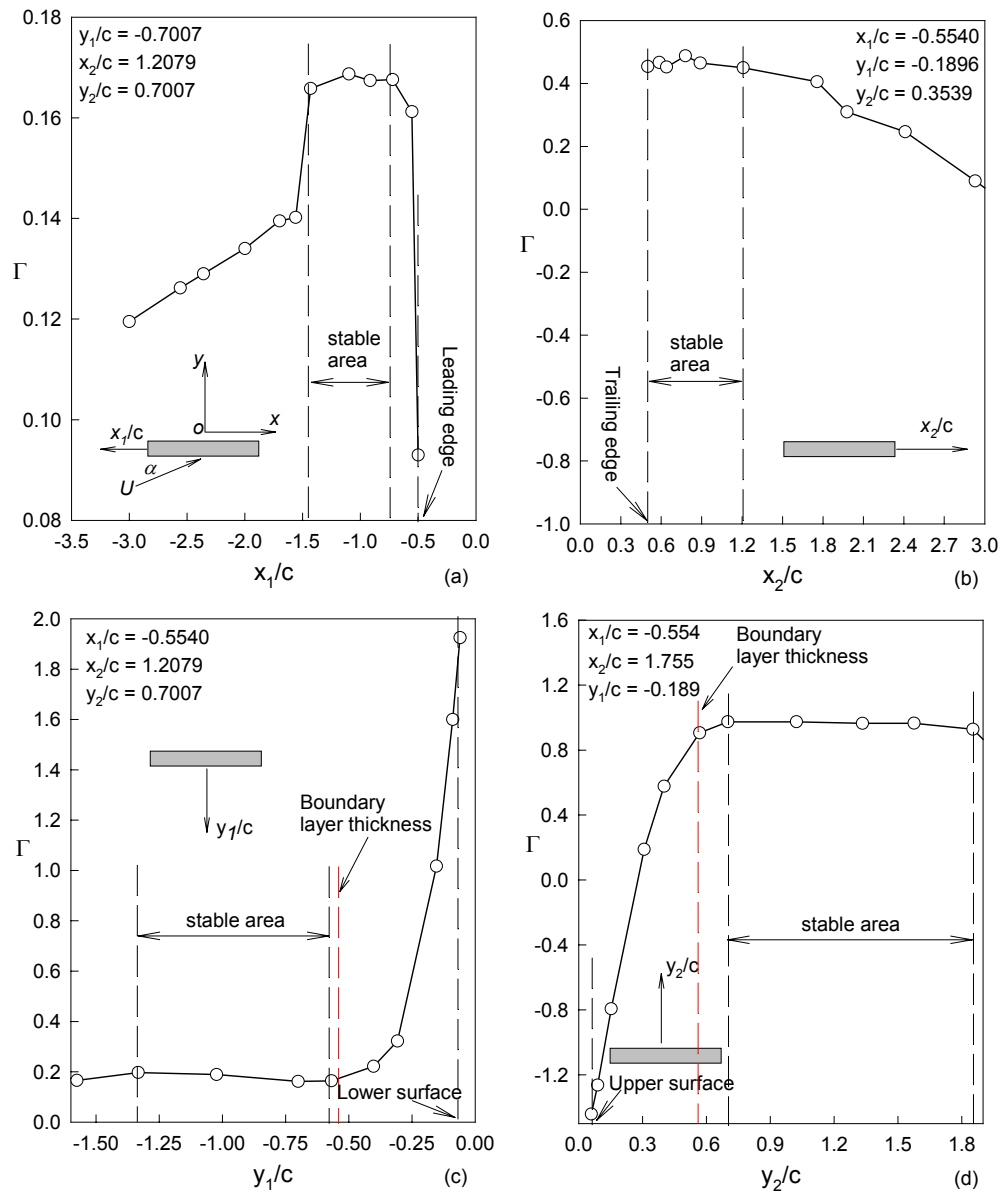
Fig 3.6 Circulation variation with the movement of each leg of 'mimic' acoustic path
(reference to Fig 3.5, $\alpha=6^0$)(a) Before leading edge; (b) After trailing edge;
(c) Away from lower surface; (d) Away from upper surface

Fig 3.7 Schematic of required acoustic path size and locations to make circulation measurements path independent. Oscillating plate flow at Re=100, $\alpha=6^0$.
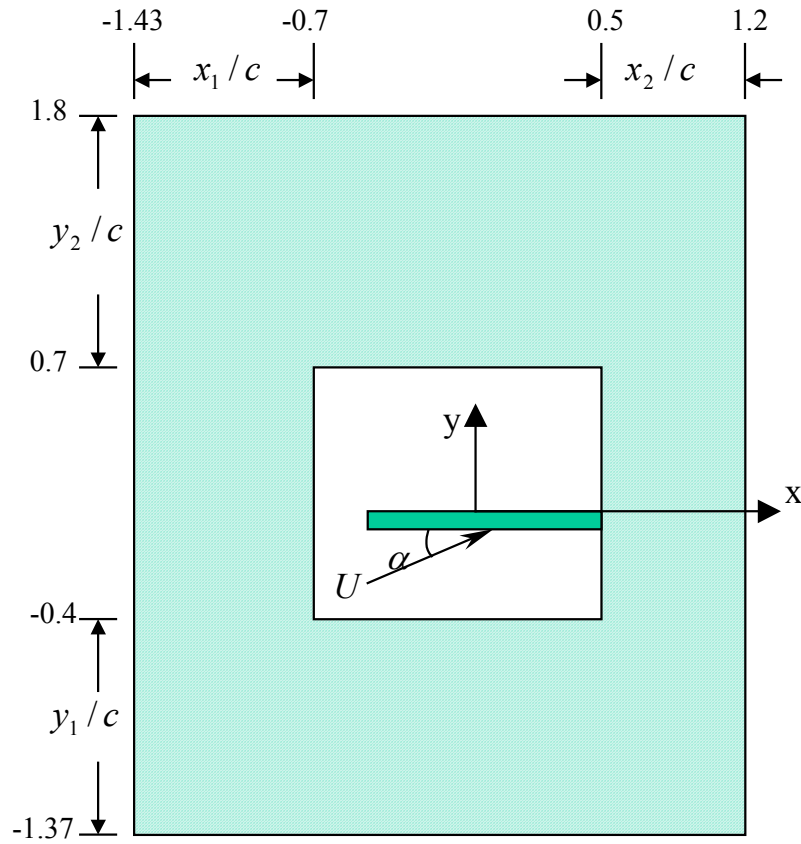
$$\frac{x_1}{c} \le -0.7; \ \ 0.5 \le \frac{x_2}{c} \le 1.2 \ ; \ \frac{y_1}{c} \le -0.4; \ \ 0.7 \le \frac{y_2}{c}$$

Optimum path: $x_1/c = -0.7208; x_2/c = 0.8893;$
$y_1/c = -0.5689; y_2/c = 0.7007$

streamlined flow region below the stall angle. From this study, the proper closed path selected is set as $x_1= -0.7208c$, $x_2 = 0.8893c$, $y_1= -0.5689c$ and $y_2= 0.7007c$ for the reminder of the numerical work on the flat plate. In the present work, we have not repeated the path sensitivity study for oscillating plate flows. However, we point out that in our numerical simulations we study low amplitude oscillations with $h_a/c < 0.15$, this is the range for which the theory of chapter 2 applied. If this oscillation amplitude is added to the boundary layer thickness, the 'new' boundary layer thickness will be $y_2/c \cong 0.7$, it still remains within the stable region of Fig 3.6(d). As a result, the same closed path will be used when plate oscillation effects are introduced into the numerical simulation.

These path selection guidelines will aid in sound path design in future UCMT experiments. We note the additional criterion that in UCMT experiments, one often strives to reduce the total acoustic path length in order to maximize acoustic pulse signal-ratio and sampling frequency. Beyond its usefulness in the present and future UCMT studies, this systematic study of the sensitivity of results to variation of integration path has broader implications for PIV and LDV studies. Investigations where local velocity and vorticity data are integrated over an enclosed region can be benefit from the present results.

3.6 Results for oscillating plate flow

In this section, we present the results from numerical simulations on a flat plate at a single intermediate value of angle of attack $\alpha=6^0$. While a widen variation in α

could be conducted, we point out that the unsteady potential flow theory leading to the unsteady correction methods of chapter 2 is only valid within the limited AOA region below stall ($\alpha \leq 10^0$). Also study of AOA variation in the analytical work of chapter 2 showed smooth, monotonic variation in results (rms error amplitude, for example) over a wider range of $2^0 \leq \alpha \leq 8^0$. As a result we would not expect to see dramatic quantitative difference in results in this section if a larger range bracketing the intermediate AOA was studied. The unsteady correction methods of chapter 2 are incorporated as follows. The bound circulation $\Gamma(t)$, from Eq. (3.10), is determined at each time step. The quasi-steady approximation (K-J theorem) of equation (2.18), along with the corrected unsteady approximation (Eq. (2.36))

$$L^{(1)} = \rho U \Gamma(t) \quad . \tag{2.18}$$

$$L^{(3)}(t) = \rho U \Gamma(t) + R\rho c \frac{d\Gamma(t)}{dt} . \tag{2.36}$$

are used to convert the numerical bound circulation $\Gamma(t)$ into appropriate lift values.

The reduced frequency of the oscillating plate was set at four values k=0.1, 0.2, 0.3, 0.4. Amplitude was set at three values h_a /c=0.05,0.1, 0.15. The numerical grid and time step are set at NM=1043, NND=4430, and Δt=1/40 as discussed in our validation studies.

Fig 3.8 (a)-(e) presents the flow fields, presented with contour of u-component of velocity field, around the oscillating plate at five time instants of one cycle with α=6^0, h_a/c=0.15, k=0.15 and Re=100. The corresponding lift values in Fig. 3.8(f) shows the periodic variation due to the plate oscillating in a harmonic style, this can be
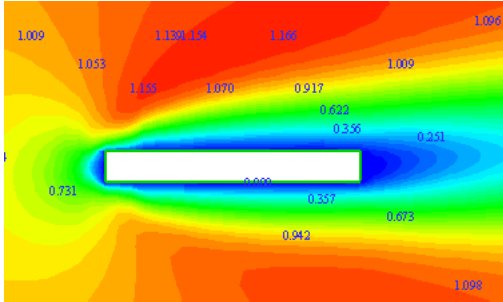
(a) tU/c= 10.325
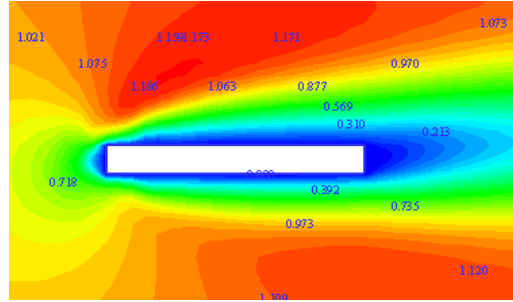
(b) tU/c= 15.252
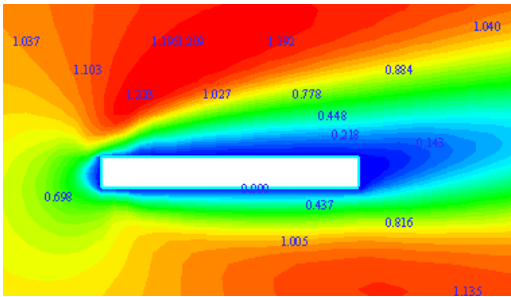
(c) tU/c= 20.7
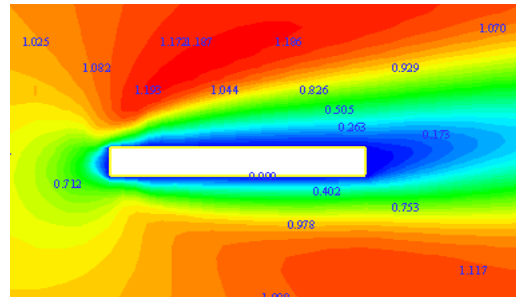
(d) tU/c= 26
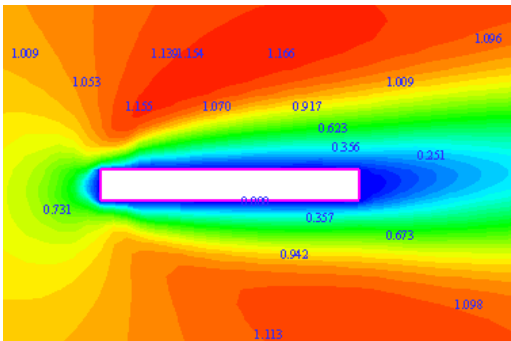
(e) tU/c= 31.3
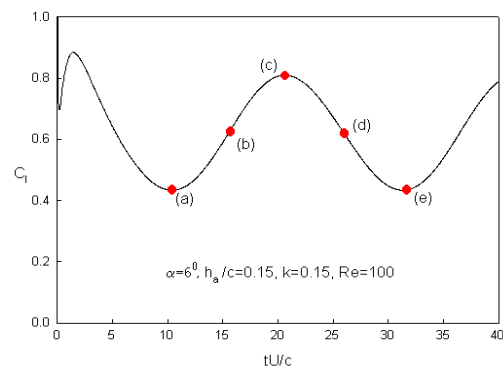
(f) time trace of lift

Fig 3.8 Flow visualization represented by contour of u-component of velocity in the field around a flat plate with $\alpha=6^0$, h_a /c=0.15, k=0.15 and Re=100. The flow fields a, b, c, d, e correspond to five specific times lift in one cycle of the lift time trace.

judged from the almost same values of both lift and flow fields at (a) and (e). From these flow fields, we see the cavities attached to the plate, not the separation bubbles for steady flow, due to two reasons. On is larger thickness of the plate $t/c=0.12$ and another reason is the unsteady oscillating of the plate. Due to the existence of a cavity behind the plate instead of a open separated boundary layer, the calculation based on laminar boundary (from Eq.(3.13)) overestimates the boundary layer thickness. Hence, the selected optimum closed path is appropriate enough for circulation determination. In addition, Fig. (3.8) shows that the numerical code can provide good information for our studies.

Fig 3.9 presents a typical time trace of the numerical bound circulation $\Gamma(t)$ and plate instantaneous location h(t). The plate non-dimensional amplitude is set as $h_a/c = 0.1$, reduced frequency as $k=0.4$, $\alpha=6^0$ and Re=100. The bound circulation shows a periodic variation after a short transient time. The phase of the plate motion is always leading the phase of the bound circulation. This is the reasonable result because the plate motion affects the wake dynamics leading to the fluid loading through circulation as discussed in chapter 1.

Fig 3.10 is a typical time trace of the lift forces and the plate instantaneous location from the numerical simulation. The quasi-steady lift $C_l^{(1)}$, corrected unsteady approximation $C_l^{(3)}$, and the true lift coefficient C_l obtained from plate surface stress integration are all presented. Plate non-dimensional amplitude is set at $h_a/c = 0.1$, reduced frequency as $k=0.4$ and $\alpha=6^0$. After the initial transient period, the lift forces also are periodic in nature following the periodic motion of the plate. The phase of the

plate location is always leading the phase of the true lift C_l by approximate a quarter of

a cycle ($\frac{\pi}{2}$). The phase difference, $\Delta\Phi^{(1)}$, between the true integrated lift and the quasi-

steady lift is larger than the phase difference, $\Delta\Phi^{(3)}$, between the true lift and corrected

unsteady lift approximation. The phase difference $\Delta\Phi^{(1)}$, $\Delta\Phi^{(3)}$ are a measure of the

accuracy of the various unsteady approximation in correctly predicting the proper phase

of the lift forces. We will further quantify these phase difference over a wide range of

flow parameters, but first discuss the behavior of the rms lift amplitude. As in chapter 2,

we use root mean square error for the comparison of the lift force amplitude.

Fig. 3.11 presents the variation of phase difference ($\Delta\Phi^{(1)}$, $\Delta\Phi^{(3)}$) for the quasi-

steady and corrected unsteady approximations for a range of reduced frequency and

amplitude of plate motion. In Fig 3.11a, the reduced frequency is fixed at k=0.3 and

h_a /c varied for h_a /c<0.15. The phase difference for the quasi-steady approximation are

in the order of 40^0, while the corrected unsteady approximation reduces these difference

to approximation 15^0, an improvement of approximate 60%. The phase difference

($\Delta\Phi^{(1)}$, $\Delta\Phi^{(3)}$) are found to be independent of the h_a/c amplitude level. Fig 3.11b

presents the variation in $\Delta\Phi^{(1)}$, $\Delta\Phi^{(3)}$ when reduced frequency k is varied at a fixed h_a

/c=0.1, the phase difference $\Delta\Phi^{(3)}$ is reduced from the quasi-steady value $\Delta\Phi^{(1)}$ over the

entire range of k. While the unsteady corrected method improves the phase prediction

significantly, value of $\Delta\Phi^{(3)}$ remains as high as $\Delta\Phi^{(3)} \approx 15^0$ at larger k values. At low k

values, phase differences $\Delta\Phi^{(3)} < 5^0$ are obtainable. The phase difference increases with

increase in reduced frequency k.

Fig 3.12 presents the variation of root mean square (rms) errors of the lift force (defined in chapter 2) for the quasi-steady and corrected unsteady methods over a range of flow parameters. Here, the analytical lift L is replaced by the true lift from surface stress integration. Fig 3.12a shows the rms error variation with plate oscillation amplitude h_a /c at a fixed reduced frequency of k=0.2. Fig 3.12b shows the rms error variation with plate oscillation reduced frequency k at a fixed h_a /c=0.1. Results show that rms error increase with both the plate oscillating amplitude and reduced frequency. The rms error for the the unsteady corrected method is much smaller than that from the quasi-steady approximation for all h_a /c and k values. Larger amplitude and reduced frequency leads to the worst case, at k=0.4 and h_a /c=0.1. The rms error from the quasi-steady approximation is approximate 31%; from our corrected unsteady method, it's reduced to 12%. The corrected unsteady method can improve the rms error by almost 60%. In additional, we also run the case of higher Reynolds number (Re=200) flow around the oscillating plate (at k=0.4 and h_a /c=0.1) to study the Re effects on results, within limitations of present numerical simulations (not including turbulent model and 3D effects). The results show that the rms error at Re=200 is approximately 8%, smaller than that for Re=100. This shows that our unsteady correction method can predict rms lift amplitude within 10% even at the highly viscous Re=200, and confirms our idea that Re=100 is a worst case of scenario and the unsteady correction method should yield better results at higher Reynolds number.

Before turning to other issues, we point out that the circulation distributions $\gamma(x,t)$ and $\Gamma(x,t)$ introduced in chapter 2 are attainable from our numerical simulations.

Fig. 3.13 shows typical distributions for k=0.2, h_a/c=0.1, Re=100, α=6^0 at one instant. In Fig. 3.13a, a higher vorticity region is observed near leading edge. It must be remembered that the $\gamma(x,t)$ distribution in the viscous flow summarizes effects from both upper and lower surface boundary layers. Near the trailing edge, the $\gamma(x,t)$ distribution becomes negative suggests that lower surface boundary layer with negative vorticity dominates. In a potential flow, $\gamma(x,t)$=0 at trailing edge due to the Kutta condition. In Fig. 3.13a, $\gamma(x,t)$=0 has shifted away from the trailing edge. These observations lead to consideration of the unsteady Kutta condition in these flows. In an unsteady flow, the location of stagnation point may oscillate and move away from the trailing edge. Our assumption of low frequency and low amplitude should imply that this movement is small in an inviscid flow. However, our simulations are highly viscous with thick boundary layers making interpretation in terms of the Kutta condition difficult. This needs further study. In Fig. 3.13b, the parameter $\Gamma(x,t)$ is presented. We perform another path sensitivity study to determine how $\Gamma(x,t)$ results are affected. Path 1 is the optimum path from Fig. 3.7. While in path 2, $\gamma(x,t)$ values from leading to trailing edges (-*0.5<x/c<0.5*) are integrated. Again, a sensitivity to path geometry is observed. This could have implications for PIV studies which could possibly measure $\Gamma(x,t)$. The enclosed integration region in these studies would have to be carefully selected.

3.6.1 Correction of experimental data from pitching plate study

In this section, we study application of our corrected unsteady method to correct previous UCMT data from experiments on a pitching airfoil (Weber et al, 1995). Our

intent here is to study how much the properly converted lift values will deviate from lift values determined using the quasi-steady approximation, as was done in Weber et al (1995). We point out that Weber used a single acoustic leg downstream of the airfoil (see Fig.1, Weber et al, 1995) and not a closed acoustic path. Also, circulation data was often obtained for only one-half of an oscillation cycle. Given those facts, we will accept the measured circulation values as valid, and apply our unsteady correction methods.

Reduced frequency k is one of the primary parameters studied in Weber et al (1995) for the pitching airfoil. Fig 3.14 represents a low reduced frequency case (k=0.059) in Weber's work. In Fig 3.14a, measured Γ and lift coefficient values from Weber et al (1995) are presented for a pitching NACA 4418 airfoil with motion $\alpha = \alpha_0 + \alpha_a \sin \omega t = 7^0 + 11^0 \sin 10t$. The $\alpha = f(t)$ curve shows that the experimental data was only acquired in one half of a sinusoidal oscillation cycle. Prior to reaching the maximum angle of attack, the circulation and lift curves have a similar sinusoidal shape, but after the maximum point, they drastically deviate from the sinusoidal behavior. The lift and circulation values lead the angle of attack curve by a fairly large phase angle. In Fig 3.14b, the time derivative of circulation $d\Gamma/dt$ and the unsteady correction factor R (from Eq.(A.19)) for this data are presented. The value of R is generally small in the area of the maximum angle of attack. Physically, when the pitching airfoil approaches α_{max}, its motion gradually becomes slowdown and stop, the contribution from the quasi-steady term A in Eq. (2.3) to the total lift become larger, and correspondingly leads to the effect of the unsteady term B smaller. In Fig 3.14c, the R and $d\Gamma/dt$ results from Fig

3.15(b) are applied through Eq. (2.36) yielding the corrected lift coefficients which we compare to the original Weber et al (1995) data. Large correction in lift coefficient is on the order of 0.3 in C_l (about 25% error) occurred at low AOA. However, due to the small values of $d\Gamma/dt$ for high AOA, only small corrections in peak lift coefficient values are found.

In Fig 3.15 and Fig. 3.16, Similar results for intermediate and high reduced frequencies from Weber's data are presented. The qualitative trends for these results are similar to those in Fig. 3.14. The difference between corrected lift and original data increases with increase of amplitude and reduced frequencies. Further of application of our unsteady correction methods to experimental data is limited by the lack of UCMT data at present in unsteady flows. Future anticipated studies to address this lack of data will be discussed in chapter 6.

3.7 Summary

The results in this chapter show that quasi-steady approximation based on K-J theorem used by previous investigators in UCMT and oscillating airfoil studies has limitations for predicting the unsteady lift force due to the lack of consideration of unsteady effects. Our corrected unsteady method can improve predictions of the phase, rms lift in oscillating plate flows at low Re number, compared to the quasi-steady method. Our work in this chapter further verified the methods developed in previous chapter to properly convert the time dependent bound circulation, which is measurable with the UCMT technique, to unsteady lift force. We have also shown that specification

of the size and location of the closed acoustic path are crucial to bound circulation determination, and hence will definitely affect the instantaneous lift force measurement. The knowledge studied here will provide guidance for experimental design when using the UCMT technique. This path sensitivity also has implications for PIV and LDV studies that perform integrations within a specified closed path. As an extension of current developed approximation for the oscillating plate flow, we suggest a general relation between the time-dependent bound circulation measurable with the UCMT technique and the time-dependent lift force that may have applications to other unsteady flows, through this relation

$$L(t) = \rho U \Gamma(t) + R\rho l \frac{d\Gamma(t)}{dt} \ . \tag{3.13}$$

and l is the characteristic length of the body. R will be vary with body shape and motion, and may not be a concise analytical result as in our studied flow where $R = \frac{3}{4}$.

For example, in the study of the pitching airfoil in chapter 2, R is a complicated function of time, oscillating amplitude, reduced frequency, angle of attack and pivot location. But in certain cases, R could be determined and used to develop further unsteady approximations. For example, in chapter 4, we will study the application of Eq. (3.13) to a classic unsteady flow over a stationary cylinder at low Reynolds number.

To this point, we have fulfilled several major goals of the present work including developing a method to properly convert the time dependent bound circulation, which is measurable with UCMT or PIV techniques, to instantaneous lift force. We also better understand the importance of closed acoustic path selection on

bound circulation determination. Hence, our work has expanded the capability of UCMT for unsteady flow studies.

Reader may noticed that in our path sensitivity studies, we only considered it at a fixed $\alpha=6^0$ and Re=100. We believe the path sensitivity will also be affected by other parameters such as Reynolds number, angle of attack, turbulence intensity, and systematically investigations about these issues will be an interesting topic in future.
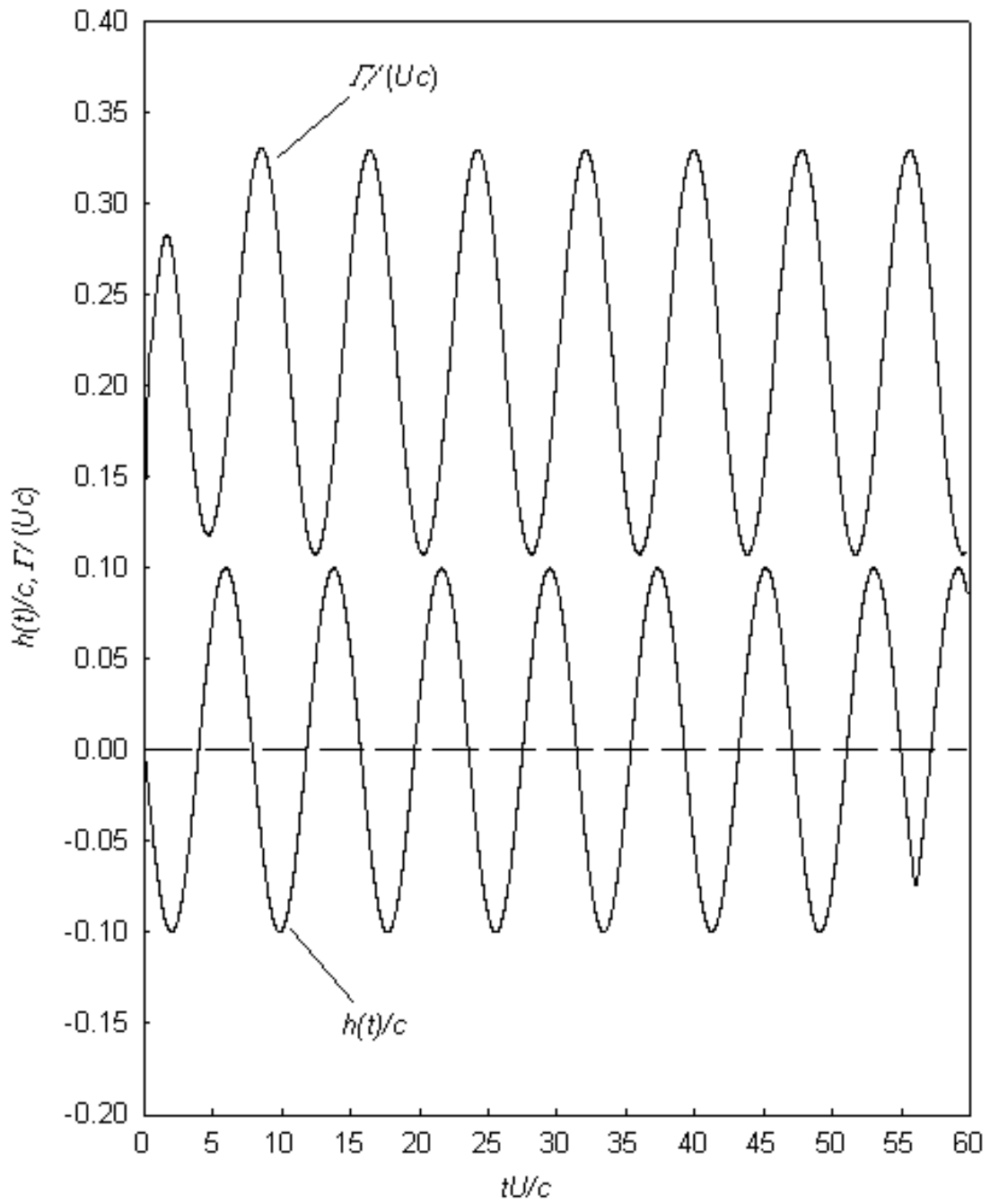
Fig 3.9 A typical case of plate instantaneous location and bound circulation variation with time, *k=0.4*, *h_a/c = 0.1.*
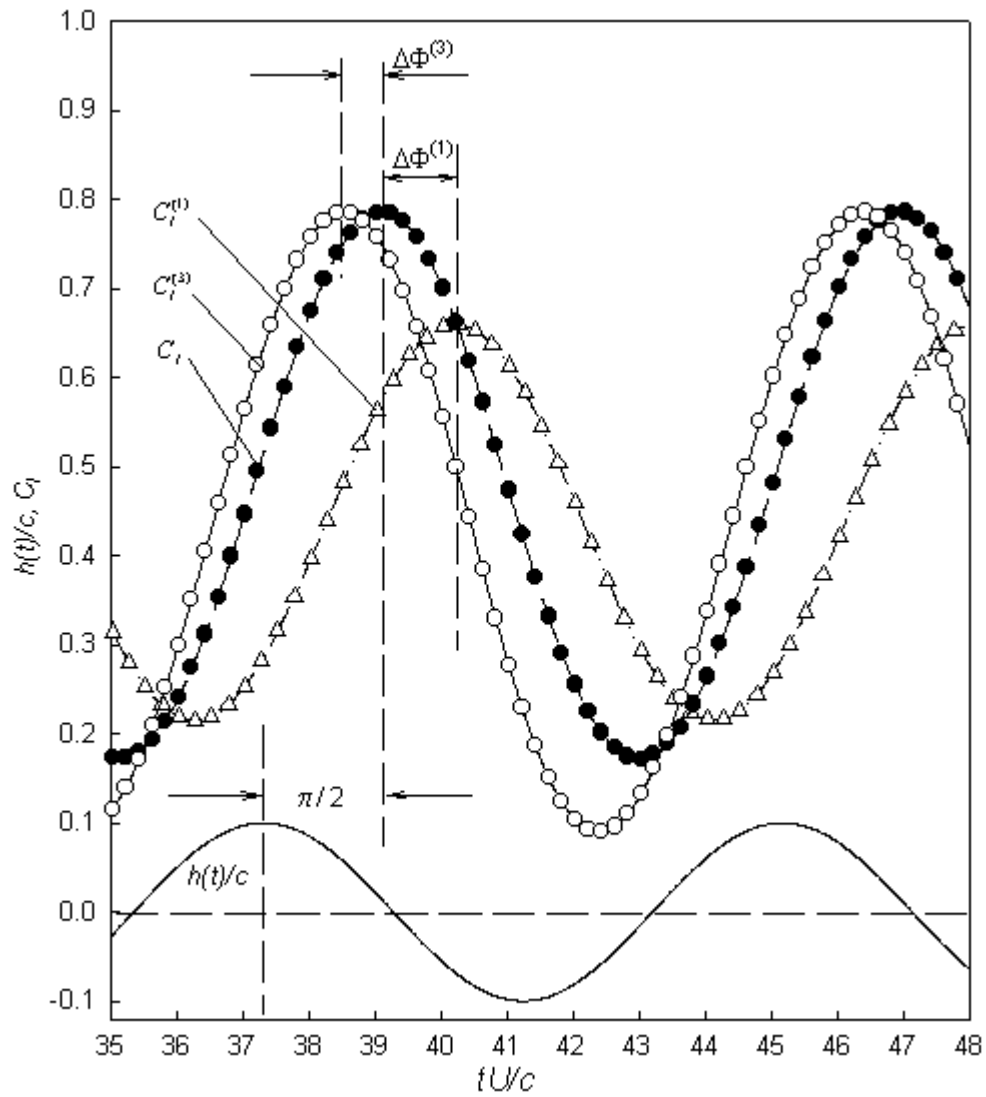
Fig. 3.10 Typical lift force obtained from different methods at k=0.4, h_a /c=0.1
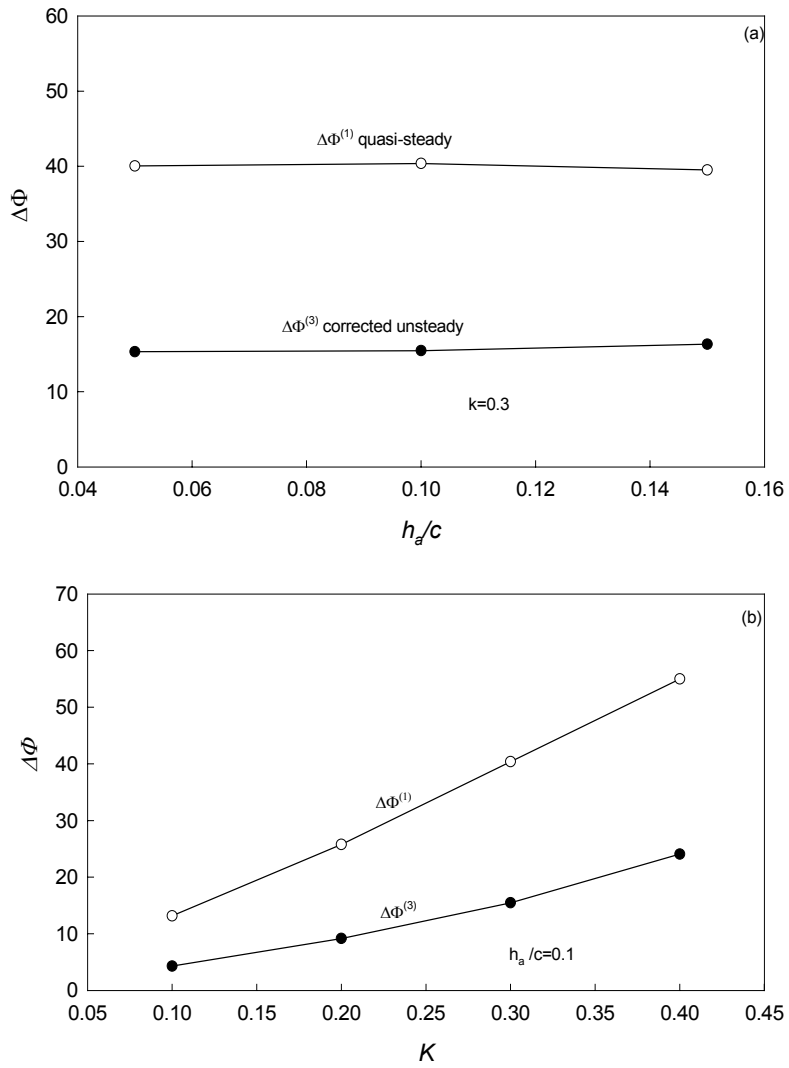
Fig 3.11 Phase difference variation with plate oscillating amplitude and reduced frequency at Re=100

$$e_{rms}^{(3)} = \frac{L_{rms}^{(3)} - L_{rms}}{L_{rms}}$$

$k=0.2, \ \alpha=6^0$

$e_{rms}^{(1)}$

$e_{rms}^{(3)}$

(a)

e_{rms}

h_a/c

$h_a/c=0.1, \ \alpha=6^0$

$e_{rms}^{(1)}$

$e_{rms}^{(3)}$

Re=100

Re=100

$e_{rms}^{(3)}$
Re=200

(b)

e_{rms}

k
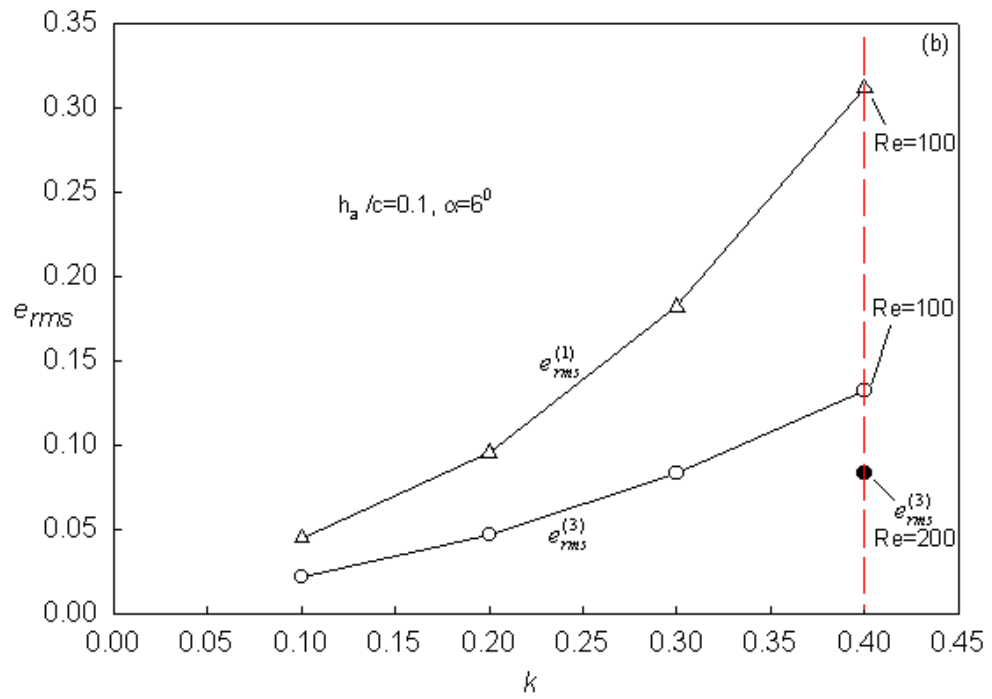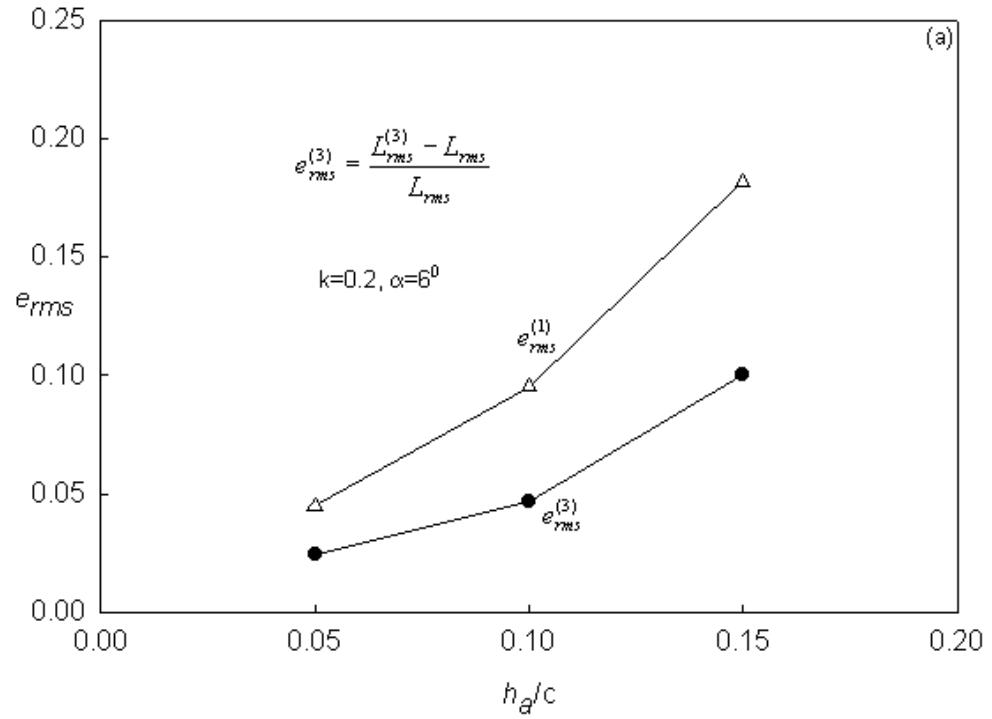
Fig 3.12 Rms error variation with plate oscillating amplitude and reduced frequency

94
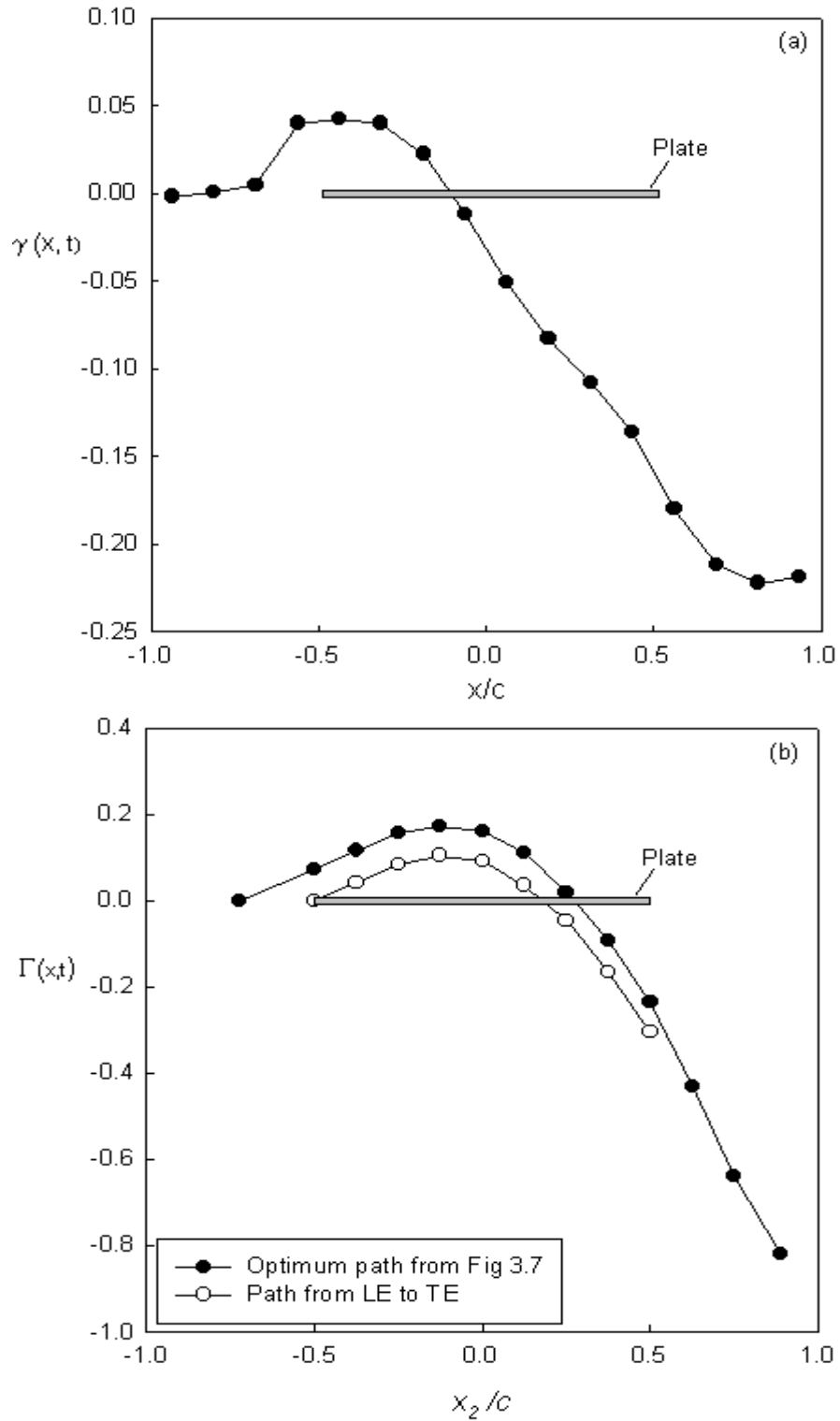
Fig 3.13 Typical numerically attainable circulation distributions along plate at an instant. Re=100, $\alpha=6^0$, k=0.2, h_a /c=0.1. (a) local chordwise vortex element strength distribution. (b) Integrated vorticity distributions from the optimum path and a path just from leading edge (LE) to trailing edge (TE).
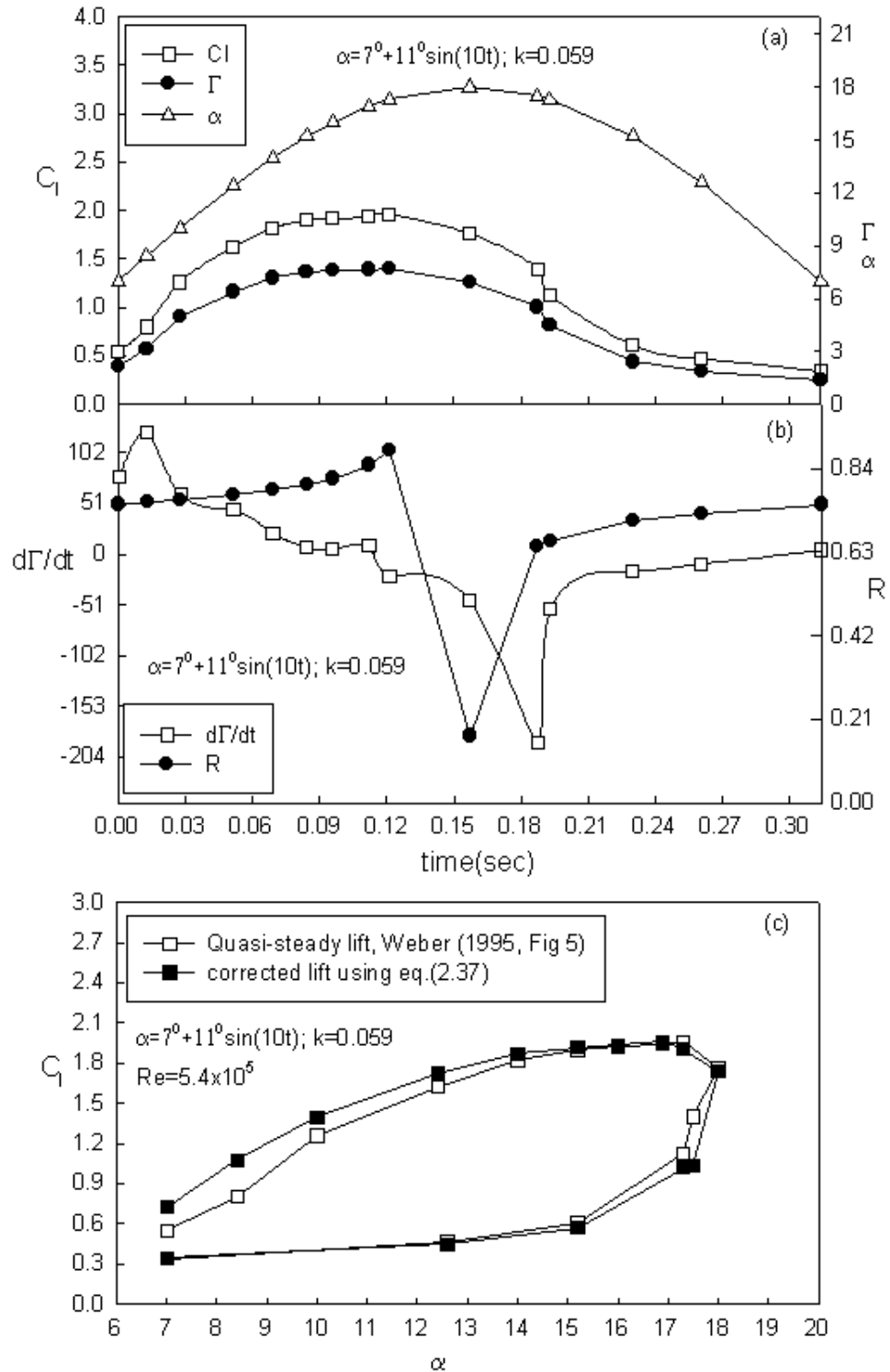
Fig.3.14 Application of corrected unsteady methods to Weber et al (1995) measurements on a pitching NACA 4418 airfoil. $\alpha = 7^0 + 11^0 \sin(10t)$, k=0.059, Re=5.4×10⁵. (a) Lift coefficient and correlation measurements of Weber et al (1995). (b) Behavior of first derivative and unsteady correction factor R (from Eq. (A.19)). (c) Corrected lift coefficients compared to Weber et al (1995) original results.
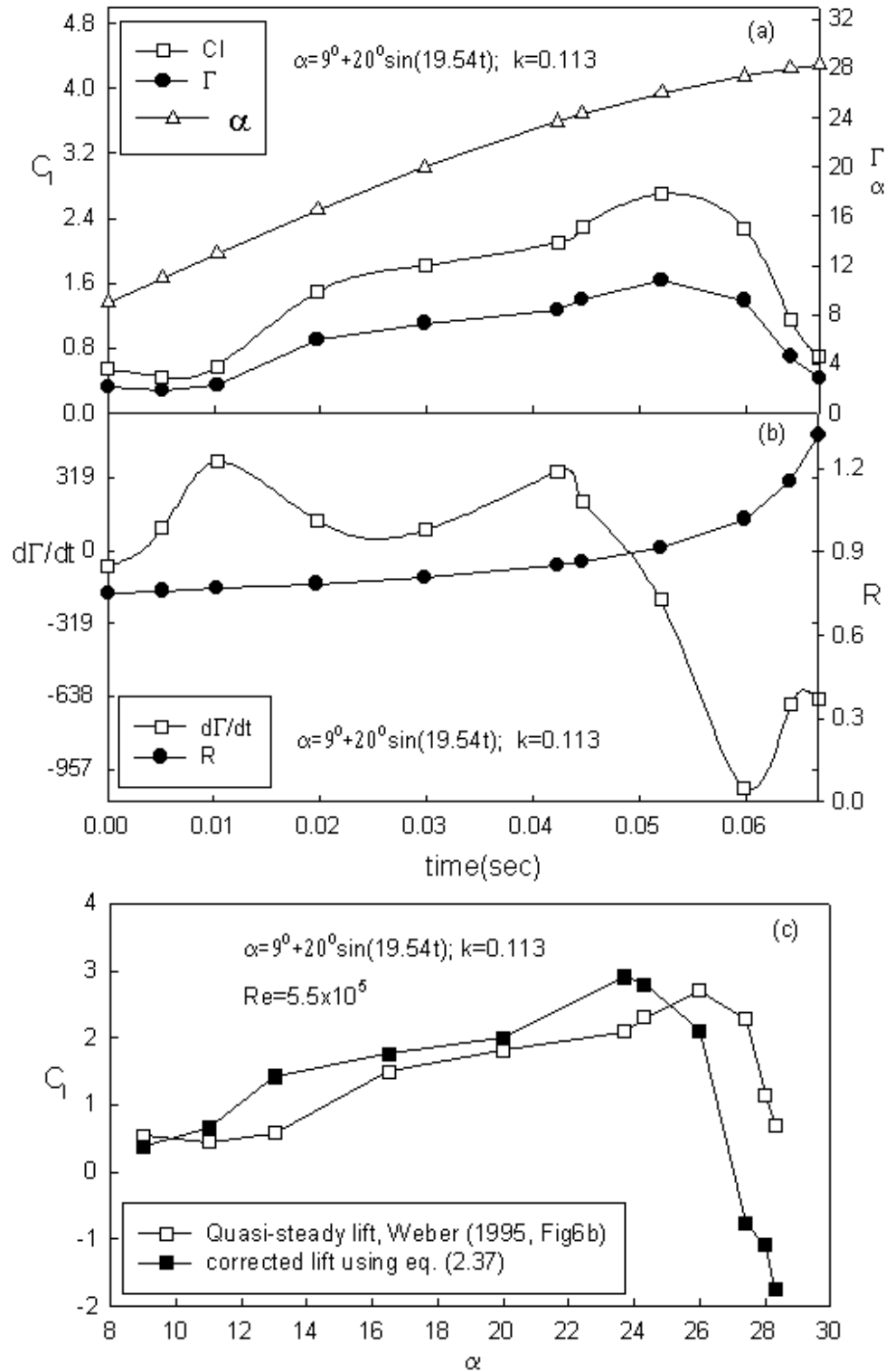
Fig 3.15 Application of corrected unsteady methods to Weber et al (1995) measurements on a pitching NACA 4418 airfoil. $\alpha = 9^0 + 20^0 \sin(19.54t)$, k=0.113, Re=5.5×10^5. (a) Lift coefficient and correlation measurements of Weber et al (1995). (b) Behavior of first derivative and unsteady correction factor R (from Eq. (A.19)). (c) Corrected lift coefficients compared to Weber et al (1995) original results.
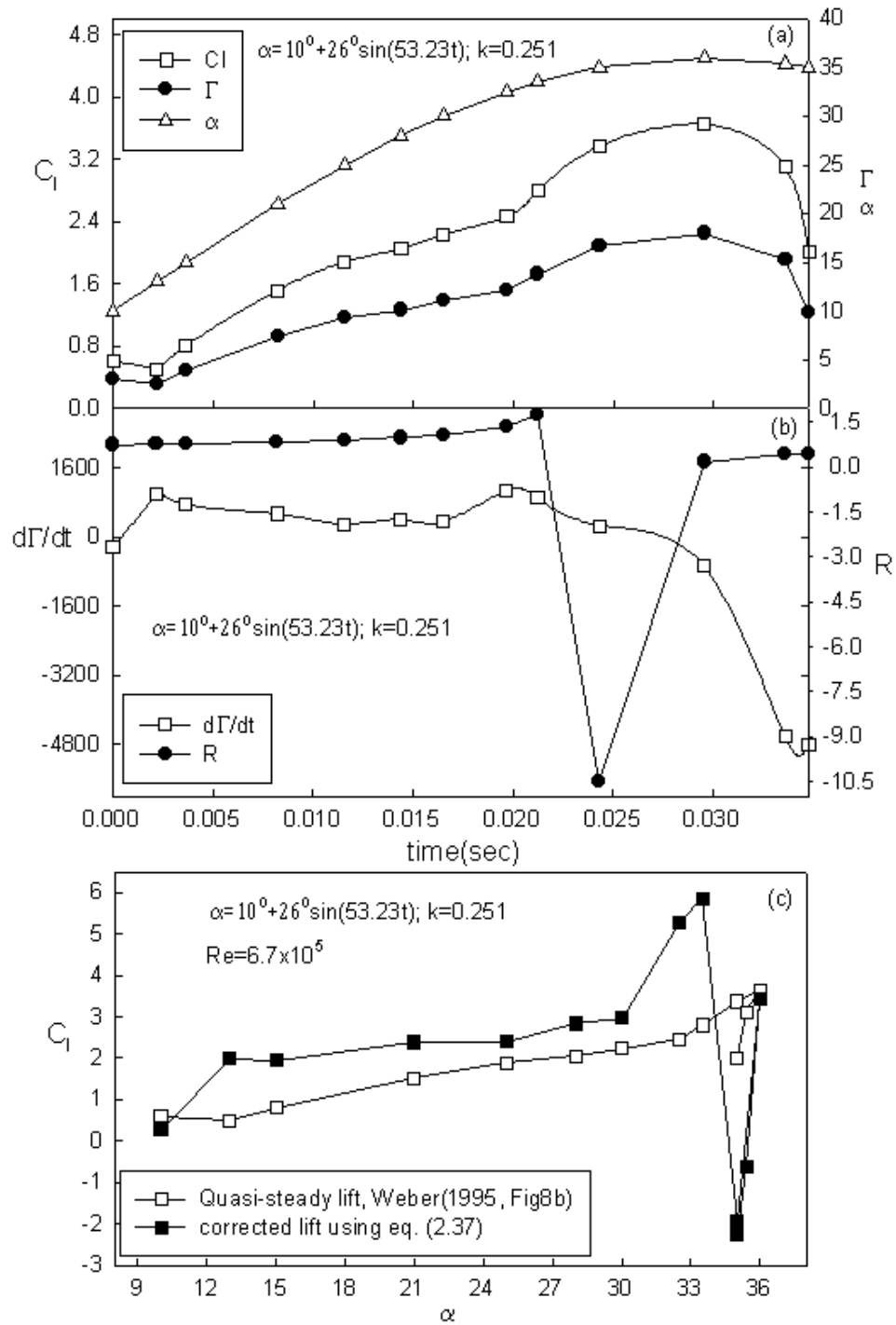
Fig.3.16 Application of corrected unsteady methods to Weber et al (1995) measurements on a pitching NACA 4418 airfoil. $\alpha = 10^0 + 26^0 \sin(53.23t)$, k=0.251, Re=6.7×10^5 . (a) Lift coefficient and correlation measurements of Weber et al (1995). (b) Behavior of first derivative and unsteady correction factor R (from Eq. (A.19)). (c) Corrected lift coefficients compared to Weber et al (1995) original results.

Chapter 4

Circulation Methods for Instantaneous Lift Force Determination – Circular Cylinder Flow

4.1 Introduction

In chapter 2 and 3, we have achieved a better understanding of lift determination in unsteady thin airfoil flows through analytical and numerical studies. As long as the bound circulation is varying with time, unsteady effects have to be included for accurate instantaneous lift force determination. In our developed method, the instantaneous lift force is composed of the quasi-steady lift expressed in same form as Kutta-Joukowski (K-J) theorem, and an unsteady term involving the time-derivative of bound circulation, adjusted with a defined unsteady lift correction coefficient R (for the oscillating thin airfoil, $R=0.75$). Another important issue we have identified is that the size and the role that ultrasonic sound path is critical in determination of time-dependent bound circulation in the UCMT method. This systematic study will be helpful in design of sound paths in UCMT experiments. In chapter 4 we study whether the framework developed in previous chapters can be extended to a classical unsteady flow, low Re vortex shedding from a stationary bluff body. We again take a similar approach as in chapter 3 where numerical simulation are preferred and studied over future anticipated experimental UCMT studies. Before describing our work in this chapter, we will first present a literature review of past investigations on instantaneous lift measurement in vortex shedding studies.

The fundamental question addressed in this chapter and by previous investigations is the proper method for converting flow field data (velocity, vorticity or

circulation field) to determine resultant fluid forces on the bluff body. This issue is important in PIV and LDV in addition to UCMT studies.

Compared to the in-line (drag) force well represented by Morison equation in certain flow situation, the lift force is more difficult to analyze because it is more sensitive to how vortices are formed, shed and move in bluff body wake. Several researchers have suggested that if detailed information about vortex strength and motion are available, then a Blasius equation could be a good choice to calculate the fluid forces. Using this equation, Maul & Milliner (1978) have qualitatively studied the relationship between development of the fluid force and the generation and movement of shed vortices in the wake. Ikeda & Yamamoto (1981) used similar ideas for a rough prediction of lift force by estimating the rough motion and strength of vortices in the wake from particle streak visualization photographs.

With a desire to acquire quantitative information and have a better understanding of the role of vortices in fluid loading, Obasaju & Bearman (1988) experimentally studied the sectional and total lift force acting on an oscillating circular cylinder in a water tunnel. For bound circulation determination, the velocity measurement around the cylinder at its center span were made by using a thermo system Laser Doppler velocimetry (LDV) working in forward scatter mode with a frequency tracker, Measurements were made within a square circuit enclosing the cylinder (Fig 4.1a). The measured bound circulation was converted to instantaneous lift forces based on the K-J theorem. Simultaneously, the pressure average technique (summarized in chapter 1) was used to obtain the instantaneous lift force for the purpose of comparison.
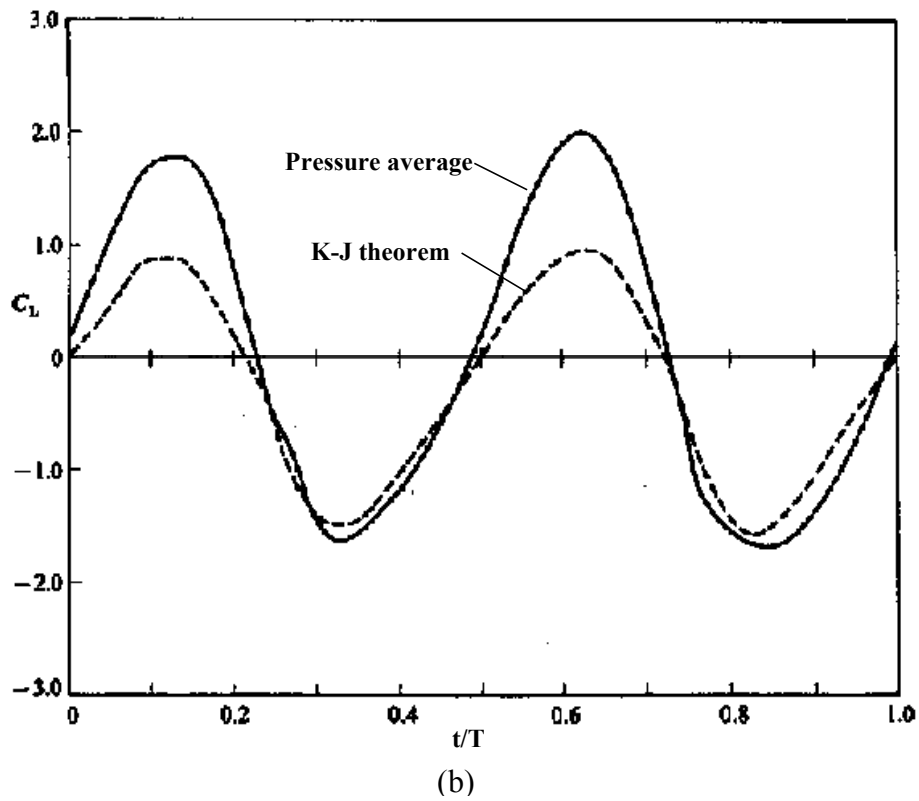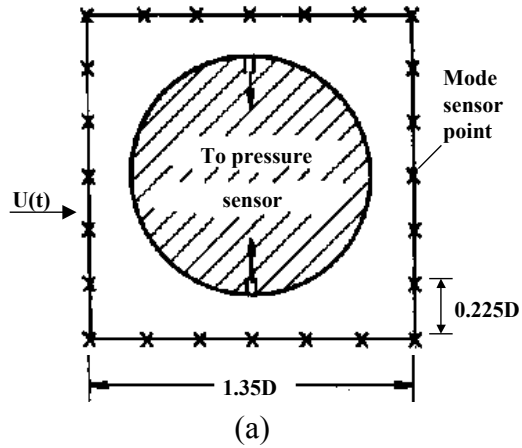
Fig 4.1 Lift force measurement on an oscillating cylinder. (a) Schematic of a square path enclosing cylinder (Fig. 1 in Obasaju & Bearman (1988)). (b) Comparison of lift force from Kutta-Jukowski theorem and that from pressure average method at *KC=6.75* (Fig. 20(a) in Obasaju & Bearman (1988)).
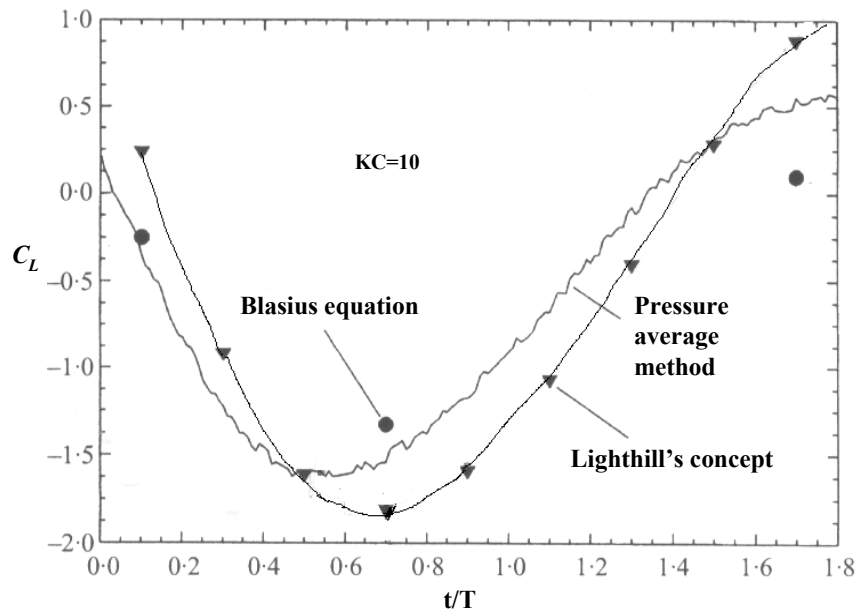
Fig 4.2 Instantaneous lift force at *KC=10* obtained from three methods by Lin & Rockwell (1996). Difference in lift amplitude and phase exist between different methods (Fig. 2 in Lin & Rockwell (1996)).

A typical result from this work is shown in Fig 4.1(b). The agreement between the lift obtained from the K-J theorem and that from the pressure average method is not good, but the gross features of the curves, such as the positions of the peaks were still well predicted. Hence, they suggested that K-J theorem could be considered as a good first approximation to determine the unsteady lift on a bluff body, and the authors thought it was a remarkable finding and could not be explained and may be fortuitous.

Lin & Rockwell (1996) studied the instantaneous lift force on an oscillating circular cylinder using the PIV technique. After obtaining the vorticity distribution in a region at successive instants, they used theoretical concepts such as the Blasius equation and Lighthill's concepts to provide an experiment determination of the instantaneous lift (Fig 4.2). These methods were compared to lift forces obtained using the pressure average method. Larger difference exists between the instantaneous lift curves obtained using the different methods. They also mentioned that their future efforts would focus on studies when varying the size and location of the enclosing region where the sensitivity of the lift calculation is determined. The goal would be to enhance the accuracy of their methods through a systematic study similar to these we have conducted in the presented work.

These show that work still needs to be done to gain a better fundamental understanding of the proper method for converting flow field measurements into instantaneous lift curves in wake studies. In this chapter, we seek to extend our previously developed framework to address issue. We study the low Reynolds number vortex shedding from a stationary bluff body (circular cylinder) using similar numerical

techniques as in chapter 3. We focus on whether instantaneous bound circulation values (of the type attainable from UCMT experiments) can be properly converted to instantaneous lift values in this flow. Motivated by earlier work of Wu (1981) and the cited previous investigations, we study various force models including a quasi-steady Kutta-Jukowski method, a vortex flow force model (Lighthill, 1986), and a new unsteady correction model similar to that developed for the thin airfoil flow in chapters 2 and 3. Finite element simulations for flow over a circular cylinder at Re = 100 are once again performed in order to obtain true instantaneous lift values (from surface stress integration), which are then compared to various combinations of the force models. It is determined that stream-wise circulation distributions in the wake behind the circular cylinder are required to properly apply the vortex flow force model by Lighthill (1986). These distributions would be attainable in experimental UCMT studies. Again, the important issue of the proper size and location of the closed path for bound circulation determination will be studied.

In section 4.2, we describe additional issues related to the numerical methods of chapter 3 that are now relevant to our circular cylinder flow investigation. We then study the streamwise circulation distributions in the wake behind the circular cylinder. These circulation distributions are required to properly determine the vortex force based on Lighthill's model in section 4.3. In section 4.4, the effect of size and location of the mimic closed ultrasound path on bound circulation determination is investigated. Finally, lift forces results determined from different fluid force models will be discussed in section 4.5. We will show that proper superposition of the three previously listed

104

models (K-J quasi-steady, vortex force, and unsteady correction term) can accurately predict instantaneous lift values on circular cylinders.

4.2 Numerical Method

The numerical code used here is largely the same as that used in chapter 3, which is based on the classical Garlekin finite element method to solve the Navier-Stokes equations. Difference includes changing the coordinates of the no-slip boundaries according to the geometry of the body (circular cylinder here), and numerical grid. Parameters are all non-dimensionalized with free stream speed U, and cylinder diameter d, for example, velocity is normalized as $\vec{V^*} = \vec{V}/U$, time as $t^* = tU/d$. The origin of the xy coordinate system is set at center of the circular cylinder. The numerical grid is generated through PATRAN in a computational domain extending 8 diameters in the y (transverse) direction ($-4 < y/d < 4$) and 24 diameters in x direction ($-4 < x/d < 20$). The mesh in vicinity of cylinder is much finer so that the detailed near wake flow information can be captured. The total number of nine-node quadratic elements is $NM=984$, number of nodes is $NND=4068$. The input Reynolds number is $Re=100$, and time step $\Delta t=1/40$.

The boundary conditions of the computational domain are set as follows; at inlet, upper and lower grid boundaries, the velocity is set as the free-stream velocity. At the surface of the circular cylinder, no-slip condition is maintained. At the outlet boundary, a synthetic (constant pressure) condition is utilized as in chapter 3.

The solution of the problem was conducted using a segregated procedure for the

primary unknowns at each node. The algorithm of interpolation with bi-quadratic polynomials was used for solutions of velocity components and pressure at any arbitrary spatial location. By using the potential flow solution of pressure field as initial guess to accelerate the convergence process, the conservation equations were solved at each time step using an explicit step for an intermediate velocity field. The numerical scheme has been used previously by Olinger et al (1995) to model flow over an oscillating cylinder wake at low Reynolds number. In the present work, stationary cylinder wakes are studied.

A typical result from the numerical simulation is shown in Fig 4.3 for a low Reynolds number Re=100 flow. Fig 4.3(a) shows the flow field in vicinity of circular cylinder at *tU/d=78.875*, which shows clearly the velocity vector field, vortex generation and shedding process. Fig 4.3(b) is a typical time trace of the lift force acting on the circular cylinder, obtained from surface stress integration method at each time instants. The periodical lift force is due to the periodic vortex shedding process in the wake of cylinder shown in Fig 4.4. The numerical code can provide accurate velocity data to be used for circulation determination along an arbitrary selected closed path.

4.3 Wake circulation distribution and vortex lift force

In this section, we study how circulation measurements (obtainable with a UCMT method) can be used to determine the 'vortex force' developed by Lighthill (1986). The fluid forces in that model are related to wake vortex strength and locations. Lighthill proposed the following expression.

$$\vec{F}_v = -\frac{d}{dt}\left[\frac{1}{2}\rho\int \vec{r}\times\vec{\omega}d\forall\right] \quad . \tag{4.1}$$

where $\vec{r}$ is the position vector (relative to the origin) of a fluid element in wake flow with vorticity $\vec{\omega}$. In a two-dimensional flow, $\vec{r} = x\vec{i} + y\vec{j}$, $\vec{\omega} = \omega\vec{k}$, $d\forall = dA\times1$. The cylinder wake is divided into N_x sections in x direction and N_y sections in y direction (Fig 4.5a). The circulation of a fluid element at location (x_i,y_j) is given by

$$\Gamma_{ij} = \oint \vec{V}\cdot d\vec{l} = \iint_{A_{ij}} \vec{\omega}\cdot d\vec{A} \quad . \tag{4.2}$$

within the infinitesimal area A_{ij}, vorticity can be assumed as constant, hence

$$\Gamma_{ij} \approx \omega_{ij}A_{ij} \quad . \tag{4.3}$$

$$\omega_{ij} \approx \frac{\Gamma_{ij}}{A_{ij}}, \quad \vec{\omega}_{ij} \approx \omega_{ij}\vec{k} \quad . \tag{4.4}$$

Discretizing equation (4.1) and substituting equation (4.4), the vortex force will be

$$\vec{F}_v \approx -\frac{\rho}{2}\frac{d}{dt}\left[\sum_{i=1}^{N_x}\sum_{j=1}^{N_y}(x_{ij}\vec{i} + y_{ij}\vec{j})\times\vec{\omega}_{ij}(A_{ij}\cdot1)\right] \approx -\frac{\rho}{2}\frac{d}{dt}\left[\sum_{i=1}^{N_x}\sum_{j=1}^{N_y}(y_{ij}\vec{i} - x_{ij}\vec{j})\Gamma_{ij}\right]. \tag{4.5}$$

$$\vec{F}_v \approx [-\frac{\rho}{2}\frac{d}{dt}\sum_{i=1}^{N_x}\sum_{j=1}^{N_y}(\Gamma_{ij}y_{ij})]\vec{i} + [\frac{\rho}{2}\frac{d}{dt}\sum_{i=1}^{N_x}\sum_{j=1}^{N_y}(\Gamma_{ij}x_{ij})]\vec{j} \quad . \tag{4.6}$$

Hence, the vortex lift force will be

$$L_v \approx \frac{\rho}{2}\frac{d}{dt}\sum_{i=1}^{N_x}\sum_{j=1}^{N_y}(\Gamma_{ij}x_{ij}) \quad . \tag{4.7}$$

The corresponding lift coefficient will be

(a)

(b)
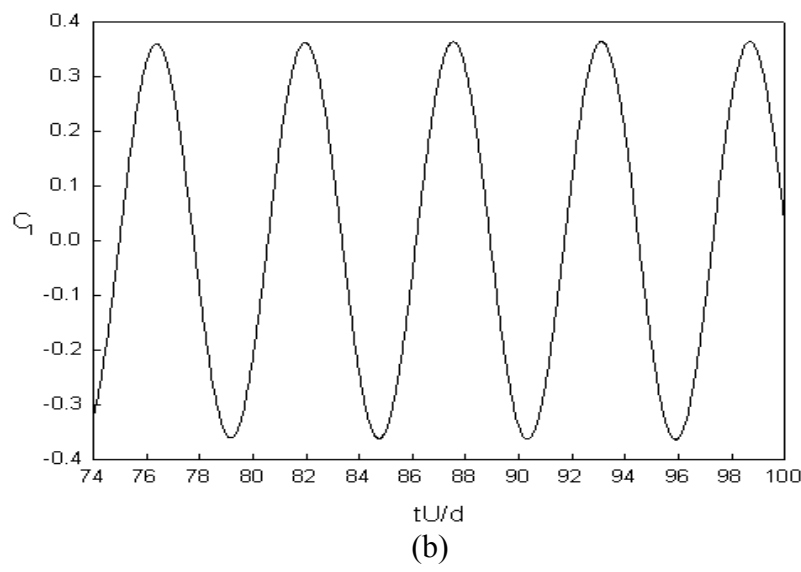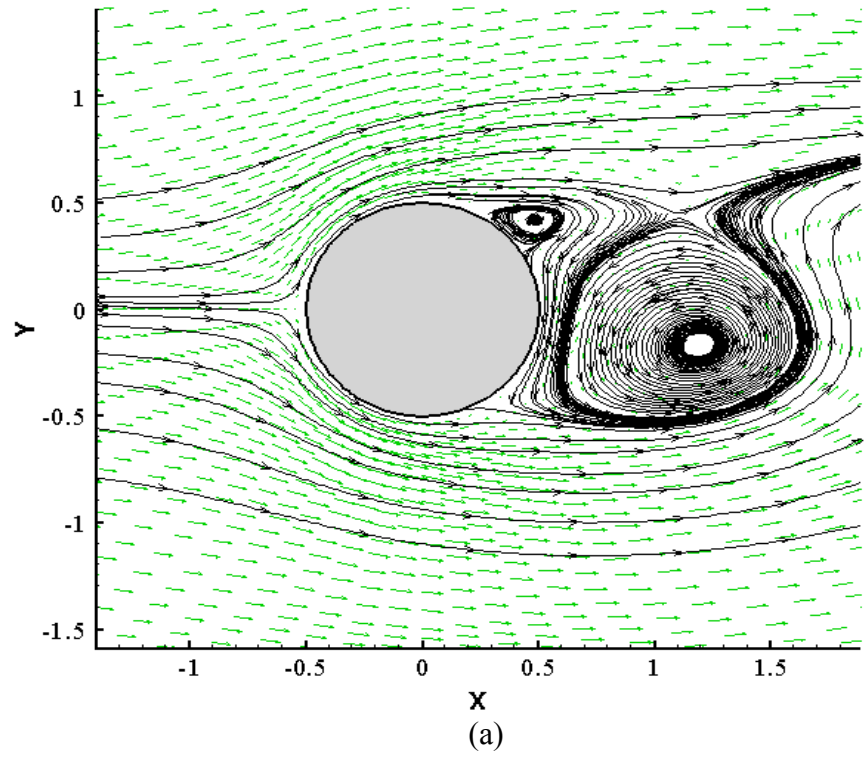
Fig 4.3 Typical results from numerical simulation of flow over a stationary circular cylinder at *Re=100*. (a) Velocity vector field and streamlines at one time instant presented the vortex generation and shedding process. (b) The time trace of lift force was from the stress integration method.
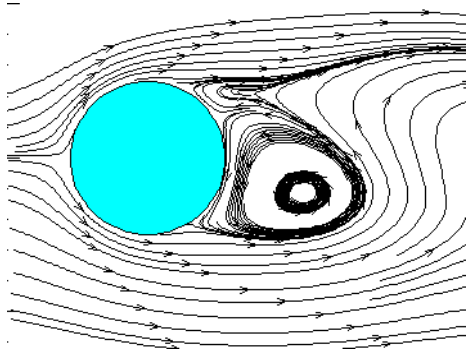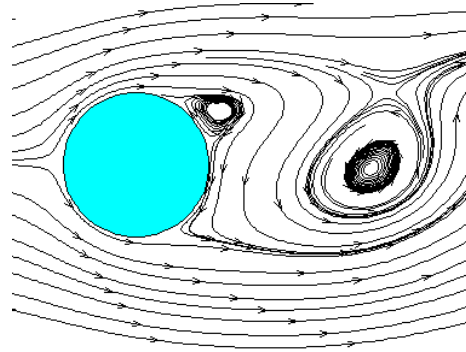
(a) *tU/d=76.4*   (b) *tU/d=77.8*
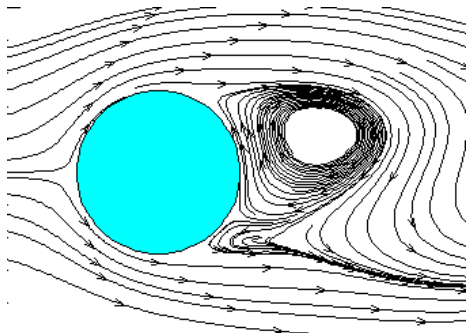
(c) *tU/d=79.2*
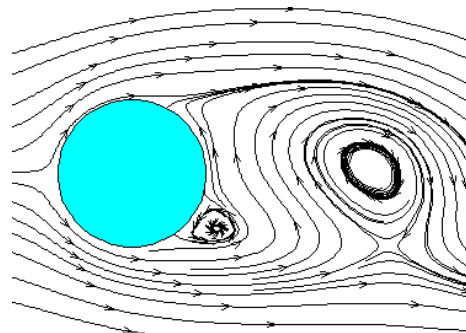
(d) *tU/d=80.58*
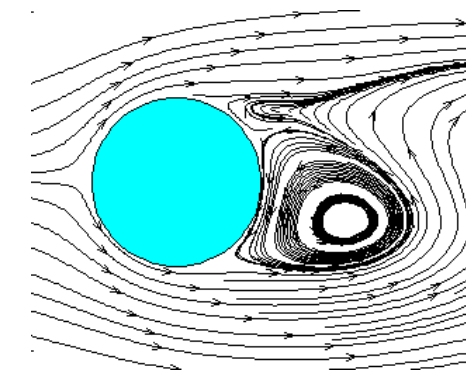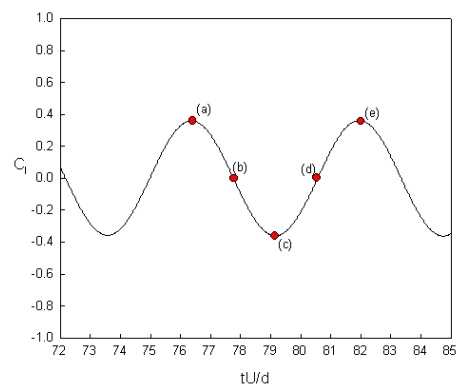
(e) *tU/d=81.98*   (f) C_l time trace

Fig 4.4 Flow visualization of the near wake of circular cylinder during one lift cycle at *Re=100.* (a)-(e) are instantaneous wake vortex structures at five time instants shown in (f), the periodic time trace of the lift force.

(a)

(b)
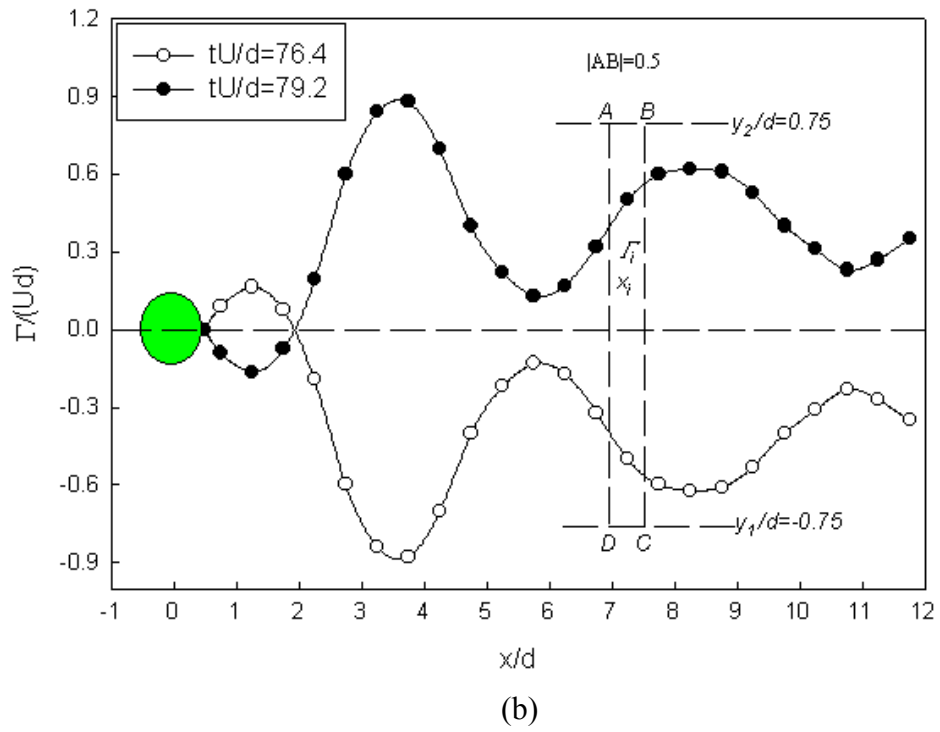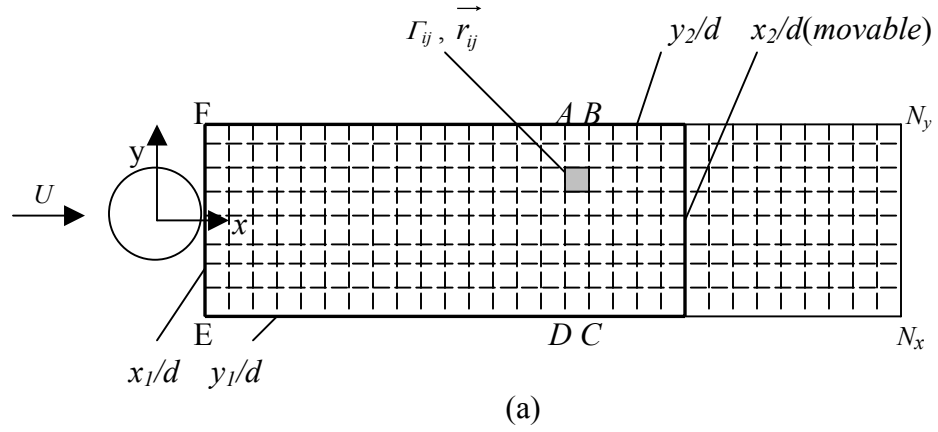
Fig 4.5 (a) Schematic of cylinder near wake and definition of variables needed for wake circulation determination. In *x*-direction, wake is divided into N_x sections. In *y* direction, it is N_y sections.   (b) Wake circulation distribution in x-direction with y_1/d=-0.75, y_2/d=0.75. Wake is divided into a series of consecutive smaller paths like *ABCD*, with the path extent in *x*-direction |AB|=$\Delta(x/d)$=0.5

$$C_{Lv} \approx \frac{\dfrac{d}{dt}\displaystyle\sum_{i=1}^{N_x}\sum_{j=1}^{N_y}(\Gamma_{ij}x_{ij})}{(U^2 d)} \quad . \tag{4.8}$$

Form Eq. (4.8), the vortex lift force only dependent on the *x*-coordinate of the fluid element, hence all the fluid elements enclosed by a path *ABCD* will be with the same *x*-coordinates, and

$$\sum_{j=1}^{N_y}(\Gamma_{ij}x_{ij}) \approx x_{ij}\sum_{j=1}^{N_y}\Gamma_{ij} \quad . \tag{4.9}$$

After defining $\Gamma_i \approx \displaystyle\sum_{j=1}^{N_y}(\Gamma_{ij})$ as the circulation in area enclosed by path *ABCD,*

and replacing x_{ij} with x_i, Eq.(4.8) yields

$$C_l^v \approx \frac{\dfrac{d}{dt}\displaystyle\sum_{i=1}^{N_x}(\Gamma_i x_i)}{(U^2 d)} \quad . \tag{4.10}$$

once Γ_i and x_i are known, lift component of vortex force can be obtained. We note that Eq. (4.10) approximates the true Lighthill vortex force given by Eq. (4.1), it must be recognized when interpreting numerical results.

Equation (4.10) is a useful expression for UCMT studies on circular cylinder wakes. It states that to determine lift component of vortex force in Lighthill's model, one needs only measure Γ_i and x_i in the wake of a circular cylinder. Γ_i can be obtained in a UCMT study by specifying the closed path ABCD (Fig 4.5(a)). It is particularly useful that only the location x_i is needed to find the lift force in Lighthill's model, since

x_i is known once the path ABCD is specified. In the schematic of determination of Γ_{ABCD} in Fig. 4.5(a), we can calculate

$$\Gamma_i = \Gamma_{ABCD} = \Gamma_{EFBC} - \Gamma_{EFAD} \ . \tag{4.11}$$

Measurement of Γ_i could be accomplished by using Eq. (4.11) where moving the downstream leg at $x_2\,/d$ incrementally will aid finding Γ_i. In real UCMT test, the size of acoustic transducers and the length of sound path may affect the resolution of the Γ_i distribution measurement. For PIV technique, however, Eq. (4.1) may yield more accurate results considering that the spatial measurement resolution of PIV is greatly better than UCMT. Following the spirit of chapter 2, we will validate these ideas using our numerical simulation in the previous work.

Using the numerical algorithm described in chapter 3 applied to the circular cylinder flow, we studied circulation variation in both x and y direction in the wake. It was found that the majority of shear layer vorticity is confined to a region between $y_1/d=-0.75$ and $y_2/d=0.75$. Hence, they were selected as upper and lower bound of the path ABCD with the size in x direction set as $\Delta(x/d)=0.5$. Fig 4.5(b) presents typical wake circulation distributions in the x-direction at tU/d=76.4 and 79.2 corresponding to the flow visualizations of Fig 4.4(a) and 4.4(c) respectively. The circulation distributions at the two instants are clearly out of phase reflecting the shedding process in Fig 4.4. The wake circulation distribution shows a periodic variation with streamwise distance reflecting sequentially shed vortices in the wake. Peaks in the circulation distribution reach a maximum near x/d=3.5 and then decay due to viscous dissipation as

the vortices move downstream. These distributions provide all the necessary Γ_i and x_i information for vortex lift force determination using equation (4.10) at any time instant, typical time traces of the wake vortex lift are shown in Fig 4.6.

Recognizing that the extent of the wake over which Eq. (4.10) is applied could affect resultant vortex lift force values, we fix the region EFBC in Fig 4.5(a) as follows, the legs EC and FB are set at $y_1/d=-0.75$ and $y_2/d=0.75$ respectively. The leg EF is fixed just behind cylinder at $x_1/d=0.5$, and the downstream leg BC is variable with x_2/d adjusting, Eq. (4.11) is then used to find Γ_i. Fig.4.6 presents four curves of wake vortex lifts from four different EFBC regions with $x_2/d=5, 10, 15$ and 20. Obviously there exist phase and amplitude difference between these curves. With an increase in size of EFBC domain, the amplitude of wake vortex lift gradually increases and the phase gradually decrease (earlier in time), due to inclusion of additional vortex elements in the far wake that were shed earlier. However, the difference between results for $x_2/d=15$ and $x_2/d=20$ is much smaller than that between $x_2/d=5$ and $x_2/d=10$. This is because the fluid dissipation effect and the contribution to lift from vortices further away from the cylinder decrease. For region EFBC with $x_2/d=20$, we encompass the downstream bound of our computational domain for the cylinder flow. Based on Fig.4.6, we conclude that use of region EFBC with $x_2/d=20$ will yield accurate wake vortex lift forces and that contribution of vortices downstream of our numerical boundary can be neglected. Hence, all of the wake vortex lift force results presented later will be obtained from region EFBC with $y_1/d=-0.75$, $y_2/d=0.75$, $x_1/d=5$ and $x_2/d=20$.
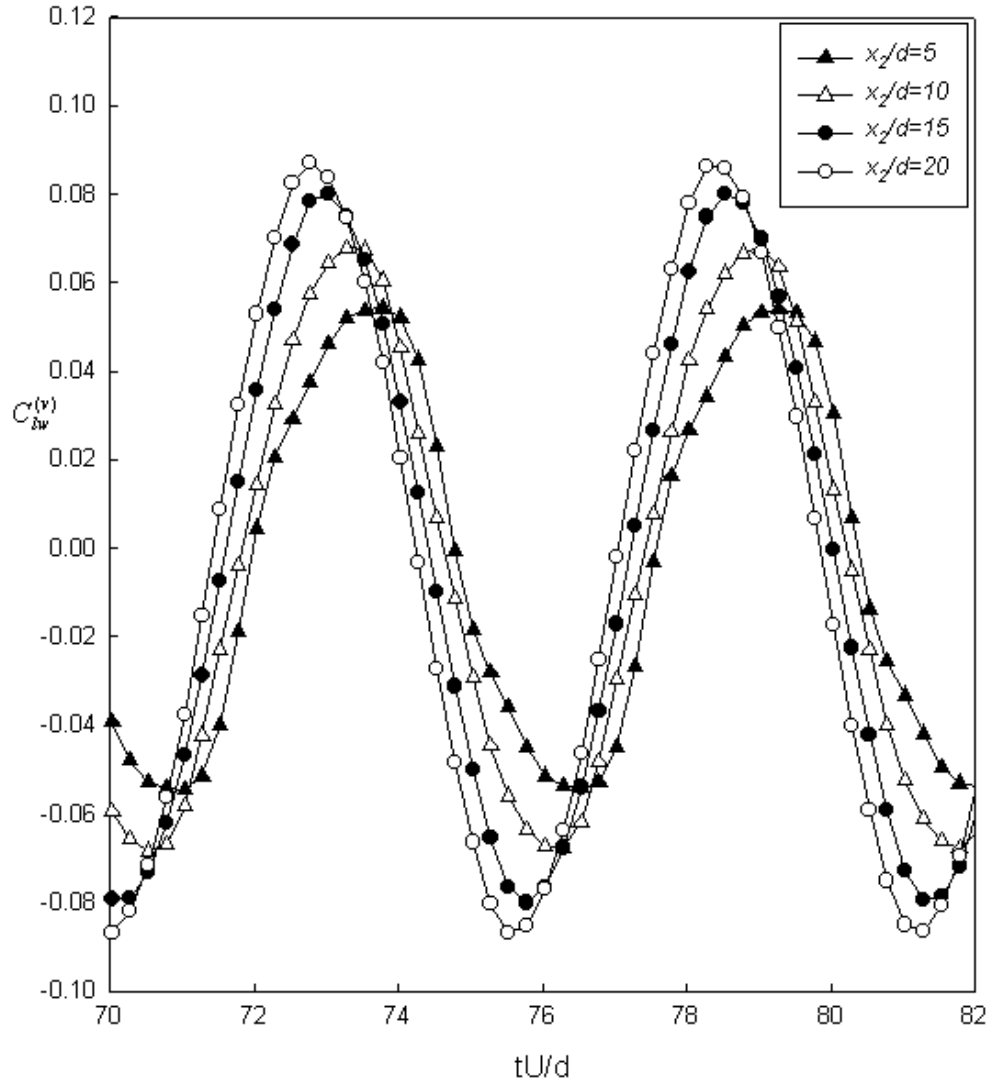
Fig 4.6 Time traces of wake vortex lift force obtained from Eq. (4.10) within different wake domains. The lower, upper and left bounds of the domain are fixed at $y_1/d= -0.75$, $y_2/d= 0.75$ and $x_1/d= 0.5$. The right bound is movable and set at four locations $x_2/d= 5, 10, 15$ and 20.

4.4 Bound circulation determination

In section 4.3, we focused on the wake vortex force derivation based on Lighthill's concept. In some sense, the contribution of the vortex force to the total lift is similar to the concept of wake circulation contribution in Wu's work (1981). In chapter 2 and 3, we also have shown that contribution from the time-dependent bound circulation in a region enclosing the cylinder is of significant importance. Our corrected unsteady approximation, equation (2.9), can properly convert the time-dependent bound circulation to instantaneous lift force. As a result in the same spirit of chapter 2, issues related to bound circulation determination will be studied. In this section, we focus on proper selection of a closed sound path for bound circulation determination in stationary circular cylinder wakes.

Using the same algorithm for circulation determination introduced in chapter 3, we can easily calculate the value of circulation around an arbitrary closed path, and study the effect of path size and location on bound circulation determination. Due to the geometry of circular cylinders, we select a square shaped path with the center located at the center of the cylinder as done by Obasaju & Bearman (1988). By varying the side length of the square path (a), the bound circulation variation with length a can be obtained.

Fig 4.7 shows this path variation for bound circulation determination. Five typical paths, A, B, C, D, E are highlighted to study effect of near-wake vortex structures including the attached and shed vortices labeled in the figure. The attached vortex develops in close proximity to the cylinder and later sheds down stream (see Fig
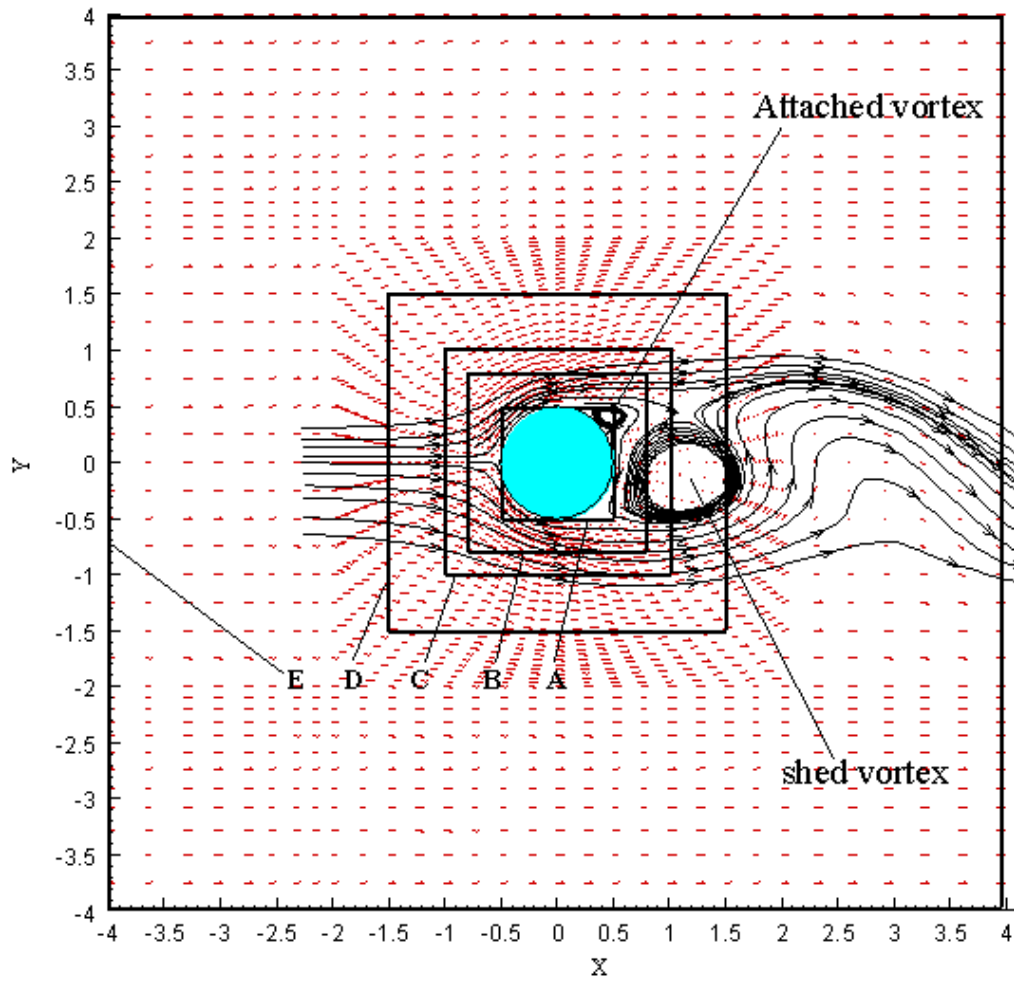
Fig 4.7 Schematic of path selection for bound circulation determination around circular cylinder. Re=100, tU/d=76.875. Five typical paths are highlighted to study the effect of near-wake vortex structures on bound circulation values. Define *a* as the length of one side of the square paths, for path *A, a/d=1.0*; path B, *a/d=1.6*; path C, *a/d=2.0*; path D*, a/d=3.0*; path E, *a/d=8*.
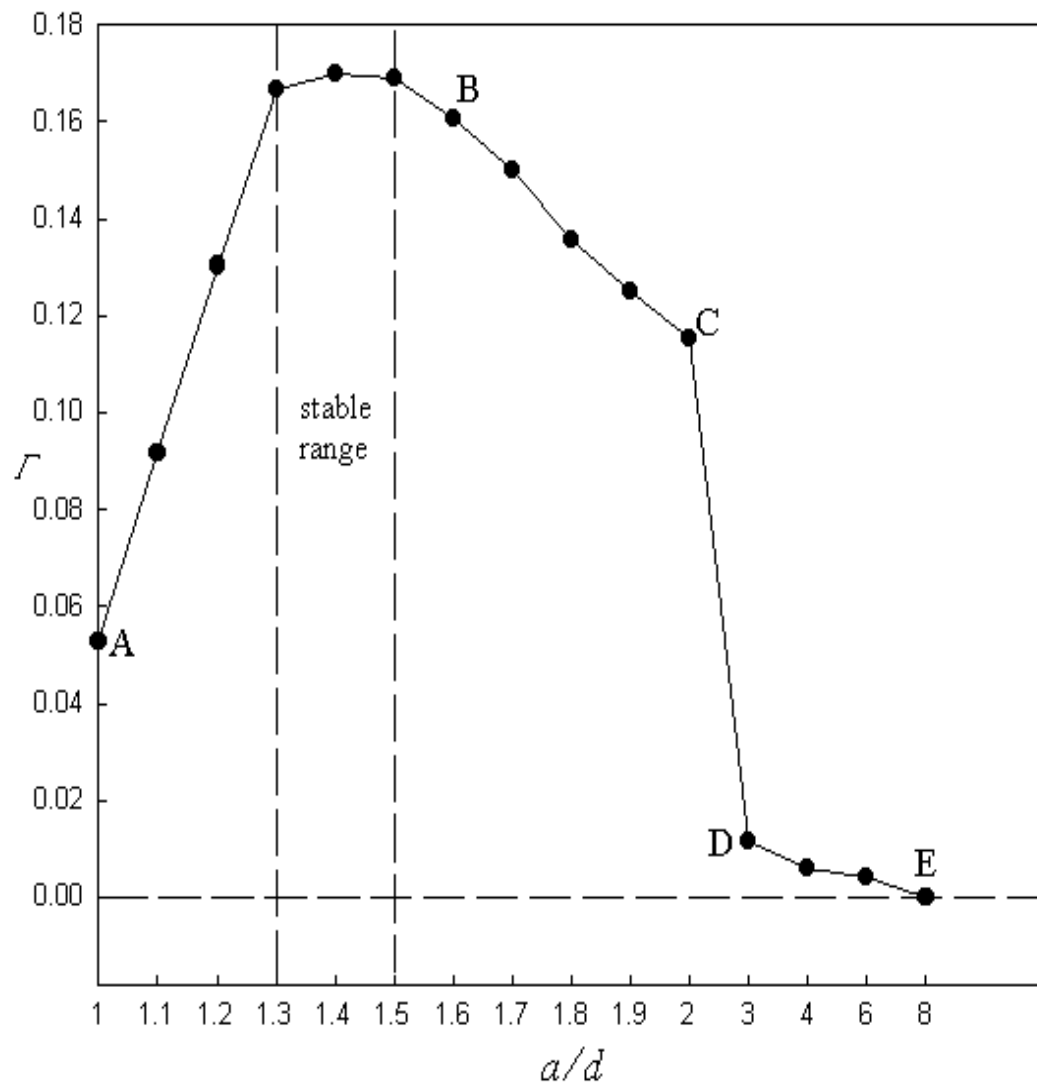
Fig 4.8 Bound circulation Γ at an instant of time variation with the size of the closed paths. A small stable range exists in the plot where Γ is independent of *a/d,* These results can serve as a useful guide for closed sound path design in UCMT experiments. Labels A, B, C, D, E correspond to paths highlighted in Fig 4.7.

4.4). The smallest path A just encloses the circular cylinder, with each of its legs tangential to the cylinder.

Fig. 4.8 shows the variation of bound circulation with the size of the paths defined in Fig 4.7 along with further intermediate path sizes. This plot shows that bound circulation increases with an increase in path size starting from path A, then it comes to a stable area in which the bound circulation becomes independent of path length while reaching its maximum value. With further increase of a/d, area enclosed by the path begins to include shedding vortices in the wake. The shedding vortices contain opposite signed vorticity compared to the attached vortex in the other shear layer. This addition of opposite signed vorticity causes the total bound circulation to decrease with increase in a/d. For $a/d \geq 5$, the bound circulation $\Gamma(t)$ approaches zero. As the path becomes larger and encloses additional shed vortices, the vorticity of these shed vortices dominate the effect of the attached vortex. Since the downstream vortex street contains alternating vortices of opposite sign, the measured bound circulation becomes negligible.

Based on the above results, a proper path should be selected from the stable area that covers from $1.3 < a/d < 1.5$ In Obasaju & Bearman's experiments (1988), a value of $a/d = 1.35$ was used, which closely matches our optimum path. We will determine the bound circulation using this selected path in our later analysis of lift forces on circular cylinder. Here, we can conclude for the path selection: For bound circulation determination, sound path should include the attached vortex, but not include any part of the separated shedding vortex. This fact can act as a guide for future UCMT

experiment design. As detailed in chapter 3, the path sensitivity study also has implications for PIV and LDV studies. We should point out that the optimum path a/d=1.5 may have some practical limitations. This path implies acoustic sound legs in close proximity to the cylinder that may require acoustic mirrors that disturb the flow. However, in an experiment, rectangular acoustic paths, with y_1/d and y_2/d legs placed further away from the cylinder and near the wind tunnel walls, could be used successfully. These issues require further study.

4.5 Results and discussion

In this section, we present lift force results from our numerical simulations based on different force models and compared these results with the true lift obtained from the stress integration method. The wake vortex lift force is based on Lighthill's concept, which is expressed in equation (4.10). The quasi-steady lift force is based on Kutta-Joukowski theorem, where $\Gamma(t)$ is the bound circulation within the optimum sound path (section 4.4). Osbasaju & Bearman (1988) used this approximation in their experimental work. The lift force from our corrected unsteady approximation (2.22) is based on unsteady potential flow theory and can count in the unsteady effects. A variation of this approximation will be applied later in this chapter. Finally, we will put forward a new lift model in this section to combine the quasi-steady, wake vortex and unsteady lift models.

Next, we present lift curves from the numerical simulation for the true lift C_l, wake vortex lift $C_{hw}^{(v)}$, vortex lift $C_l^{(v)}$ (including contribution from bound and wake

circulation) and the quasi-steady lift $C_l^{(1)}$ (K-J theorem) in Fig 4.9. $C_l^{(1)}$ is determined using the bound circulation obtained from the optimum closed path selected in section 4.4. The vortex lift $C_l^{(v)}$ shows the largest phase angle lag behind the true lift C_l, and its peak-peak amplitude is larger than C_l, a 15% deviation of lift rms amplitudes is observed between C_l and $C_l^{(v)}$. This deviation should be due to approximation introduced in derivation of Eq. (4.10). However, it is interesting to note that in Rockwell's experimental work using PIV technique (see Fig.4.2), similar deficiency between Lighthill's vortex lift and true lift was observed. Compared with the vortex lift $C_l^{(v)}$, the quasi-steady lift $C_l^{(1)}$ better matches the true lift curve. Because $C_l^{(1)}$ doesn't include the viscous effects (accounted by vortex lift), we next study the combination of $C_l^{(1)}$ and $C_{lw}^{(v)}$. However, due to the large phase difference ($\approx \dfrac{\pi}{2}$) between $C_l^{(1)}$ and $C_{lw}^{(v)}$, the combination of $C_l^{(1)}$ and $C_{lw}^{(v)}$ becomes less accurate than $C_l^{(1)}$ in terms of phase angle prediction, and little improvement is noted for the rms lift. The best prediction occurs for the quasi-steady case where values in phase difference of $\beta \approx 45^0$ between this case and the true lift are observed. This may serve as some justification for use of the quasi-steady approximation in earlier wake studies (Obasaju & Bearman, 1988). However, we will next see that better lift prediction on circular cylinders can be obtained by incorporating unsteady effects using the framework of chapter 2.

Since the lift approximation $C_l^{(1)}$, or various combinations using an approximation based on Lighthill's vortex force concept, cannot predict the true lift C_l
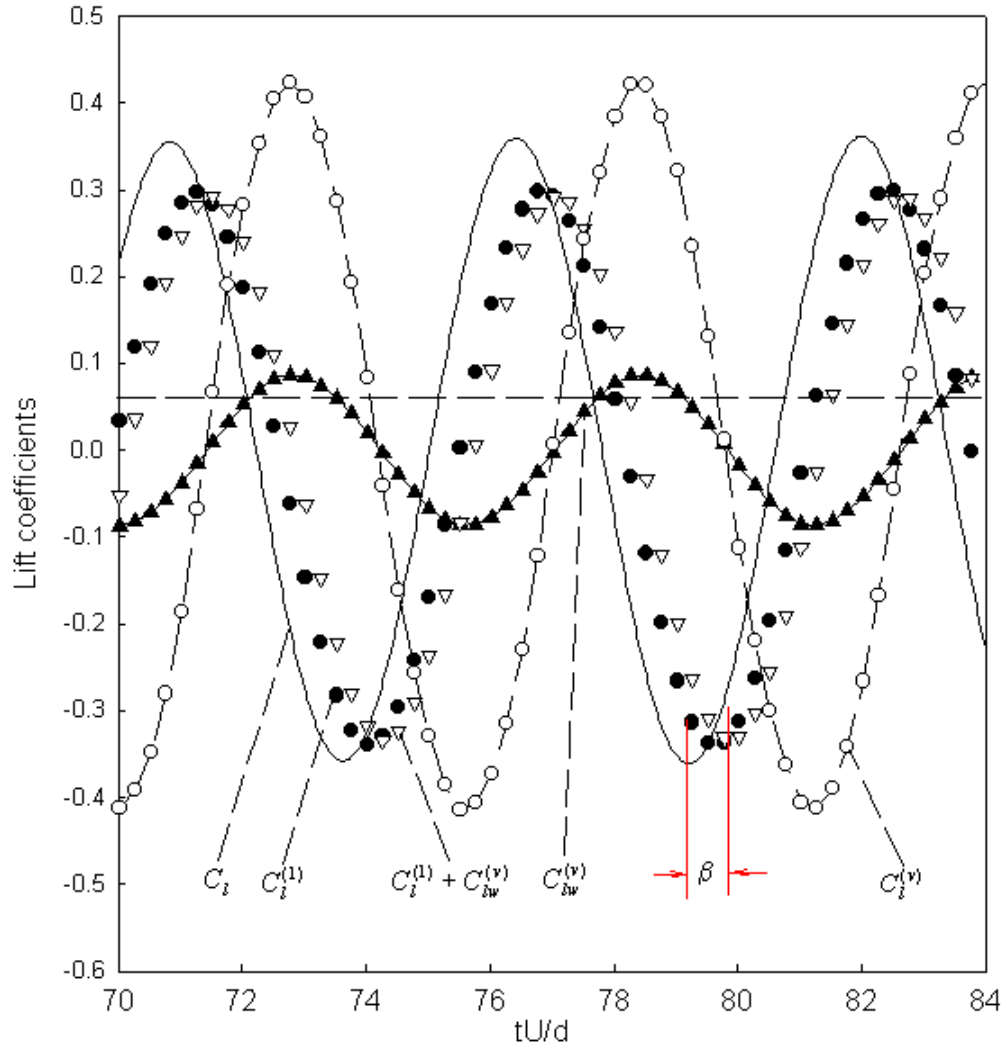
Fig 4.9   Comparison between true lift force C_l, quasi-steady lift $C_l^{(1)}$, wake vortex lift $C_{lw}^{(v)}$ and vortex lift $C_l^{(v)}$. Vortex lift is obtained from Eq. (4.10) within the selected domain. Quasi-steady lift is determined from K-J approximation. β is the phase angle between true lift and $C_l^{(1)} + C_{lw}^{(v)}$.
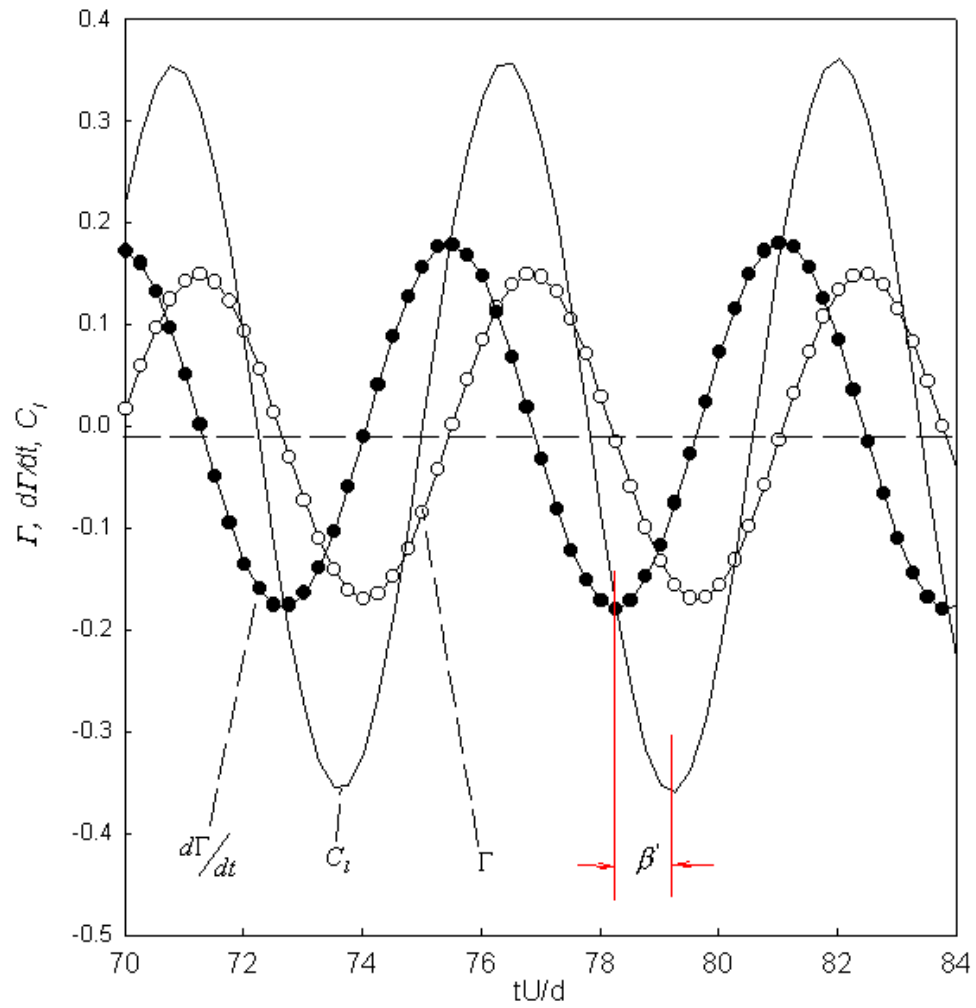
Fig 4.10 Phase comparison of true lift C_l, bound circulation Γ and its first derivative $d\Gamma/dt$, which will be used for unsteady effect correction.

well, we next consider if the unsteady nature of the bound circulation can be used to increase lift prediction accuracy. In Fig 4.10, we present the results of the time variation of the bound circulation Γ and its first derivative $\dfrac{d\Gamma}{dt}$ that was used in our corrected unsteady approximation in chapter 2. We focus on the phase angle difference β' between the $\dfrac{d\Gamma}{dt}$ curve and C_l curve defined in Fig 4.10, and find $\beta' \approx 60^0$ with $\dfrac{d\Gamma}{dt}$ leading C_l. In Fig 4.9, we have seen that the phase angle $\beta' \approx 45^0$ with C_l leading $C_l^{(1)} + C_{lw}^{(v)}$. This suggests that $\dfrac{d\Gamma}{dt}$ curve (which describes the unsteady effect) has the proper leading phase to correct our lift predictions. As a result, we next study inclusion of an unsteady term into our lift approximations.

In our corrected unsteady method in chapter 2, we developed the following approximation

$$L^{(3)}(t) = \rho U \Gamma(t) + R\rho d \frac{d\Gamma(t)}{dt} \quad . \tag{2.36}$$

Eq. (2.36) was obtained after applying unsteady potential flow theory, focusing on the bound circulation $\Gamma(t)$ that is obtained from a region enclosing the body. Eq. (2.36) can be converted to non-dimensional form giving

$$C_l^{(3)} = \frac{2\Gamma(t)}{Ud} + \frac{2R\dfrac{d\Gamma(t)}{dt}}{U^2} \quad . \tag{4.12}$$

We first use Eq. (4.12) to specify a value of the unsteady lift correction coefficient R, which was found to be ¾ for oscillating plate flow in chapter 2. For bluff circular cylinder flow, R will have a different value and may be a function of various

123

flow parameters such as Re etc. It may be possible to establish R analytically (similar to our work in chapter 2) using unsteady potential flow theory. Superposition of freestream flow along with doublet to model cylinder shape and a wake model would be required. In the present work, we have not undertaken this analysis, but instead we focus on a systematic study of the effect of R variation on lift results.

To accomplish this, we first choose to study the following lift approximation

$$C_l^{(4)} = \underbrace{\frac{2\Gamma(t)}{Ud}}_{quasi-steady\ force} + \underbrace{\frac{2R\dfrac{d\Gamma(t)}{dt}}{U^2}}_{unsteady\ force} + \underbrace{C_{lw}^{(v)}}_{wake\ vortex\ force} . \tag{4.13}$$

extending Eq. (4.12), we include the wake vortex force term (although we have shown it has negligible effect on lift prediction) to account all physical effects considered by previous investigators.

We next define a new rms error similar to chapter 2, where $C_{l(rms)}$ refers to the rms amplitude of the true lift value (stress integration)

$$e_{rms}^{(4)} = \frac{C_{l(rms)}^{(4)} - C_{l(rms)}}{C_{l(rms)}}. \tag{4.14}$$

Fig 4.11 presents the results of our systematic study of varying R by showing the variation of $e_{rms}^{(4)}$ with R. From this curve, we found that the best value of R for circular cylinder flow is $R \approx 0.4$. The proof that $R \approx 0.4$ should hold for a low Reynolds cylinder wake is left as a challenge to analysts in potential flow theory, and is an area of anticipated future work. However, study of our unsteady correction term in Eq. (2.36) and Sarpkaya's generalized Blasius theorem of Eq. (1.17) yields some interesting

findings. By comparing the final terms in Eq. (1.17) and Eq. (2.36), we can see that $r_{k_i} \approx Rd$. If we treat r_{k_i} as a constant and Γ_k as the bound circulation, the parameter r_{k_i} represents the location of a vortex element in the flow. Then $r_{k_i} \approx Rd = 0.4d$ is obtained using our result from Fig. 4.11. This says that the primary vortex element determines unsteady lift in Eq. (2.36) is located at $R = \dfrac{r_{k_i}}{d} = \dfrac{x}{d} = 0.4$. Now study Fig. 4.7, the attached developing vortex is located at $\dfrac{x}{d} = 0.4$, suggesting that it is the attached vortex development dominates the unsteady lift creation. It is physically plausible that the attached vortex adjacent to the cylinder in the near wake has a dominant effect on unsteady lift creation, compared to vortices at larger $\dfrac{x}{d}$ values.

Fig 4.12 presents comparison of lift curves using the approximations in Eq. (4.12) and (4.13). We first observe that the $C_l^{(4)}$ lift approximation (with $R \approx 0.4$) best approximates the true lift curve. While there is excellent agreement between the two curves in rms amplitude (as required by Fig 4.11), small phase difference still exists. For comparison, we also present the results for $C_l^{(3)}$ (Eq. (4.12)) which deletes the wake vortex force effect. Degradation in lift prediction is observed. We do however note that this approximation could also be adjusted to better match the true lift curve through an additional systematic study of R variation for this approximation, similar to Fig. 4.11.

From this chapter, we may conclude that reasonable prediction of lift force based on circulation method generally has to include unsteady effects, as long as the bound circulation is varying with time. Lighthill's vortex lift force concept, when

applied over the entire flow, using a UCMT based technique, results in approximate 15% error in lift rms amplitude compared to the true integrated lift. As a result, an alternative lift model based on measuring bound circulation with an acoustic path enclosing the cylinder is proposed.

$$e_{rms}^{(4)} = \frac{C'^{(4)}_{l\ rms} - C_{l(rms)}}{C_{l(rms)}}$$
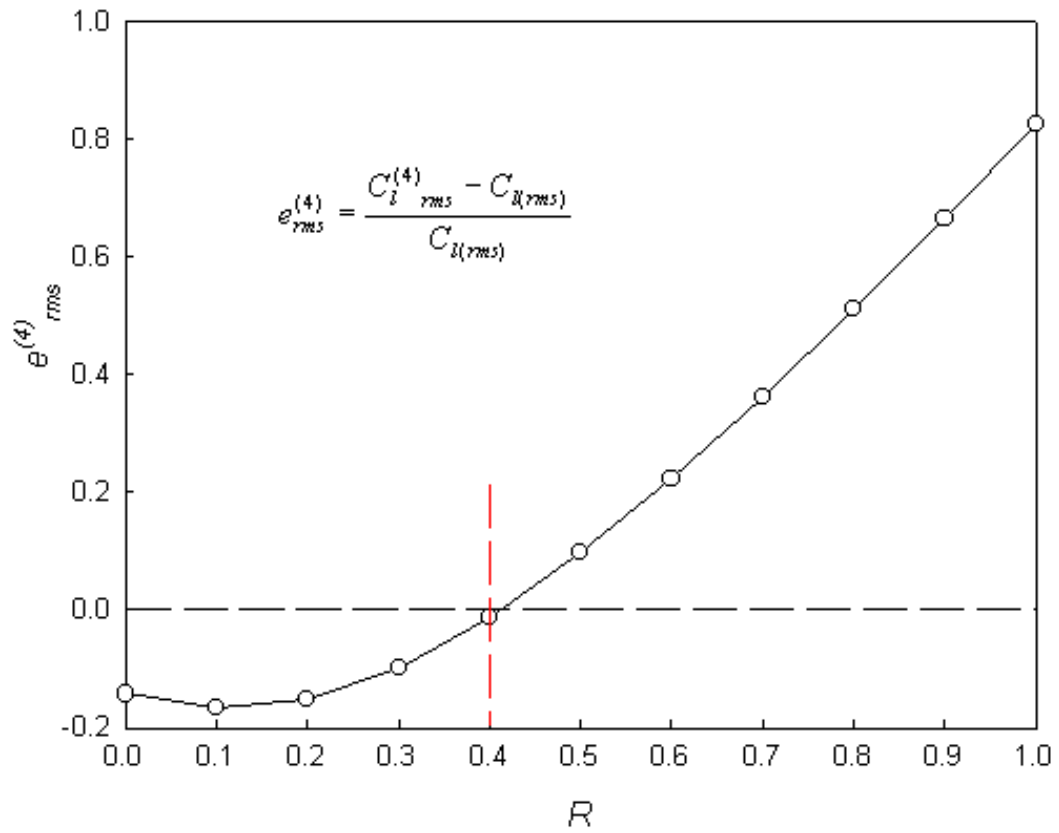
Fig 4.11 Rms error of lift $C_l^{(4)}$ approximation with variation in unsteady lift correction coefficient R. $R \approx 0.4$ for circular cylinder flow yields $e_{rms}^{(4)} \approx 0$.
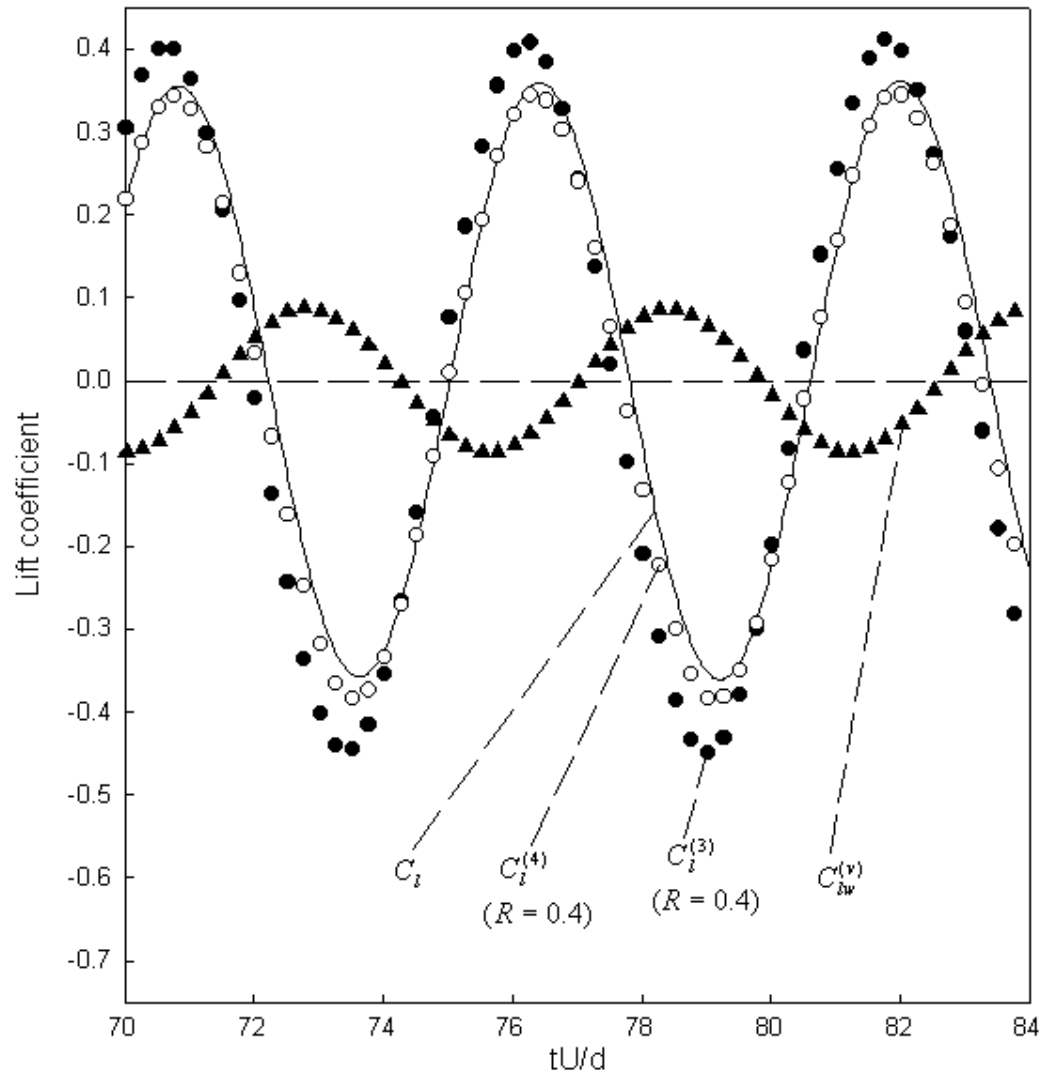
Fig. 4.12 Comparison of lifts between true lift C_l, vortex lift $C_l^{(v)}$, unsteady corrected lift $C_l^{(3)}$ (K-J theorem + corrected unsteady) and total lift $C_l^{(4)}$ (K-J theorem + corrected unsteady + vortex force).

Chapter 5

Experimental UCMT study on Three-dimensional Flows

5.1 Introduction

To expand the capability of UCMT for lift determination in unsteady and three-dimensional flows, we have developed methods to properly convert the time-dependent bound circulation measurable with UCMT to instantaneous lift in chapter 2 and 3, based on unsteady potential flow theory. In chapter 4, we studied the instantaneous lift in bluff body flows, by applying our developed methods along with Lighthill's vortex force concept in numerical simulations. However, we have not yet focused on lift determination in three-dimensional flows. This will be the main topic in this chapter in which we will conduct UCMT experiments to study the *mean* sectional lift distribution along aerodynamic bodies with three-dimensional features.

In UCMT experiments, it is possible to systematically study the spanwise lift distribution along structures. For our aerodynamic body, we select the flow around a flat plate because it has three distinct flow regimes dependent on angle of attack (AOA). At smaller AOA, it can be characterized as streamlined flow; at intermediate AOA, a stalled flow; and at larger AOA, it becomes a bluff body flow. As a result, outcomes from a flat plate flow study should have broad application. Furthermore, it is convenient to design and fabricate plates with a variation in chord length along the span to study the three-dimensional lift distribution.

In the past, most investigations on three-dimensional flows have focused on vortex generation and shedding patterns behind the body. For example, Nuzzi *et al*

(1992) studied the three-dimensional vortex formation from an oscillating, non-uniform cylinder. The gradual variation of the cylinder diameter acted to 'detune' the highly coherent vortex formation in the spanwise direction and promoted the occurrence of non-periodic and period-doubled states. This approach can result in an effective destabilization of the near wake vortex formation leading to three-dimensional flow. Recently, considerable attention has also been paid on the development of three-dimensional flows from stationary plate trailing edges. Lasheras & Meiburg (1988, 1990) employed combined experimental and numerical approaches to study the evolution of the wake from the trailing edge of a thin flat plate at low AOA having spanwise perturbations. They found that an important feature of the three-dimensional flow is the induction of spanwise undulations of the large scale (Karman) vortices. Such undulations can exhibit either an in-phase or varicose pattern.

An important aspect of the investigation of three-dimensional flow is
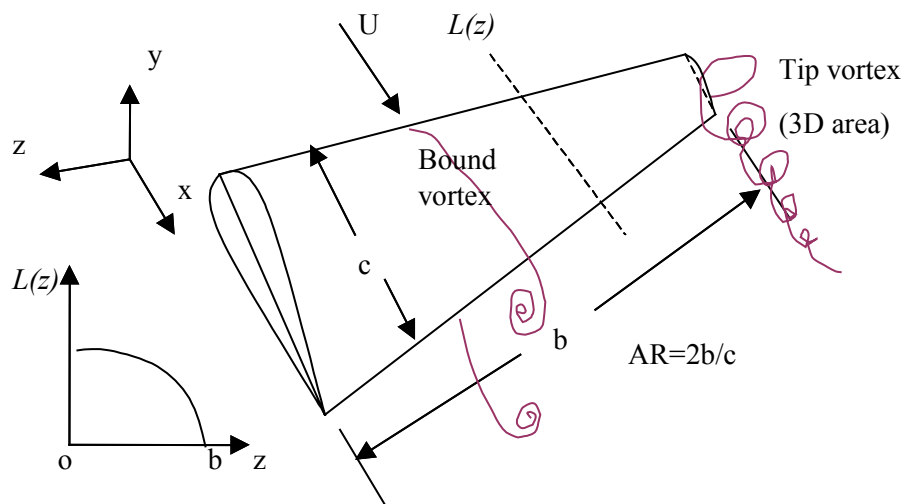
Fig. 5.1 Schematic of local sectional lift distribution on a finite wing

130

measurement of the local sectional fluid forces, which are crucial to aeroelastic analysis of structures such as aircraft wings (Fig. 5.1). However, past research in this direction is somewhat limited. Prandtl (1918, 1921) first analytically developed the lift line theory for predicting the lift distribution and induced drag on a finite lifting surface (wing). In his theory, he hypothesized that each spanwise section of a finite wing has a local lift equivalent to that acting on a similar section of infinite two-dimensional wing having the same circulation. This assumes negligible flow in the spanwise direction along the wing. However, this assumption is easily violated if three-dimensional flow exists. Recently, Bastedo et al (1985) experimentally studied the finite wing performance with a pressure measurement method at low Reynolds number Re = $8\times10^4 \sim 2\times10^5$. For a rectangular wing with *AR=4*, the agreement between lift from Prandtl's finite wing theory, and the measured local sectional lift based on the integration of the local pressure distribution became worse with an increase of angle of attack (Fig 5.2a). Bhagwat et al (2000) employed Laser Doppler Velocimetry to measure the spanwise bound circulation distribution on a rectangular wing with *AR=9.6*. As opposite to Prandtl's smooth lift distribution, a peak was found in the measured circulation distribution at a location near the tip area where strong three-dimensional flow exists (Fig 5.2b). Due to various experimental limitations, the above investigations could not measure the lift or circulation distribution along the whole span. Our effort in this chapter includes experiments to accomplish this to learn more about this type of three-dimensional flow.

Another research area that has been arisen recently is the study of low aspect ratio (AR) wings at low Reynolds number. These wings have application in the design of micro aerial vehicles (MAVs), which are small aircrafts with maximum dimension less than 25cm. MAVs can be used as surveillance or reconnaissance vehicles to carry visual, acoustic, chemical or biological sensors in military or commercial applications. For these vehicles, the accompanying chord Reynolds numbers are in the range of $Re=2\times10^4$ to 2×10^5. This presents numerous aerodynamic challenges to the designer of MAV. Very little data exists for low Reynolds, low aspect ratio wings, and the applicability of exist model such as Prandtl's lift line theory should be rigorously examined. Also, details of the spanwise lift distribution are critical to MAV design. Particularly in swept low AR wings, this lift distribution determines the location of the MAV center of pressure and neutral point and thus is critical in determining aircraft stability. Control and stability of MAV aircraft is a current challenge due to their small size. Experimental studies (Bastedo & Muller, 1985; Pelletier & Muller, 2000) have been conducted to determine the total lift and drag forces in low Reynolds, low AR wings. However, little attention has been placed on measurement of local sectional lift distributions.

In the following sections, we will present experimental lift results obtained from UCMT and force balance measurements. In section 5.2, we will describe the experimental apparatus for our three-dimensional flow studying. Data processing and analysis will be described in section 5.3. In section 5.4, two-dimensional flow over a flat plate for a wide range of AOA is studied to validate our experimental methods. In

(a)

(b)
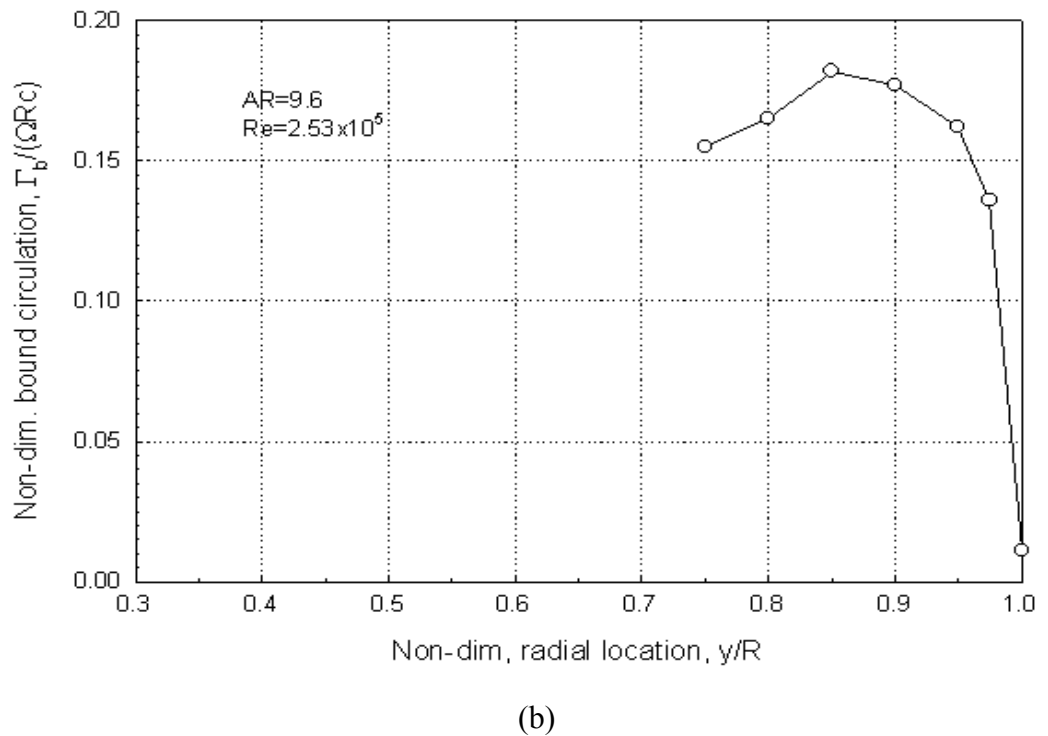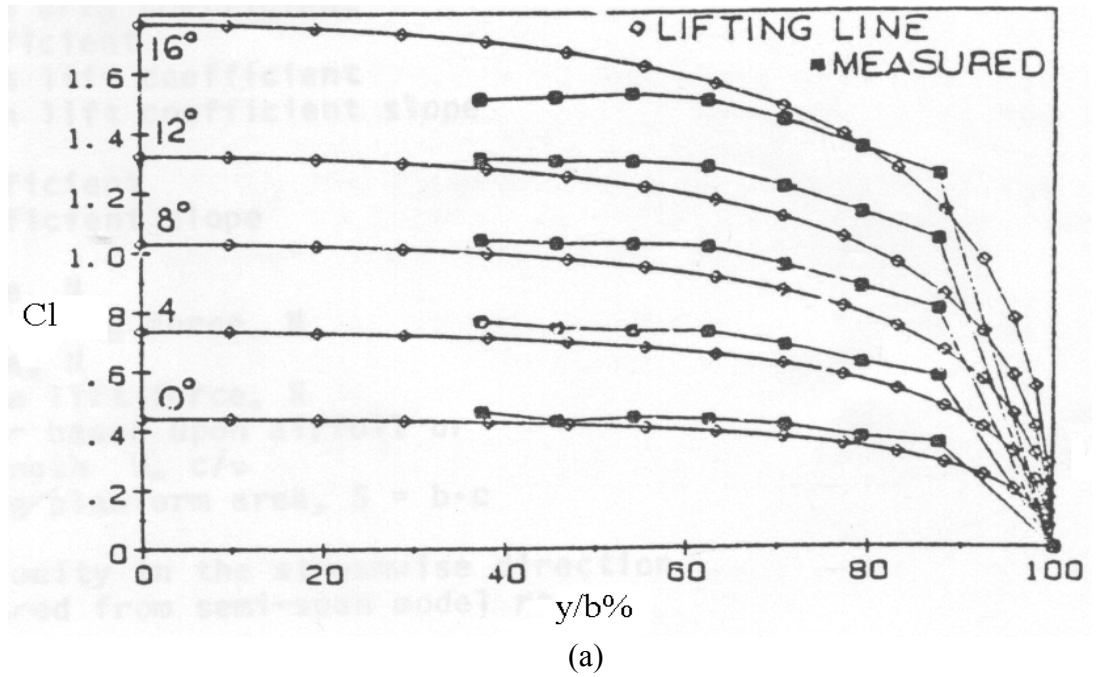
Fig 5.2 (a) Comparison of lifting line predictions with spanwise lift distribution obtained from integrated pressure distribution for $Re=2\times10^5$ and $AR=4$ (Fig.9 in Bastedo et al (1985)). (b) LDV measurement of bound circulation along airfoil span at $Re=2.53\times10^5$ and $AR=9.6$ (Fig. 12(a) in Bhagwat et al (2000)).

133

section 5.5, we present a study of flow over flat plate with local chord length variation along the span. In section 5.6, we will study lift distribution on low Reynolds number, low aspect ratio wings applicable to MAV design. Finally, we will summarize our experimental study in section 5.7.

5.2 Experimental apparatus

Measurements presented in this chapter were conducted in two low-speed wind tunnels located in the Mechanical Engineering Department in Worcester Polytechnic Institute. All of the UCMT testing was conducted in an open circuit wind tunnel (hereafter tunnel 1). Force balance lift measurements were conducted in tunnel 2, a closed circuit tunnel.

5.2.1 Experimental study for UCMT measurements

The entrance of tunnel 1 includes a honeycomb straighter to uniform flow, and four wire mesh screens used to reduce turbulence intensity. The contraction ratio is approximate 12, with entrance size of 165cm × 206cm. The test section has dimensions of 45.7cm (height) by 61cm (width) by 91.4cm (length); The available velocity range is $3m/s \leq U \leq 64m/s$, measurable with a Pitot-static tube set at a location near the entrance of the test section; Free stream turbulence intensity measured from hot-wire anemometry is approximate $0.07 \leq \varepsilon' \leq 0.09$. A downstream diffuser connects the test section to the fan assembly consisting of 75hp 3-phase induction motor driving an axial

fan. Tunnel speed control is accomplished by adjusting damper vanes located upstream of the inlet to the blower.

A schematic of the test setup is shown in Fig. 5.3. A triangular ultrasound path was constructed for circulation measurement shown in Fig. 5.3a. The triangle path was also used in the work of Desabrais (1998) who verified UCMT measurements on a 2D airfoil based on comparison with results measured from a load cell force balance. In Fig. 5.4, we present a scaled schematic of the triangular sound path. It is noted that we measured spatial circulation distributions based on this triangular path (which is not the optimum path) prior to studying the path sensitivity. The triangular path is compared to the allowed acoustic path locations (Fig. 3.7) from the path sensitivity study of chapter 3. Our main concern is that the downstream acoustic reflector is at an x_2 position larger than that allowed in Fig 3.7. Study of Fig 3.6b shows that measured circulation values would be expected to decrease if the downstream reflector is at larger x_2/c values (here $x_2/c \cong 3$), suggesting the triangular path may slightly underpredict Γ values. We also note that the Reynolds numbers are different in our experiments compared to the simulation of chapter 3, so these trends are only speculative.

In real experimental test, the sound path may not keep as straight geometric line due to the effects of turbulence and wake vortex flow. This may affect the final measurement precision. However, these effects may be negligible considering the freestream velocity is just 5m/s, far less than the sound speed (340m/s) in air.

In UCMT test, two 100KHz ultrasonic transducers (3/4" diameter, bandwidth about 20KHz) from Panametric were used as both transmitter and receiver to generate

Top View

Acoustic reflector

x

o

W

y

Sound path   plate

Side wall of W.T.

U

cable

computer

Panametric
GP68

Flowmeter   preamplifier

Ultrasound
transducers

W.T. size: WxH=24"x18"

(a)

Side View

Rotating Plug

z

x

o

plate

End plate

H

smoke

U

Light sheet

bottom wall of W.T.

300w ELH High
Energy Bulb

camera

Smoke Generator
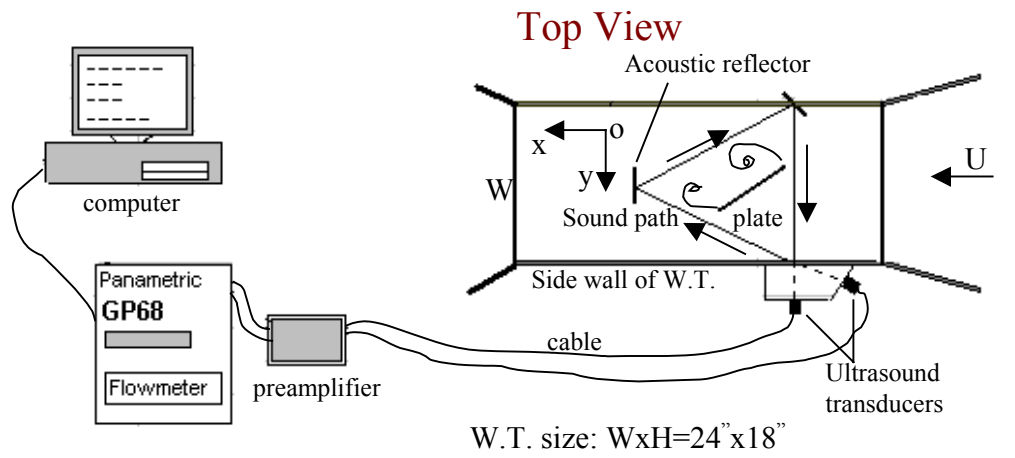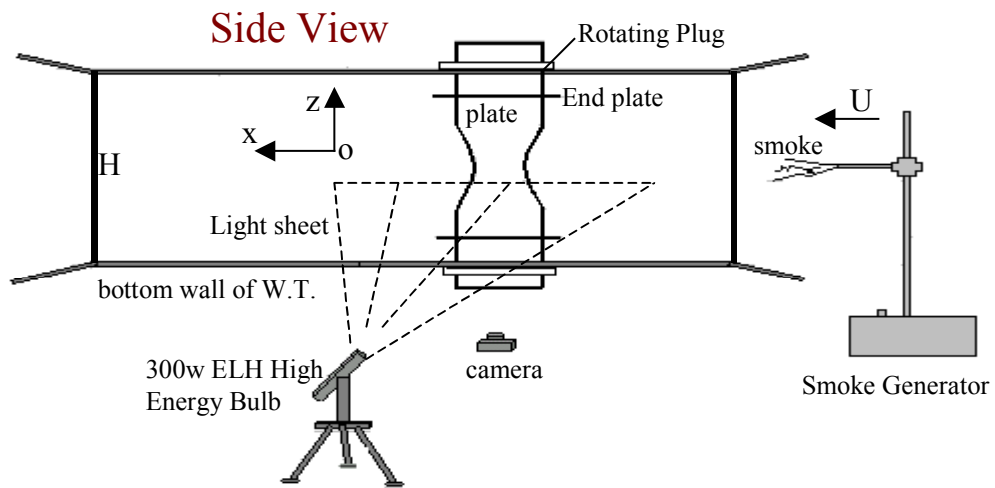
(b)

Fig 5.3 Schematic of the experimental arrangement in tunnel 1. Spanwise lift distributions along plates with chord length variation are studied. (a) Setup for UCMT measurement. (b) Setup for smoke visualization.
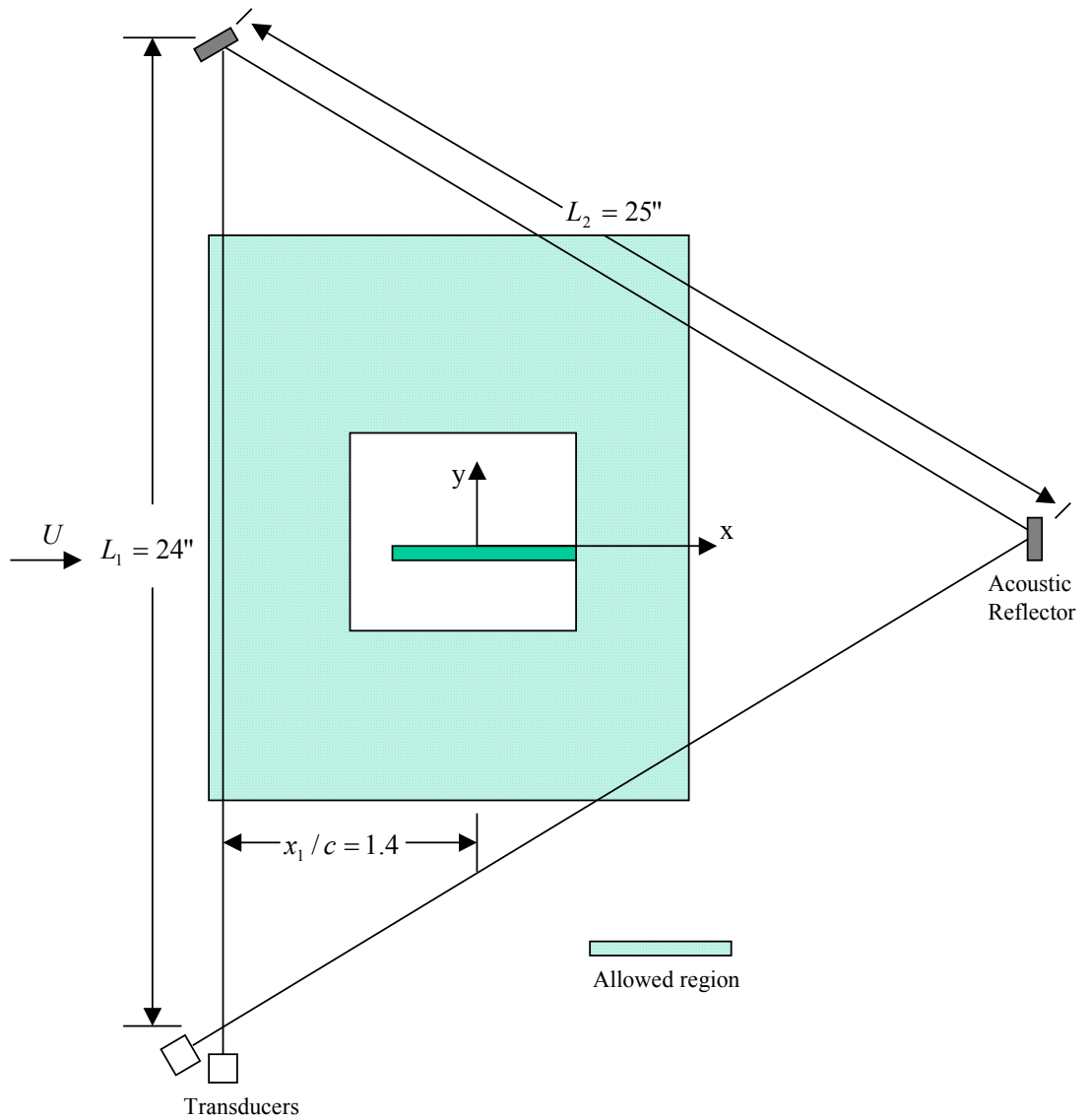
Fig. 5.4 Diagram of the closed triangular acoustic path and its relative location to our allowed region from the path sensitivity study.

and receive sound pulses, and two acoustic reflectors (mirrors) were used for redirecting the acoustic pulses. The broadening of pulse width and deflection from its undisturbed propagation direction due to freestream flow in the tunnel was carefully calculated and checked. A Panametric GP68 Flowmeter controlled the emitted and received sound pulses and measured their average transit times. These transit times are critical for mean circulation measurement.

A PC based data acquisition system was used for data storage and post-process. Two Panametric model PRE-120 preamplifiers were used to amplify the signals received from the transducers. Each measurement of the transit time was obtained by averaging approximately 100 data acquired over 7 seconds and stored in a data acquisition file. The relationship between the measured transit times and the circulation has been described in chapter 1 as

$$\Gamma = \frac{1}{2}a^2(T_{cw} - T_{ccw}) = 2(\frac{l_p}{T_{cw} + T_{ccw}})^2(T_{cw} - T_{ccw}) \ . \tag{1.21}$$

where a is sound speed, l_p is the total length of sound path, T_{cw}, T_{ccw} are the transit times (Johari & Durgin, 1998).

The total length of the closed sound path l_p was carefully measured as 201cm. Transducers and acoustic reflectors were recessed into cavities in the test section walls to reduce disturbances to the flow field. In order to reduce cross-talk between transducers, rubber O-rings were used to isolate the transducers from each other and the supporting structure.

The effect of interference from boundary layers on the tunnel walls was assumed negligible because of the symmetry of the designed sound path. The vorticities in the

boundary layers on opposite sides of the tunnel were assumed to have equal and opposite signs. Furthermore, a small baseline circulation that was measured in the tunnel with the flow on, but with no flat plate in place, was subtracted from the circulation measurements.

Calibration of the UCMT setup in still air showed that resolution of the GP68 Flowmeter measurement was about *50* ns, which corresponded to an error about *2.3%* in circulation values, based on the measured transit time at *U=5m/s* and plate angle of attack of $\alpha=6^0$. In addition, a barometer and a thermometer were used to measure the ambient temperature and pressure for accurate determination of air density and sound speed.

In order to correlate the measured lift distribution to the flow structures in flat plate wake, a smoke flow visualization method was employed (Fig. 5.3b). A propylene glycol smoke generator was set in front of the wind tunnel entrance to provide smoke as a flow tracer. A 300W ELH high energy bulb provided a light sheet (with a thickness of about 1.5mm) to visualize the wake vortex flow in a two-dimensional plane. The spanwise (*z* direction) location of the smoke generator probe and the light sheet were fixed at the mid-point of test section height. The plates were vertically aligned in the tunnel (span in z direction), and the measurement of local circulation and flow visualization were implemented by moving the plate in *z* direction with the aid of two circular rotating plugs in the test section walls, which were designed to adjust the plate spanwise position and its angle of attack. In order to reduce interference from top and bottom test section walls, transparent end plates were designed following Stansby

(1974) and mounted on the plate, with a distance of about one chord length from the test section walls.

Four thin flat aluminum plates with thickness of 3.2mm and maximum chord length of 89mm were studied (Fig 5.5). Case 1 was a 2D plate used for validation of two-dimensional flow results. Case 2-4 were plates with sinusoidal varying chord length in the center section plate from $z=0$ to $z=z_0=6.35$cm. The chord length c(z) for case 2 and 3 was given by $c(z) = 7.874 - 1.016\cos(0.4947z)$. Case 2 was used to study the effect of trailing edge chord variation on lift distributions, and case 3 for studying the effect of leading edge variation. Case 4 was used to examine combined trailing and leading edge effects. Its chord length variation was $c(z) = 6.858 - 2.032\cos(0.4947z)$. The chord length variation was carefully machined on a CNC machine. For local circulation and lift measurements, 12 stations in z direction were tested with a resolution of $\Delta z=6.35$mm from $z=0$ to $z=1.1z_0$.
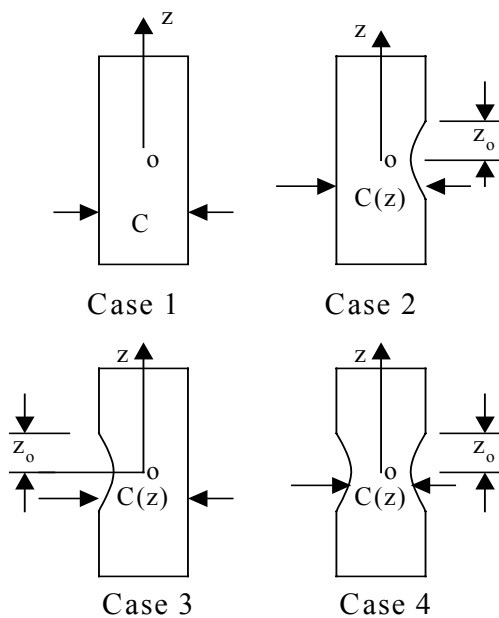
Table 5.1 Plate parameters

	Case 1	Case 2	Case 3	Case 4
z/z_0	c(z)/C	c(z)/c	c(z)/c	c(z)/c
0.0	1.0	0.7714	0.7714	0.5429
0.1	1.0	0.777	0.777	0.5541
0.2	1.0	0.7933	0.7933	0.5865
0.3	1.0	0.8134	0.8134	0.6268
0.4	1.0	0.8504	0.8504	0.7008
0.5	1.0	0.8857	0.8857	0.7714
0.6	1.0	0.921	0.921	0.8421
0.7	1.0	0.9529	0.9529	0.9058
0.8	1.0	0.9782	0.9782	0.9563
0.9	1.0	0.9944	0.9944	0.9888
1.0	1.0	1.0	1.0	1.0
1.1	1.0	1.0	1.0	1.0

Fig 5.5 Schematic of four plates with varying chord length used for study of sectional lift distribution on flat plates.

140

The spanwise lift distribution along low aspect ratio wings at low Re was also measured using UCMT in tunnel 1 (Fig 5.6a). The UCMT setup was the same as described in section 5.2.1. Plates were vertically aligned in the test section using a sting and support that was designed to move the plate in spanwise direction and change its angle of attack. The distance from wing tips of the low AR wings to the test section walls was always greater than one chord length to reduce wall effects on trailing vortices. Due to the symmetry of the wings, we measured the spanwise circulation and lift distributions along the upper half of the plates only.

5.2.2 Experimental setup for force balance measurement

Force balance measurements were conducted in tunnel 2 to further verify UCMT measurements (Fig5.6b). Wind tunnel 2 is a 24" re-circulating tunnel. Dimensions of its test section are 61cm wide by 61cm high by 240cm long. The free-stream velocity in test section can vary from 3m/s to 55m/s. Turbulent intensity is approximate 0.5% ~ 0.8%.

Force measurements were conducted with a LVDT (Linear Variable Displacement Transducer) dynamometer that was incorporated into the wind tunnel. The dynamometer is externally mounted to the bottom of the test section to independently measure lift and drag based on a internal beam deflection principle. These deflections are translated into a voltage change in the LVDT output signal filtered and amplified by a signal-conditioning unit (Popp, 2000). Calibration of the
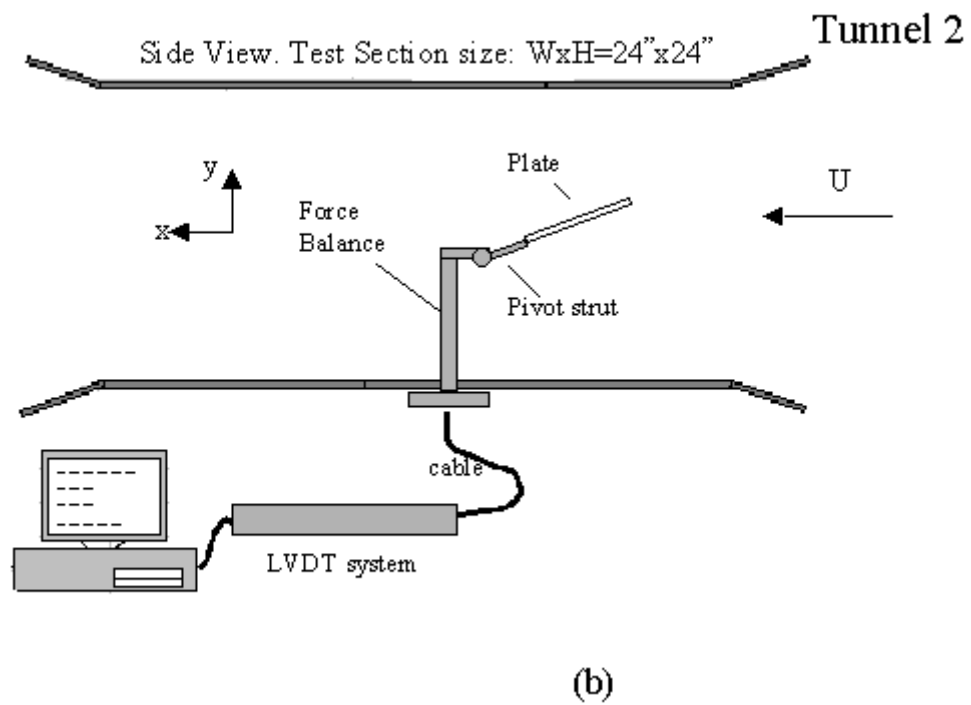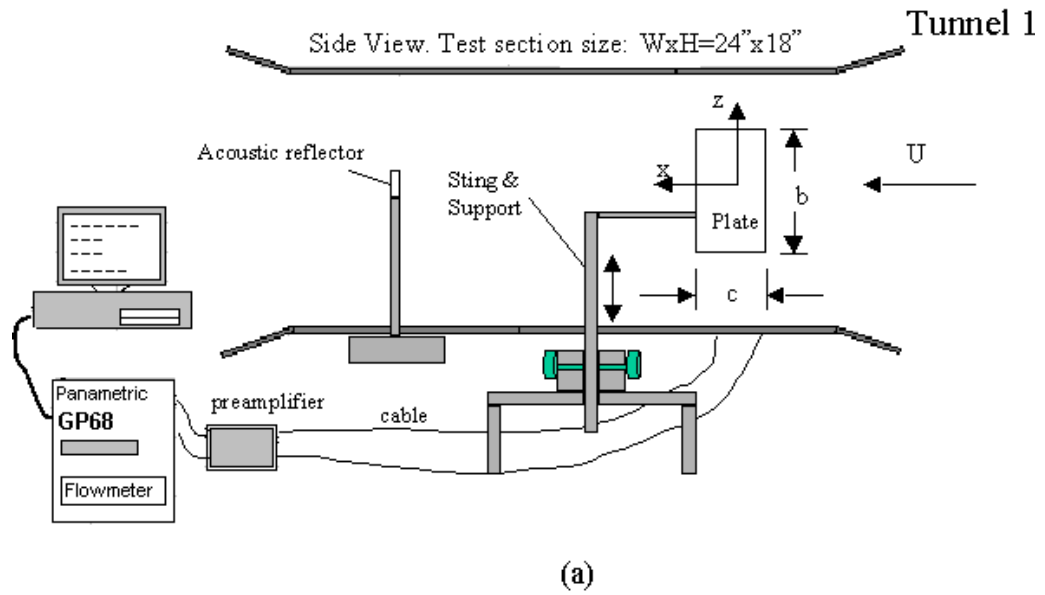
Fig. 5.6 Schematic of experimental setup for low aspect ratio wing study. (a) Arrangement for UCMT measurement of spanwise lift distribution along wings in tunnel 1. (b) Setup for force balance measurements in tunnel 2.

LVDT is using known external weight before and after each test run was conducted. Fig 5.7 shows a typical calibration curve used for lift measurements. Once the output voltage is collected by the signal-conditioning unit, it was sent to a Cyber Research[©] CYDAS 6402 HR data acquisition card, which interfaced with a PC through a commercial software package, HPVee[©], to visualize and analyze the acquired signal. It permits the user to alter the scan rate and time period for the recorded signal. Fig 5.8 is a typical acquired voltage signal in HPVee[©] with a sampling rate as 1000HZ and scan time of 6 seconds during the calibration process.

Table 5.2 Geometry of the four low aspect ratio wings

AR	b(cm)	c(cm)	Re
1	10.16	10.16	41,753
1.5	15.24	10.16	41,753
2	17.78	8.89	36,534
3	15.24	5.08	20,876

Four low aspect ratio plates made of aluminum were studied in wind tunnel 2 as part of our focus on low Re, low AR aerodynamics study. The plate thickness was 3.2mm, plate chord length c and span b are varying with aspect ratio, which were shown in Table 5.2. Free-stream speed of oncoming airflow in test section was set at $U=5m/s$, yielding Reynolds number (based on chord length of the plates) in the range of 2.1×10^4 to 4.1×10^4. The distance from wing tips of the low AR wings to the test section walls was always greater than one chord length to reduce wall effects on trailing vortices. Plates were horizontally aligned in wind tunnel test section and attached to a pivot strut
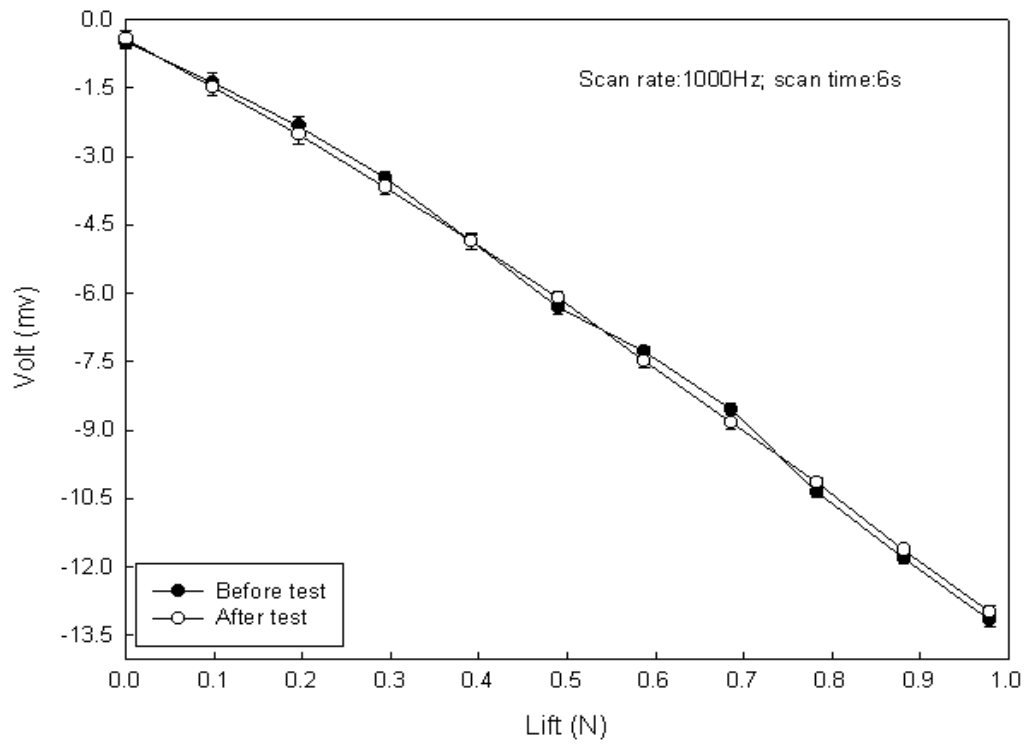
Fig 5.7 Typical calibration curves for lift measurement before and after test
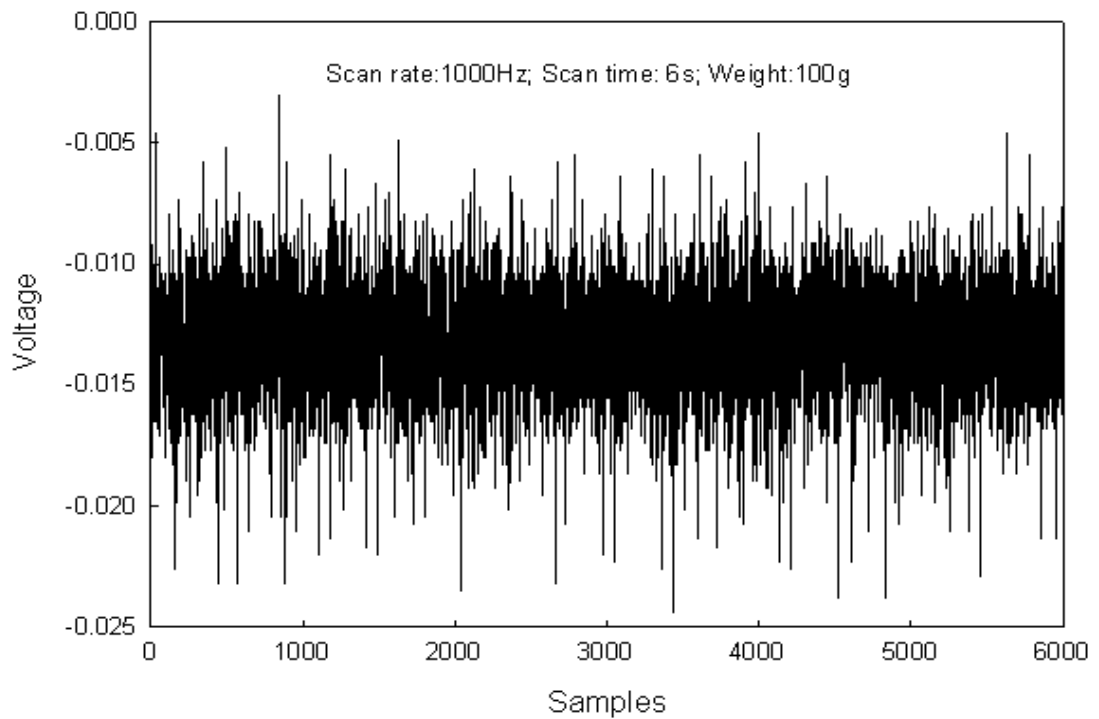
Fig 5.8 A typical output voltage signal in HPvee during calibration process.

used to vary plate angle of attack. One of the flat plates with leading and trailing edge chord variation (case 4 from section 5.2.1) was also studied in wind tunnel 2 using the force balance system.

5.3 Data analysis

All the test data measured by both UCMT and the force balance system was processed using standard statistic analysis. The Chauvenet method was used the reject abnormal data points. Data points where the absolute error (from mean value) exceeded three times standard deviation were eliminated.

Great care was also given to account for a base circulation value that occurred when the wind tunnel was running without the flat plates installed. This base circulation value, which was found to be approximately, $\Gamma_{base} = 0.0143$ m^2/s, was subtracted from all measured circulation values. When measuring this base circulation value, all experimental parameters were carefully adjusted to match later experiments with the flat plate present.

Finally, all results were corrected for solid blockage, wake blockage and streamlined curvature by using techniques presented by Pankhurst & Holder (1952) and Rae & Pope (1984). For example, the solid blockage was accounted for using

$$C_l = C_{lm}(1 - 2\varepsilon)[1 - (\pi\varepsilon)^2 / 48]; \quad \varepsilon = \frac{c}{w}\sin\alpha \ . \tag{5.1}$$

where ε is solid blockage, c plate chord length, w wind tunnel width, α the plate angle of attack. C_{lm} is the raw lift value and C_l the corrected value. Other correction expressions for 2D and 3D (finite wings) flows can be found in Rae & Pope (1984). The

required blockage correction for the low aspect ratio wings was only on the order of 2.2% because of their small thickness and volume.

5.4 Validation of UCMT measurement

The UCMT measurements were compared with force balance measurements either from previous investigations or from our LDVT measurement in tunnel 2. In this section, we present the lift force comparison for a 2D plate (with no chordlength variation) with the force balance data of Blevin (1984). We will also provide this type of comparison for the plates with chord length variation and low aspect ratio wings in later sections. The measured *mean* circulation values were converted to *mean* lift values using Kutta-Joukowski theorem. Smoke flow visualizations are also presented in this section.

Fig 5.9 presents the validation for a stationary 2D plate with chord length *c=8.89cm* in the test section of wind tunnel 1. The lift was converted from the circulation measured at the center of the plate in the spanwise direction. The lift comparison is shown in Fig 5.9a. The lift measured with UCMT shows that lift increases linearly with angle of attack in the range of $0^0 \leq \alpha \leq 8^0$ (streamlined flow regime). For $8^0 \leq \alpha \leq 15^0$, the lift decreases with angle of attack, it is in stalled flow regime. In the regime $15^0 \leq \alpha \leq 30^0$, the mean lift increases with angle of attack again, it is in transitional flow regime. After $\alpha > 30^0$ (bluff body regime), error bars (based on standard deviation of the UCMT measurements) abruptly increase, and the *mean* lift decreases after it approaches the maximum value at $\alpha = 40^0$. Fig. 5.9b presents smoke

(a)

(b) $\alpha=30^0$
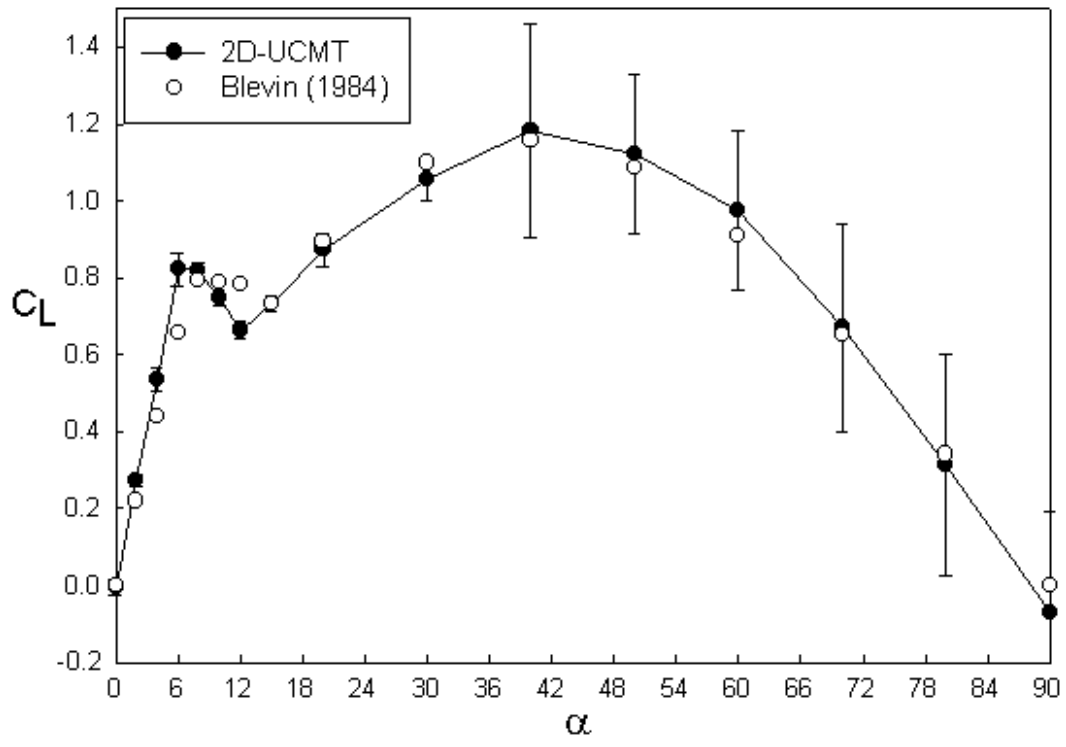
(c) $\alpha=40^0$

Fig 5.9 Validation of UCMT measurement for 2D flat plate flow at *U=5m/s*. (a) Comparison with force balance data published by Blevin (1984).   (b) Smoke visualized near wake structure at $\alpha=30^0$. (c) Near wake vortex structure at $\alpha=40^0$, vortex shedding process can be clearly observed.

visualization of the near wake vortex structure behind the plate at $\alpha=30^0$. A stable vortex is attached to the rear surface of the plate, and vortex shedding was not observed. In Fig 5.9c, the vortex shedding process in near wake at $\alpha=40^0$ is clearly shown. We believe the larger error bars accompanying the *mean* lift value in the bluff body flow are due to the effect of shed vortices on circulation measurements. The *mean* lift measured with UCMT agrees very well with the data of Blevin (1984), except in the stalled flow regime. However, the trends of both measurements are the same in this regime, with lift decreasing with angle of attack. Underprediction of lift values in the stalled flow region was also observed in Desabrais & Johari (1998), who studied *mean* lift on 2D airfoils.

Based on the error bars on lift measurement in Fig 5.9, we can conclude that for flow around a 2D stationary plate, the Kutta-Joukowski theorem can be used to predict the *mean* lift in the streamlined and transitional flow regimes. In bluff body flow, the instantaneous lift values should be predicted with the methods developed in chapter 4. However, for the *mean* lift prediction, K-J theorem can be applied (although with larger error bars) because the unsteady lift fluctuation generated by the periodic vortex shedding process is averaged to zero during the period of data acquisition over many shedding cycles.

5.5 Results for flow over plates with varying chord length

In this section, we present the *mean* lift force distribution along the span of the plates with chord length variation. The four plates described in section 5.2.1 were used in UCMT test. Each data point presented in this section is the *mean* lift averaged from 5

separate measurements. Lift distributions for streamlined flow ($\alpha=6^0$) and transitional

flow ($\alpha=15^0$) are presented.

5.5.1 Spanwise lift distributions

We next present lift distributions along the flat plate spans (z direction) in Fig

5.10 and 5.12. The local lift *L(z)* was non-dimensionalized with L_0, the measured lift

value for $z > z_0$ where the chord length is constant. In order to determine whether three-

dimensional flow is induced by curved leading and trailing edges, we also present the

nominal two dimensional lift distribution which was calculated based on local chord

length with

$$\frac{L(z)}{L_0} = \frac{c(z)}{c} \quad . \tag{5.2}$$

Here *c(z)* is the local chord length which is a sinusoidal function of the coordinate *z*, *c* is

the constant chord length for $z > z_0$. If the plate flow remains purely 2D, we would

expect that its distribution would follow Eq. (5.2). As a result deviations of measured

lift distributions for various plates will be a measure of the level of three-dimensionality

in the flow.

In Fig 5.10(a) for the streamlined flow, the deviation of the 3D lift distribution

from the nominal 2D is small. This shows that curved trailing edge generates slight 3D

effect on the spanwise lift distribution. However, in Fig 5.10b, a curved leading edge

yields a larger 3D variation, especially near center span area where the plate chord

length is minimum. Here the deviation between the 2 curves is almost 26%. This

demonstrates that leading edge dominates the flow development in streamlined flow.

Fig 5.10 *Mean* lift distributions along a plate with sinusoidal curved leading or trailing edge in streamlined regime ($\alpha=6^0$) at *U=5m/s.* (a) Trailing edge curved; (b) Leading edge curved; (c) Both leading and trailing edge curved; (d) Comparison of different cases.

(a)

(b)

(c)
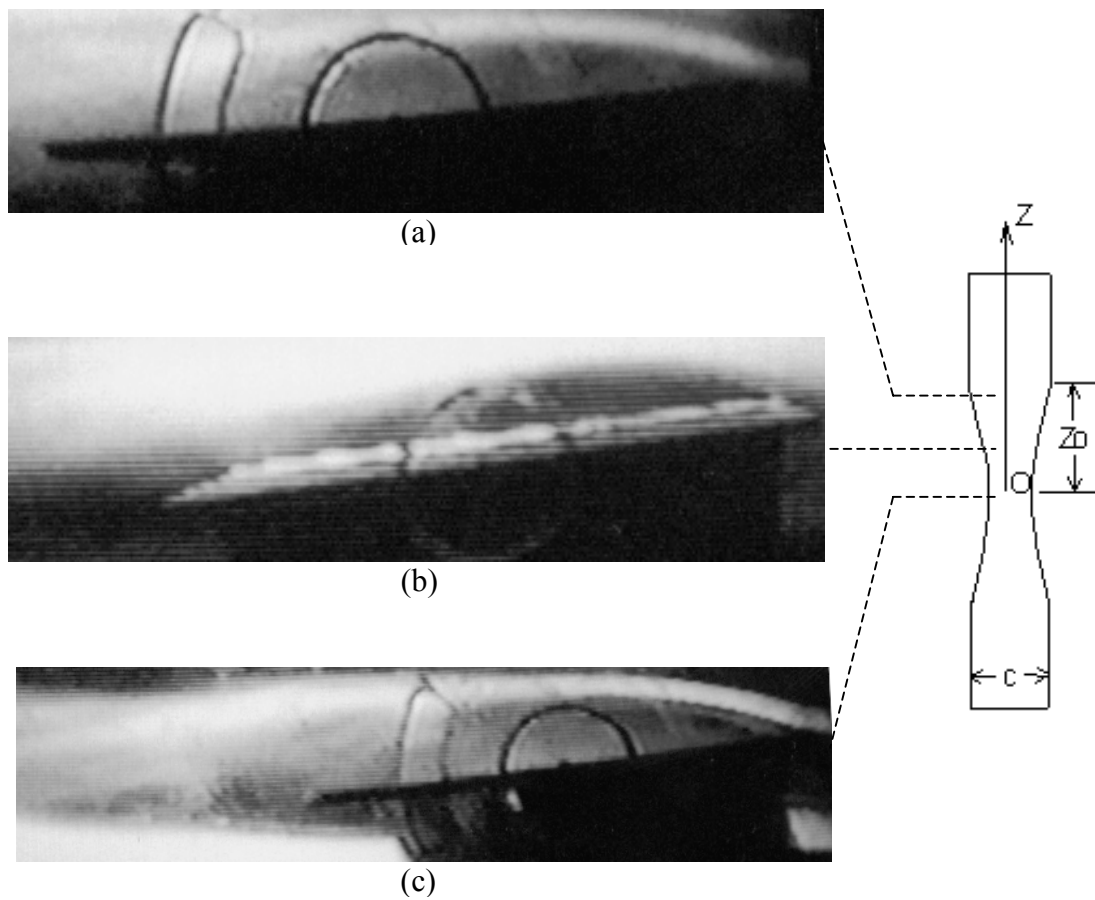
Fig 5.11 Smoke visualization of flow at three sections along plate span at $\alpha=6^0$. Separation bubble size changes at various spanwise locations. (a) $z/z_0 = 1.0$. (b) $z/z_0 = 0.5$. (c) $z/z_0 = 0.0$

Fig 5.10c presents the lift distribution from the plate with both sinusoidal leading and trailing edge (case 4). the deviation between the curves is the largest among all cases. The deviation of 3D lift from the nominal 2D results in Fig 5.10a-c serves to determine the relative contribution of the curved leading or trailing edges in development of 3D effects in the flow. In Fig 5.10d, we summarize the results from Fig 5.10a-c and include case 1 (constant chordlength plate). The maximum deviation occurs at the midspan with largest 3D effect for case 4.

A possible physical mechanism for these results could be related to the chord length variation and separation bubble effects. In general, the plate lift will be larger if there is a bubble attached on its upper surface, because the bubble effect seems to make the flow around a cambered airfoil (Tani, 1964). When the bubble bursts and no longer reattaches, a leading edge stall will occur resulting in lift reduction. This point can be used to partially explain our results combined with our smoke flow visualization at $\alpha=6^0$. Fig. 5.11 presents the flow patterns at three local sections of $z/z_0 = 1, 0.5, 0.0$ respectively for the plate with combined leading and trailing edges curved. At section $z/z_0=1$, a separation bubble clearly exists on plate upper surface extending from plate leading edge $x/c(z) = 0.0$ to a place with $x/c(z) = 0.7$. At $z/z_0=0.5$, the separation bubble covers the whole plate upper surface and extends beyond the trailing edge, a burst may happen. At plate middle span section $z/z_0=0.0$, the bubble no longer reattaches to the plate and leading edge stall occurs. These flow observations combined with Tani's viewpoint could explain the trend of the spanwise variation of lift distribution. Of

course, the effect of chord length variation also contributes to the lift variation. A larger chord length may result in larger circulation and lift. Finally it should be noted that the complex 3D flow interaction between shear layers at neighboring sections along plate span may also affect the lift distribution on final results. This is an interesting topic in the future.

The spanwise lift distribution along these curved plates for typical transitional flow ($\alpha=15^0$) is presented in Fig 5.12. In Fig 5.12(a), the deviation of the 3D lift distribution from the nominal 2D is still small, but it is larger when compared with the same case for streamlined flow (Fig 5.10(a)). From Fig 5.12(b), the curved leading edge yields much stronger 3D effect than in streamlined flow (Fig 5.10(b)). The difference between the 3D lift distribution and the nominal 2D lift increases with the reduction of chord length, and approaches its maximum value at the minimum chord length section as 62%, which is a dramatically variation compared with the same case for streamlined flow as of 26% in Fig 5.10(b). This further demonstrates the leading edge effect on 3D flow generation. Fig 5.12(c) presents the results for the plate with both sinusoidal leading and trailing edges. The difference between 3D and 2D nominal lift has the same trend as that for case 3. The maximum deviation is about 67%, showing that the combined leading and trailing edges still generate the strongest 3D effects in the flow. However, this is not a large change compared with case 3, which has a 62% deviation. Fig 5.12(d) presents the 3D lift distribution of all cases along with the 2D plate (case 1). The deviation of case 2-4 are much larger compared to case 1 than in the streamlined
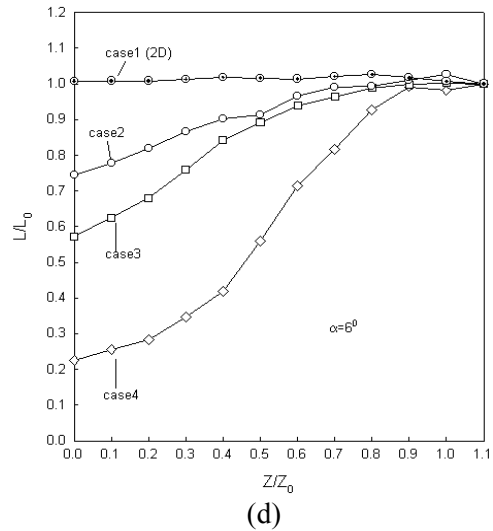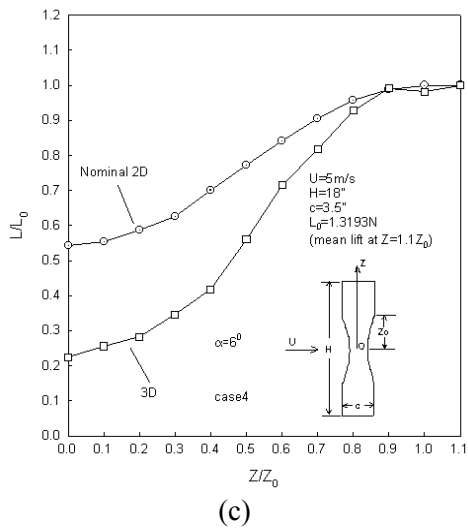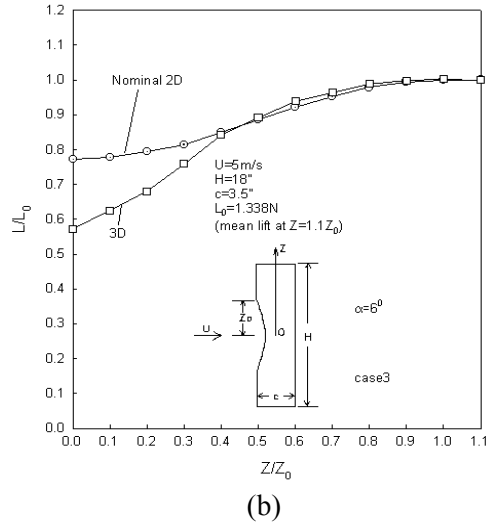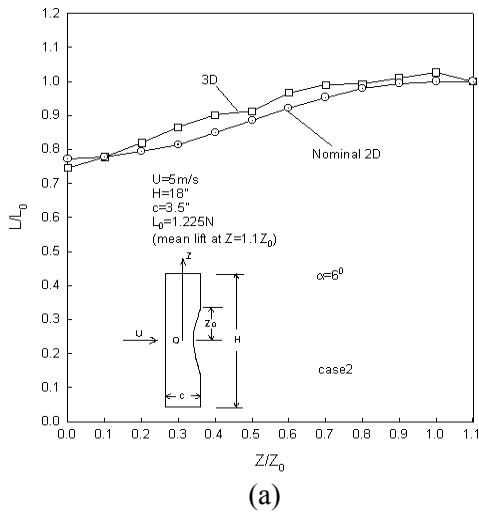
153
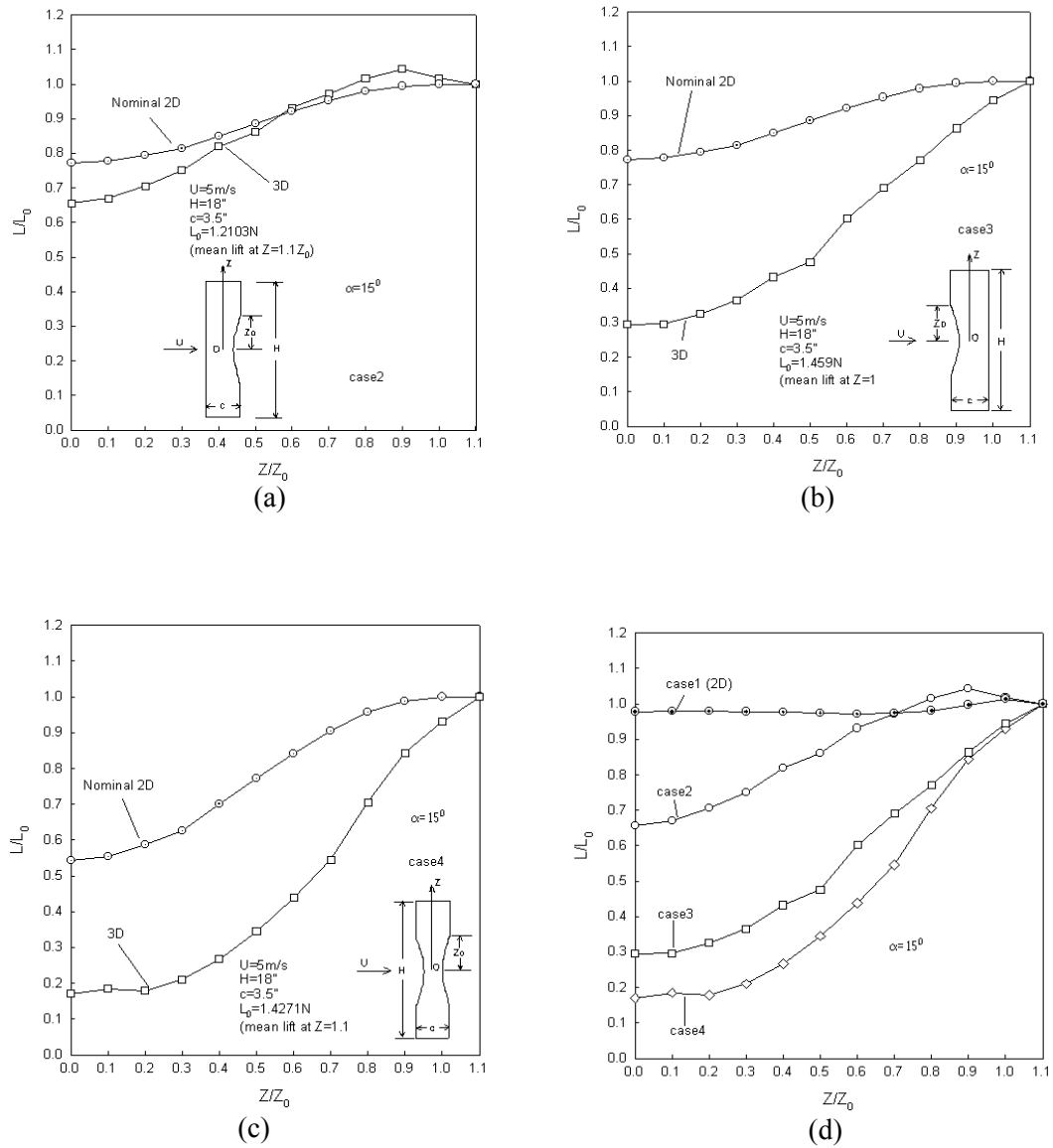
Fig 5.12 *Mean* lift distributions along plate with sinusoidal curved leading or trailing edge in a transitional flow regime ($\alpha=15^0$) at *U=5m/s.* (a) Trailing edge curved; (b) Leading edge curved; (c) Both leading and trailing edge curved; (d) Comparison of different cases.

flow case. This shows curved leading and trailing edges inducing stronger 3D effects in transitional flow than in streamlined flow. However, we reach the same conclusion as in streamlined flow, i.e., the leading edge predominates in creating 3D effects in the flow. This is further illuminated by the fact that the difference in lift distributions between case 3 and case 4 is much smaller compared with that in streamlined flow (Fig 5.10(d)). A possible physical mechanism may relate to the leading edge stall at $\alpha=15^0$ for all cases. The shear layers have separated from the plate leading edges as observed in smoke flow visualizations, hence results in smaller lift value compared to the 2D results.

5.5.2 Comparison between UCMT and force balance results

In order to further validate the UCMT measurements, we also used the force balance system in tunnel 2 to measure the total lift force on a flat plate (case 4) and compared it with the integrated lift obtained by integrating the lift distributions (in Fig. 5.10 and 5.12) across the plate span. An independent force measurement is necessary to confirm that the lift distributions measured with UCMT in section 5.5.1 are valid. The plate from case 4 (with both sinusoidal curved leading and trailing edges) was selected for the test, because it induced the strongest 3D effects on the flow as discussed previously. In previous section, our focus was mainly on the streamlined and transitional flow regimes, so in force balance measurement, the range of plate angle of attack was set from $\alpha=0^0$ to $\alpha=20^0$, which includes the streamlined, stalled and part of the transitional flow regimes. The free stream airflow speed was *U=5m/s* as in the

UCMT test. For each data point, we repeated the test for 5 times and present the *mean* value and error bars based on standard deviation. The UCMT lift distribution was integrated over plate span to give to the total *mean* lift from UCMT for comparison to the LVDT force balance measurements in tunnel 2, with following expression

$$C_L = \frac{\int_{A_0}^{A_c} C_l(z)dA}{\int_{A_0}^{A_c} dA} = \frac{\sum_{i=0}^{N}(C_{l_i} + C_{l_{i+1}})[c_i(z) + c_{i+1}(z)]}{2\sum_{i=0}^{N}[c_i(z) + c_{i+1}(z)]} \quad . \tag{5.3}$$

Where C_L is the UCMT total lift; C_l *(z)* the measured local lift coefficients; C_{l_i} the lift coefficient at each local section with chord length $c_i(z)$, setting *i=0* corresponds to the middle span of the plate and *i=N=12* represents the section with constant chord length.

An identical plate (case 4) used to determine the lift distribution (Fig 5.10c and Fig 5.12c) in tunnel 1 was now tested in tunnel 2. Since the test section dimension is slightly larger in tunnel 2 than tunnel 1, the plate did not extend to the test sectional wall in tunnel 2. Endplates (Stansby, 1974) were added to the plate in tunnel 2 to eliminate any wing tip vortex effects.

Fig 5.13 presents the comparison of lift force measured from the UCMT lift distributions and the force balance system of tunnel 2 for the case 4. The integrated lift from the UCMT lift distribution shows slightly lower values than the force balance measurements. In the streamlined flow regime at $\alpha = 6^0$, the difference is about 7%. In the transitional flow regime at $\alpha = 15^0$, the difference increases to almost 12%. The
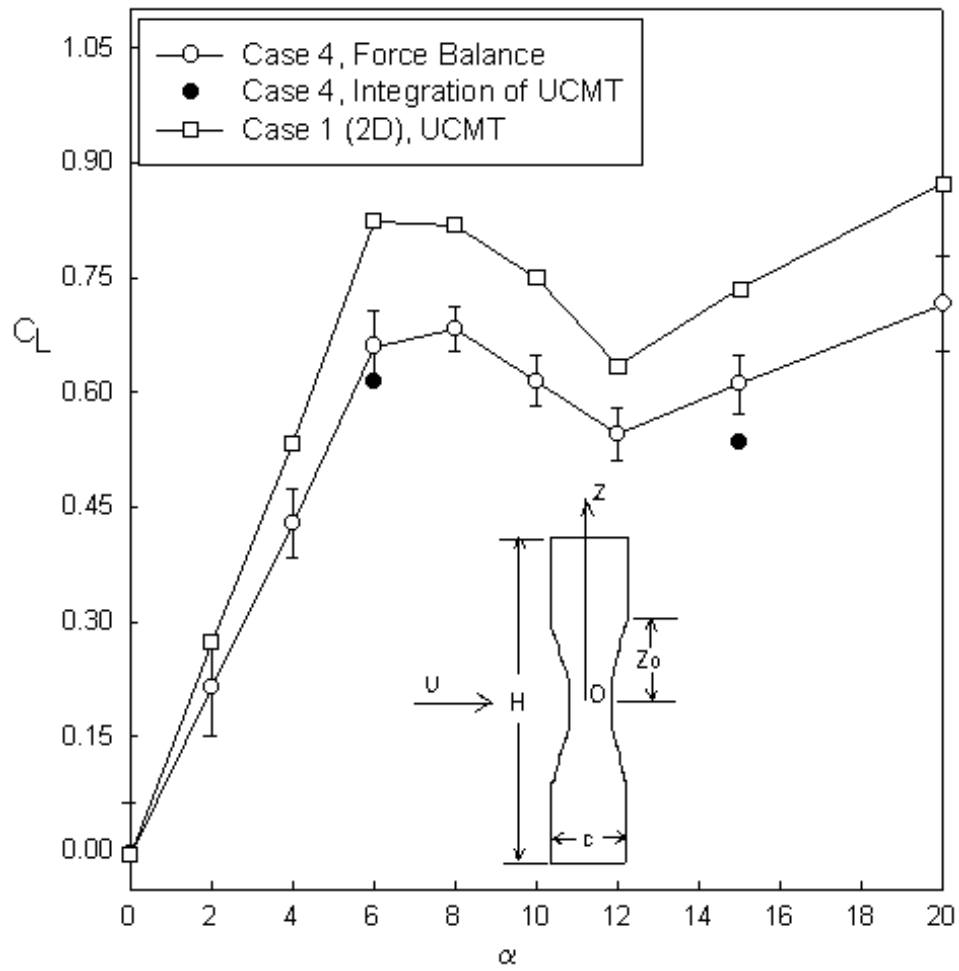
Fig 5.13 Comparison of UCMT lift measurement (in tunnel 1) and force balance measurement (in tunnel 2) at U=5m/s for a plate with both sinusoidal curved leading and trailing edge.

error may result from the discrete process when using integration and from measurement error in both the UCMT and force balance system. Another concern is that if Kutta-Joukowski theorem developed for 2D flow may yield some error in a 3D flow. Considering all these issues, the 6% deviations are still acceptable. In addition, we also present the UCMT lift for a 2D plate (Case 1) for comparison. The trend of lift variation with angle of attack is similar for case 1 (2D plate) and case 4. The difference between the lift curves for case 1 and case 4 reflects the data in Fig 5.10c and Fig. 5.12c.

5.6 Low Reynolds, low aspect ratio wing study

Given that we have developed methods in section 5.5 to study lift distributions in 3D flows, in this section, we present UCMT measurement results for low aspect ratio wings of rectangular planform shape. The wings consist of flat plate with no camber. These low AR wings may induce 3D flow naturally through the effect of wing tip vortices. The range of plate aspect ratio varied from *AR=1* to *AR=3*. For such low aspect ratios, 3D effects are expected to be strong. Given this, we recognize that in UCMT experiments, we are only measuring bound circulation related to the so-called 'linear' lift on the wing (Muller, 2001). Lift due to low-pressure regions near the wing tips created by trailing wing tip vortices is not measured with UCMT. Still, we perform UCMT experiments similar to that in section 5.5 to study the linear lift, to see if UCMT can be used to accurately predict lift on low Re, low AR wings applicable to MAV design. This isolation of the 'linear' lift from the vortex lift may also useful in low AR studies. We will discuss this in more detail later. Here, we present lift distributions measured with UCMT and determine the integrated total lift on the plates, then compare

our UCMT measurements with force balance measurement results. Our focus is again on a typical streamlined flow at $\alpha = 6^0$ and a transitional flow at $\alpha = 15^0$. Circulation values were again converted using the Kutta-Joukowski theorem, although its applicability for lift determination in highly 3D flows such as low AR wings must be verified.

Fig 5.14 presents a typical bound circulation distribution measured with UCMT along span of a low aspect ratio wing with *AR=2.0* and *Re=3.65×10⁴*. Streamlined flow ($\alpha = 6^0$) and transitional flow ($\alpha = 15^0$) cases are shown. Circulation were measured at 8 sections varying from *z/(b/2) =0.0* to *1.0*. The results shown here have processed as described in section 5.2. The uniform spanwise circulation distribution at $\alpha = 0^0$ shows negligible bound circulation as expected. The circulation distribution for $\alpha = 6^0$ and $\alpha = 15^0$ are similar. The primary characteristic is a maximum (peak) at a spanwise location near wing tip area. This deviates from the typical monotonic decreasing of lift (circulation) distributions for high AR wings through Prandtl's lift line theory (see Fig 5.15). This phenomenon may result from the strong three-dimensional flow induced near the tip vortex. It was also found by Bhagwat (2000) who measured the bound sectional circulation along the span of a wing with AR=9.6 at *Re=2.53×10⁵* using the Laser Doppler Velocimetry method (see Fig 5.2(b)). We should point out that Bhagwat (2000) was studying rotating helicopter blades where a resultant freestream velocity variation existed along the wing span. This may explain his observation of a peak in circulation along the span of fairly high aspect ration wing. As a result, direct
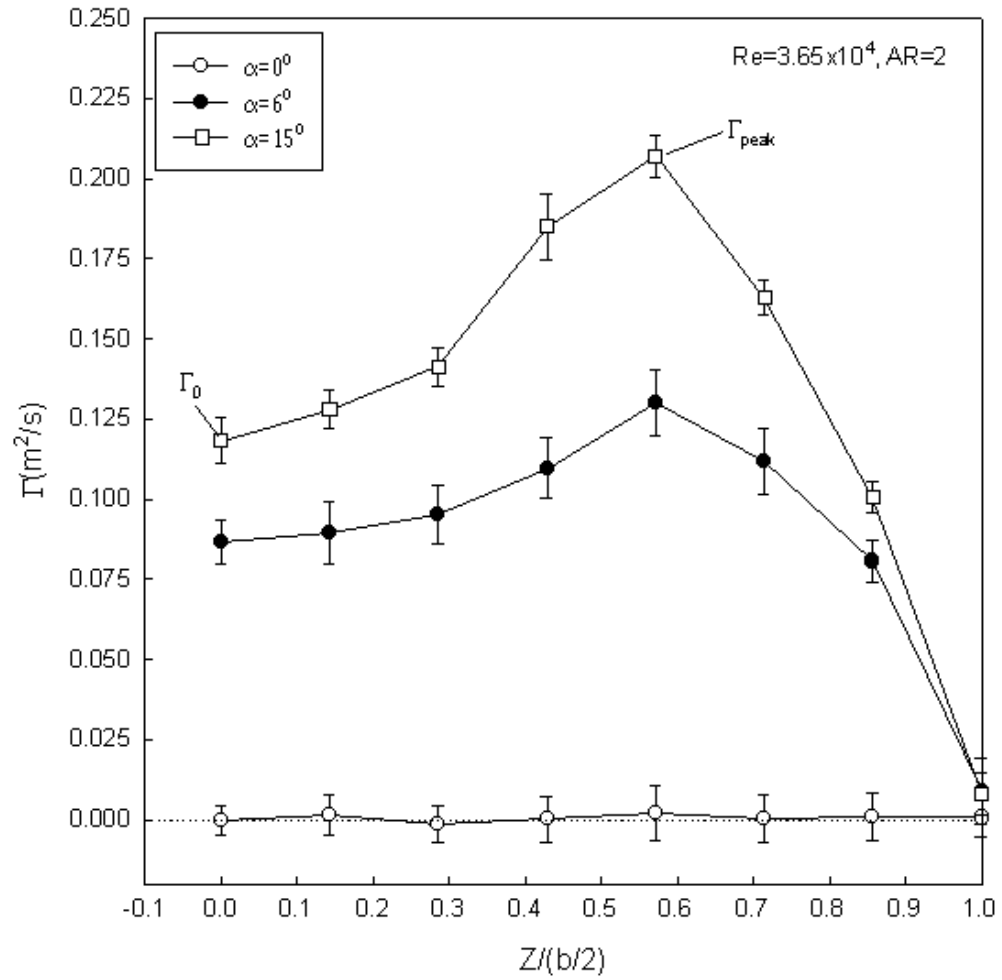
Fig 5.14 Typical circulation distributions along span of a low aspect ratio wing with AR=2 and Re=3.65×10^4, measured with UCMT in streamlined flow ($\alpha = 6^0$) and stalled flow ($\alpha = 15^0$).

comparison to our flow may not be proper. However, the existence of a circulation distribution peak in another flow is interesting. The spanwise location of the circulation peak in our work seems to be independent of AOA for $\alpha = 6^0$ and $\alpha = 15^0$. Final resolution in UCMT measurements along the span may yield some variation. However, ratio of $\Gamma_{peak}\big/\Gamma_0$ (see Fig 5.14) is larger for $\alpha = 15^0$ compared to $\alpha = 6^0$ suggesting larger induced 3D effects at higher AOA.

Fig 5.15 presents our measured lift distribution for a low aspect ratio wing (AR=2) at $\alpha = 6^0$ compared with Prandtl's lifting line theory (schlicting, 1979) for a wing with AR=6 (Prandtl's lifting line result for AR=2 is not available in literatures to the best of our knowledge). The sectional lift C_l is normalized with the mean lift of the wing C_L. The difference between the UCMT measurement and results form Prandtl's lifting line theory is dramatic. This is attributed to the strong three-dimensional effect induced by tip vortex in low aspect ratio wings. Similar results were also found by Bastedo et al (1985) (see Fig 5.2a) for a low aspect ratio wing with *AR=4* and rectangular planform and in Bhagwat (2000) (Fig 5.2b). These results indicate that Prandtl's lifting line theory is not applicable to low aspect ratio wings due to violation of the assumption of negligible flow in spanwise direction (Phillips et al, 2000).

The effect of varying aspect ratio on the lift distribution along the span of low aspect ratio wings is presented in Fig 5.16. The trends are the same for streamlined flow and transitional flow, here we only present the case for streamlined flow at $\alpha = 6^0$. We find that larger aspect ratios generally yield larger local lift across the span including the local lift value at the peak. The relative location of the peak lift value also
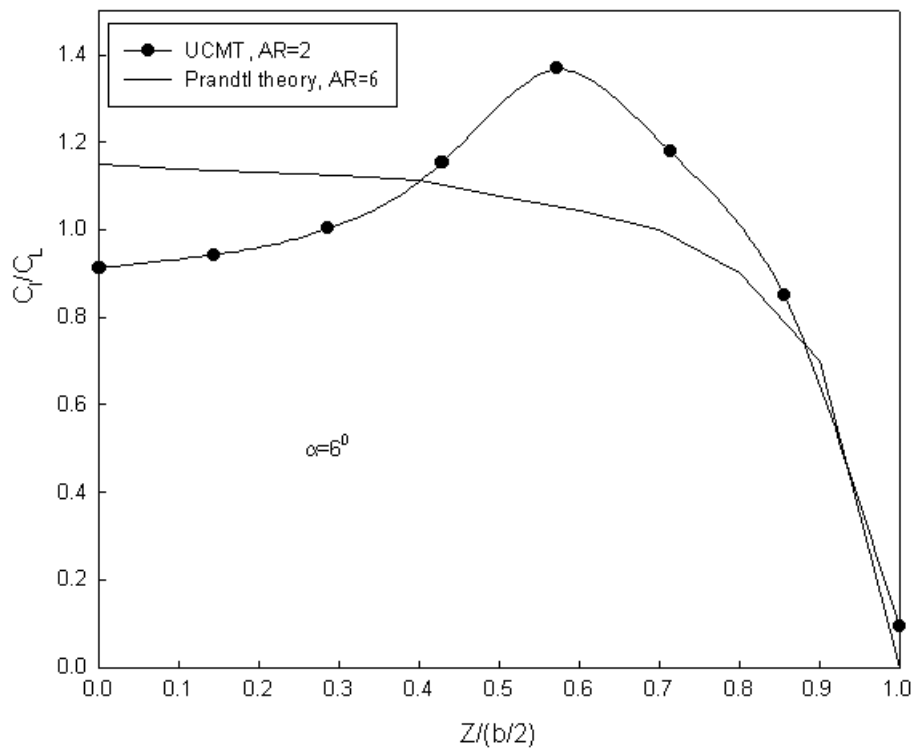
Fig 5.15 Comparison of lift distribution from UCMT along span of low aspect ratio wing (AR=2) with Prandtl's lifting line results for a wing (AR=6) (Schlichting, 1979)
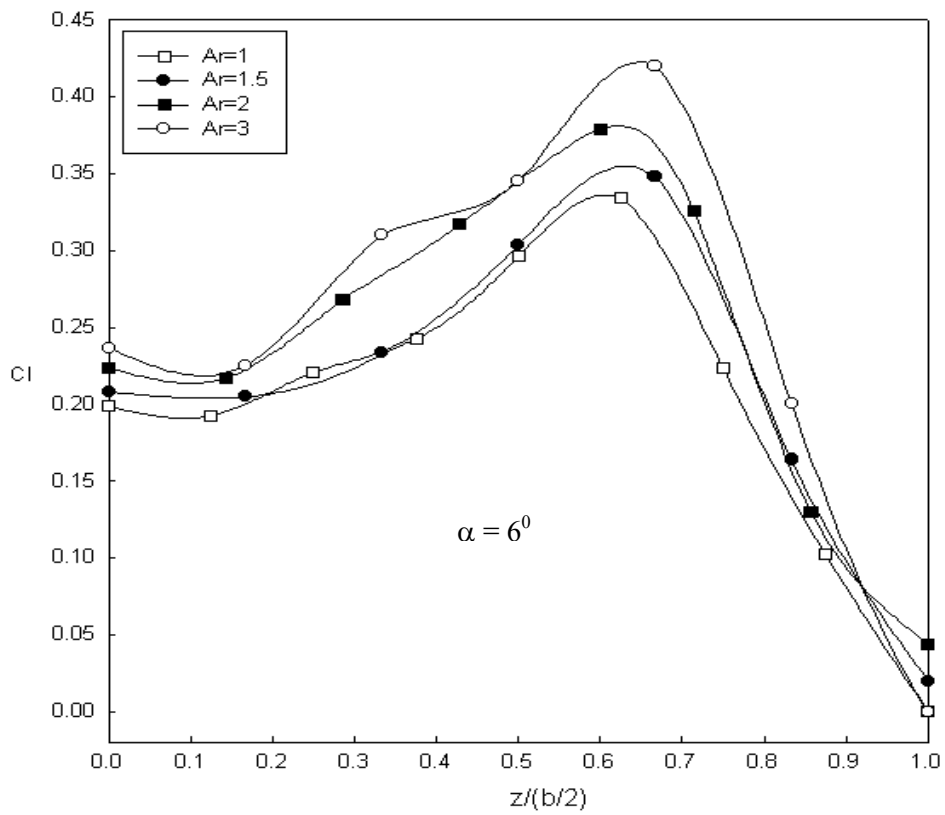
Fig 5.16 Effect of aspect ratio on lift distributions measured with UCMT on low aspect ratio wings at $\alpha = 6^0$.

varies with aspect ratio. For larger aspect ratios, the relative distance of the peak away from the wing tip decreases.

We have described the characteristics of lift distribution on low Re, low AR wings (measured with UCMT) and compared them to results from Prandtl's lifting line theory. Next, we will study the integration of the lift distributions (Fig 5.16) and compare these results with force balance measurements, results from other investigations (Pelletier & Mueller, 2000), and results from Prandtl's lifting line theory. The total lift measured with UCMT was generated from integration of sectional lift distributions (Fig 5.16) using Eq. (5.3) with N = 8. The lifting line theory result is based on

$$C_L = C_{L\alpha}\alpha$$
$$C_{L\alpha} = \frac{a_0}{[1 + (\frac{a_0 \times 57.3}{\pi Ar})(1 + \tau)]} . \tag{5.4}$$

from Anderson (1991), where $a_0 = 2\pi(\text{rad}^{-1}) = 0.1(\text{deg}^{-1})$ is the lift curve slope for two-dimensional airfoil, $C_{L\alpha}$ the lift curve slope for finite wing. τ is a parameter related to wing planform shape, where typically $0 \leq \tau \leq 0.25$, following Pelletier & Mueller (2000), we set $\tau = 0.164$ for a rectangular plate in our calculations.

We first present our lift data from UCMT measurements and our force balance measurement in Fig 5.17(a) at $\alpha = 6^0$. Each data point from balance measurement is the average of five independent runs. *Mean* value and error bars based on standard deviation are shown. The UCMT lift values are less than the force balance values, and difference between the two values increase slightly with increase of aspect ratio, with a
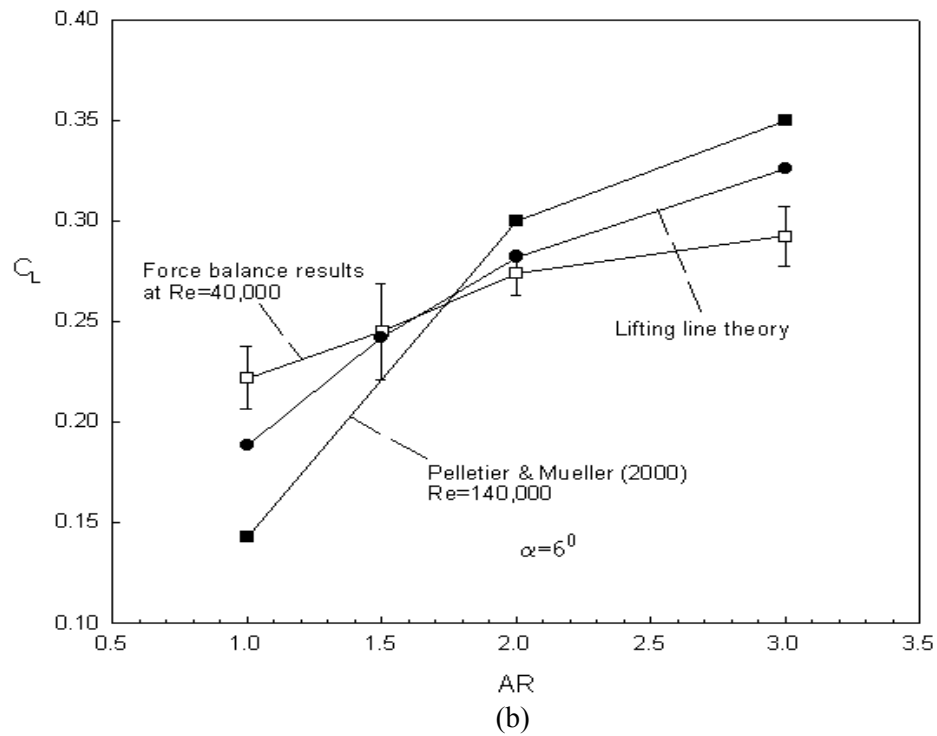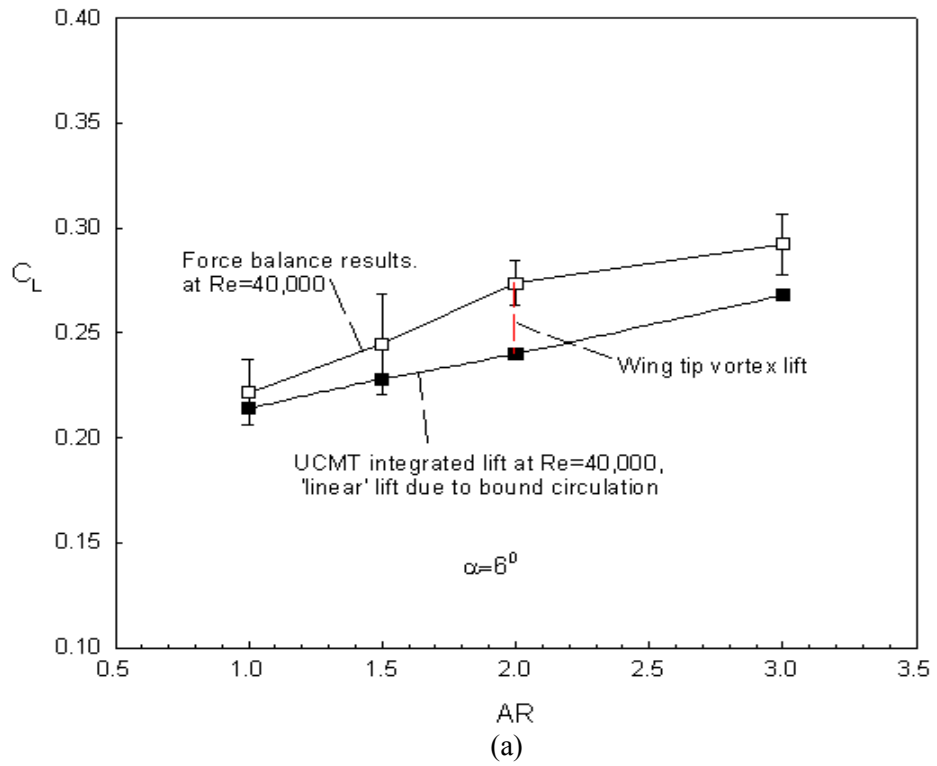
Fig 5.17 Comparison of lift coefficient vs aspect ratio in several investigations. (a) Current UCMT and force balance measurements. (b) Comparison of our force balance measurements, Pelletier & Mueler (2000)'s force balance data and finite wing theory.

maximum difference of approximate 12%. The lower lift values for the UCMT measurements seems reasonable, since the 'linear' lift due to bound circulation is accounted for in the UCMT data. The data in Fig. 5.17a suggests that integration of bound circulation from UCMT measurement can provide reasonable estimates of lift on low Re, low AR wings. The 12% difference between the curves in Fig 5.16a is acceptable at least for preliminary design work on MAVs.

In Fig 5.17(b) we compare our force balance measurements to data from Pelletier & Mueller (2000) and Prandtl's lifting line (finite wing) theory in order to check the reliability of our measurements. All these data sets show an increase in lift coefficient with increasing AR as expected. Results from Pelletier & Mueller (2000) and the present work generally bracket Prandtl's lifting line theory, however, fairly difference in lift coefficient value is observed. These differences may be attributed in part to different test conditions. For example, the Reynolds number for our test was about Re = 4×10^4, but Re = 1.4×10^5 in the work of Pelletier & Mueller (2000). Also in their work, a wing configuration with only one wingtip exposed to the flow (i.e., a half aspect ratio configuration) was used which is different from our work. The interaction between the two wingtip vortices plays an important role in low aspect ratio wings, and will certainly affect measured lift values. Unfortunately, limited lift measurements on low Re, low aspect ratio wings exists in the literature. This is an area for future work.

5.7 Summary

Two types of three-dimensional flow were studied in this chapter using UCMT and force balance techniques. First, flow over flat plate (non-uniformity) with curvedleading or/and trailing edges was studied. Next flow over low Re, low aspect ratio wing was considered. Focus was on measuring *mean* lift distributions along the span of plates leading to total integrated lift force measurement in the streamlined and transitional flow regimes.

For the flow over the curved flat plates, the measurements of lift distributions showed that leading edge effect dominates the 3D flow development. Plate with both curved leading and trailing edges induce the strongest three-dimensionality in the flow. For streamlined flows, the lift variation in span along the plates was conjectured to be related to the relative size of the separation bubble, and leading edge stall and reattachment phenomena. Smoke visualization of the flow was conducted to aid in this interpretation. Total lift data obtained by integrating the lift distributions was compared with force balance measurements. A deviation of 6% to 12% was observed and discussed.

For the low Reynolds, low aspect ratio wing study applicable to MAV design, local maximum (peaks) were observed in spanwise lift distributions measured with UCMT. This was attributed to the strong three-dimensionality in flow near wingtips. Only the bound circulation, or 'linear' lift effect is accounted for in UCMT measurements. The UCMT technique therefore can serve as a way to isolate the 'linear' lift effect verse the lift induced by wingtip vortices. This may prove useful in future

studies of low AR wings. The relative location and value of the peak lift varies with aspect ratio. Comparison between total integrated lift from UCMT lift distributions and force balance measurements showed that UCMT measurements under-predicted lift slightly as expected since only the 'linear' lift is measured. The qualitative trends from these different measurements were the same, with larger aspect ratios leading to larger lift coefficients.

In calculating *mean* lift forces from UCMT measurements, the Kutta-Joukowski theorem was used to convert circulation to lift. This may contribute some error in lift determination since the Kutta-Jouskowski theorem is valid principally for two-dimensional flows. However, we have found that UCMT techniques can provide reasonable measured lift distributions and integrated lift values as long as the imposed three-dimensionality is not too large. Another concern is whether Prandtl's lifting line theory is applicable to low aspect wings because its assumption of negligible flow in spanwise direction may not hold near the wing tip region. Future investigations are still needed to further understand these issues.

Chapter 6

Conclusions

6.1 Summary of Results

Lift force determination is a key issue in many engineering applications, especially in understanding nonlinear coupling between structural motions and flow dynamics in fluid-structure interaction problems. However, deficiencies exist in past experimental techniques available to measure lift forces, particularly in areas of unsteady instantaneous lift measurement, and measurement of spatial lift distributions variation of sectional forces along structural spans.

The major goal in our work is to explore a method that can be used in future experiments to address the above issues. The developed ultrasonic circulation measurement technique (UCMT) has shown potential for addressing those issues. UCMT was developed for lift determination based on the quasi-steady K-J theorem that properly converts the circulation to lift for steady flow. Hence, it has been mainly used in the past for *mean* lift measurement in two-dimensional steady flows around various aerodynamic bodies, including airfoils and delta wings. The extension of the UCMT methods to measure time-varying lift forces in unsteady flows has remained largely unstudied, and UCMT methods have also not been applied to measure lift distributions along structural spans. The focus of this research is to study extension of UCMT for lift determination in unsteady and three-dimensional flows.

We used a combined analytical-numerical-experimental approach to fulfill this major goal. We first developed analytical methods that can properly convert time-

dependent circulation (measurable with UCMT) to instantaneous lift forces based on unsteady potential flow theory. Then we verified the developed correction method numerically with a finite element solution. Finally, we experimentally used UCMT to study lift distributions along spans of structures that can induce three-dimensional flows.

The corrected method was developed based on the work of Katz & Plotkin (1991), who deduced a general expression to relate unsteady circulation to instantaneous lift for an unsteady flow around a thin plate.

$$L(t) = \underbrace{\rho U(u)\Gamma(t)}_{A} + \underbrace{\rho\int_0^c \frac{\partial}{\partial t}\Gamma(x,t)dx}_{B}. \tag{2.3}$$

In real experiments, $\Gamma(x,t)$ is very difficult to measure using UCMT. However, the bound circulation $\Gamma(t)$ is attainable. Hence, we developed a corrected unsteady method that can properly convert measurable unsteady bound circulation to instantaneous lift through

$$\boxed{L(t) = \underbrace{\rho U(u)\Gamma(t)}_{A} + \underbrace{R\rho c \frac{d\Gamma(t)}{dt}}_{B}.} \tag{2.36}$$

Here R is defined as an unsteady lift correction factor. The value of R was determined for several unsteady flow cases; $R=3/4$ for an oscillating plate; $R=0$ for a plunging plate; $R=1$ for an impulsively started plate. For a pitching plate, R is a complicated function of plate oscillation frequency, pivot location and freestream velocity. These results are valid for low amplitude, low frequency motions of thin airfoils. For flow around a stationary circular cylinder at Re=100, $R=0.4$ was determined empirically

from finite element solutions. Our corrected unsteady method expands the capability of the UCMT technique for unsteady flow studies may have application in other experimental methods that can acquire bound circulation such as the PIV techniques.

Our corrected unsteady method was validated numerically using a finite element solution for flow around an oscillating flat plate at low angle of attack and at Re=100. Time-dependent bound circulation, based on the instantaneous velocity field integration along a mimicked closed sound path, was converted to instantaneous lift force using our developed methods. These results were compared to the 'true' lift forces (from stress integration). It was shown that our unsteady correction method provided improved results compared to the quasi-steady K-J approximation for unsteady flow studies.

Another important issue was the effect of variation in the acoustic path on bound circulation determination, which has not been addressed in previous UCMT studies. We systematically studied this issue with numerical finite element solutions and found that proper selection of the enclosing acoustic path is critical for accurate lift measurements. The information obtained in this work will be useful for closed path design in future UCMT, PIV or LDV experiments.

Having achieved a better understanding of lift determination in unsteady plate flows, we next studied another important flow, low Reynolds number vortex shedding from a stationary bluff body (circular cylinder) using similar methods. We study various force models including a quasi-steady K-J method, an approximate Lighthill's vortex force model, and a new unsteady model similar to that developed for plate flows. Finite element simulations for flow over a circular cylinder at Re = 100 were once again

performed. Various combinations of force models were studied. An approximate vortex force model based on an UCMT concept yielded lift predictions differing from the true lift values. As a result, an alternative model similar to that developed for unsteady flat plate flows was proposed and studied. This model requires measurement of instantaneous bound circulation in a region enclosing the cylinder. Some of our results also will have future impacts on PIV and LDV studies where flow data is integrated over regions enclosing aerodynamics bodies.

To expand the capability of the UCMT technique for three-dimensional flow studies, we experimentally studied the *mean* lift distribution along structures that can induce three-dimensional flows. Flow around plates with sinusoidal curved leading or/and trailing edges and low Reynolds, low aspect ratio wings applicable to micro-aerial-vehicle (MAV) design were studied. The size of the local chord length, size of separation bubbles and leading edge stall and reattachment phenomena were suggested to understand the results on the curved plates. Investigation of the lift distribution on the curved plates, and comparison to force balance results validated the UCMT methods used.

Study of low Reynolds low aspect ratio wings with the UCMT technique showed that spanwise lift distributions are dramatically different from those obtained from Prandtl's lifting line theory. UCMT measured results showed that a peak circulation (lift) value exists at a location near the wing tip. The UCMT measurements only measure the bound circulation (e.g. 'linear' lift). Lift due to low pressure region created by wing tip vortices are not included. However, integration of the spanwise lift

distributions yielded reasonable (but lower) total lift values compared to independent force balance measurements.

Based on the deviation between lift values from integrated lift distribution and force balance measurements, some concern still exist concerning the applicability of the K-J theorem in the MAV studies. Our results suggest that the K-J theorem is valid as long as the three-dimensionality in the flow is small (curved plates), but care must be taken with highly three-dimensional flows such as low Reynolds, low aspect ratio wings.

6.2 Future Work

Future research in this area would first concentrate on applying what has been learned in the present study to experimental UCMT studies on unsteady flows. From the present work, we have not only learned how to properly convert measured unsteady circulation values to instantaneous lift, but also gained insight into a wide variety of unsteady flows. These results are valid for low amplitude, low frequency motions of flat plate airfoils. We have learned that plunging plates and impulsively started plates are the best candidate flows for UCMT experiments. Plunging plates, for example, require no-unsteady correction (R=0), and the quasi-steady K-J theorem is applicable. Pitching airfoils, on the other hand, require complex unsteady corrections ($R = f(k, a/c, U, t)$) and may be more difficult to study. Systematic determination of R values for other unsteady flows will be of interest in future work.

We have also gained insight into the dependence of lift measurements on the geometry of acoustic path. As a result, we now can design proper acoustic path in experiments on unsteady flows and low Re cylinder wakes and possibly re-interpret previous UCMT results. In future, we would like to systematically study variation of the allowed region for path selection as a function of Reynolds number, body oscillation amplitude and reduced frequency, so that the results become a true resource for guidance of circulation measurement experiments such as UCMT, PIV and LDV. We also foresee studying combinations of K-J theorem, unsteady correction and vortex flow models in UCMT experiments on cylinder wakes.

In three-dimensional flows, we plan to focus on low Reynolds, low aspect ratio wings for MAV studies. We would like to better understand the observed circulation distribution peaks, while also measuring trailing wing tip vortex strength (circulation) using UCMT. All parameters may depend on the wing tip chord-length, freestream velocity, angle of attack, and airfoil span at extreme low aspect ratios.

On the numerical side, we would like to repeat the simulation of chapter 3 and 4 at higher Reynolds numbers. Simulations on oscillating plates at Re=10^3, 10^4 would confirm our unsteady correction methods at Reynolds numbers of many engineering applications. Simulations on a pitching flat plate could also be conducted to verify and better understand the complex unsteady correction factor R in this flow. The application of the cylinder wake work to data from numerical simulation of freely vibrating cables (NEKTAR code of G. Karniadakis) is also a possibility.

For analytical studies, confirming the empirically determined corrected factor, R=0.4 for cylinder flow, remains as a challenge. In the development of our correction method, higher order time derivatives of bound circulation were not included in Eq. (2.36), which only expressed the quasi-steady and one unsteady term. Those high order terms may improve our results for body oscillations with higher frequency and amplitude. The methods of chapter 2 could also be extended to develop unsteady corrections for pitching moments in unsteady aerodynamic flows.

Appendix A

Derivation of Unsteady Correction Factor, R

(1) General plate motion

The unsteady correction coefficient is defined in chapter 2 as

$$R = \frac{B}{B^{(2)}} .$$

(2.35)

$$B = \rho \int_0^c \frac{\partial}{\partial t} \Gamma(x,t) dx .$$

(A.1)

$$B^{(2)} = \rho \int_0^c \frac{\partial}{\partial t} \Gamma(t) dx .$$

(A.2)

The integrated circulation $\Gamma(x,t)$ is expressed as

$$\Gamma(x,t) = \int_0^x \gamma(s,t) ds .$$

(2.4)

Based on the classic approach of Glauert and with a standard transform $x = \frac{c}{2}(1 - \cos\theta)$, $\gamma(s,t)$ can be expressed as a chordwise trigonometric expansion at any time instant as

$$\gamma(\theta,t) = 2U(t)[E_o(t)\frac{1+\cos\theta}{\sin\theta} + \sum_{n=1}^{\infty} E_n(t)\sin(n\theta)].$$

(2.5)

Hence, the derivative of $\Gamma(x,t)$ will be

$$\frac{\partial}{\partial t}\Gamma(x,t) = \frac{\partial}{\partial t}\int_0^x \gamma(s,t)ds = \frac{\partial}{\partial t}\int_0^\theta \gamma(\theta_0,t)\frac{c}{2}\sin\theta_0 d\theta_0$$

$$= \frac{\partial}{\partial t}\left\{2U(t)\int_0^\theta [E_o(t)\frac{1+\cos\theta_0}{\sin\theta_0} + \sum_{n=1}^{\infty} E_n(t)\sin(n\theta_0)]\frac{c}{2}\sin\theta_0 d\theta_0\right\}$$

$$= \frac{\partial}{\partial t}\left\{cU(t)[\int_0^\theta E_o(t)(1+\cos\theta_0)d\theta_0 + \sum_{n=1}^{\infty}\int_0^\theta E_n(t)\sin(n\theta_0)\sin(\theta_0)d\theta_0\right\}$$

(A.3)

With the aid of following integrals

$$\int_0^\theta \sin^2 \theta_0 d\theta_0 = \frac{\theta}{2} - \frac{\sin 2\theta}{4} . \tag{A.4}$$

$$\int_0^\theta \sin(n\theta_0)\sin(\theta_0)d\theta_0 = \frac{\sin(n-1)\theta}{2(n-1)} - \frac{\sin(n+1)\theta}{2(n+1)} . \tag{A.5}$$

and considering $U(t)=U=$constant in our work, (A.3) will be

$$\frac{\partial}{\partial t}\Gamma(x,t) = cU\frac{\partial}{\partial t}\left\{ E_0(t)(\theta + \sin\theta) + E_1(t)(\frac{\theta}{2} - \frac{\sin 2\theta}{4}) \right.$$
$$\left. + \sum_{n=2}^{\infty} E_n(t)[\frac{\sin(n-1)\theta}{2(n-1)} - \frac{\sin(n+1)\theta}{2(n+1)}] \right\} \tag{A.6}$$

For bound circulation $\Gamma(t) = \Gamma(c,t) \Rightarrow x = c \Rightarrow \theta = \pi$, substitute into (A.6), yields

$$\frac{\partial}{\partial t}\Gamma(t) = \pi cU\frac{\partial}{\partial t}[E_0(t) + \frac{E_1(t)}{2}]. \tag{A.7}$$

Substitute (A.6) into (A.1), yields

$$B = \rho\int_0^c \frac{\partial}{\partial t}\Gamma(x,t)dx = \rho\int_0^\pi cU\frac{\partial}{\partial t}\left\{ E_0(t)(\theta + \sin\theta) + E_1(t)(\frac{\theta}{2} - \frac{\sin 2\theta}{4}) + \right.$$
$$\sum_{n=2}^{\infty} E_n(t)[\frac{\sin(n-1)\theta}{2(n-1)} - \frac{\sin(n+1)\theta}{2(n+1)}] \left.\right\}\frac{c}{2}\sin\theta d\theta \tag{A.8}$$
$$= \frac{1}{4}\rho c^2 U\pi\frac{\partial}{\partial t}[3E_0(t) + E_1(t) + \frac{1}{2}E_2(t)]$$

Substitute (A.7) into (A.2), yields

$$B^{(2)} = \rho\int_0^c \frac{\partial}{\partial t}\Gamma(t)dx = \rho\int_0^\pi \pi cU\frac{\partial}{\partial t}[E_0(t) + \frac{E_1(t)}{2}]\frac{c}{2}\sin\theta d\theta$$
$$= \rho c^2 U\pi\frac{\partial}{\partial t}[E_0(t) + \frac{E_1(t)}{2}] \tag{A.9}$$

Substitute (A.8), (A.9) into (2.35), yields

$$R = \frac{B}{B^{(2)}} = \frac{3}{4} \frac{\frac{\partial}{\partial t}[E_0(t) + \frac{1}{3}E_1(t) + \frac{1}{6}E_2(t)]}{\frac{\partial}{\partial t}[E_0(t) + \frac{E_1(t)}{2}]} .$$ (A.10)

From eq. (2.7), it gives

$$\left. \begin{array}{l} E_o(t) = -\frac{1}{\pi}\int_0^\pi \frac{W(x,t)}{U(t)}d\theta, \\[2mm] E_1(t) = \frac{2}{\pi}\int_0^\pi \frac{W(x,t)}{U(t)}\cos(\theta)d\theta \\[2mm] E_2(t) = \frac{2}{\pi}\int_0^\pi \frac{W(x,t)}{U(t)}\cos(2\theta)d\theta \end{array} \right\} .$$ (A.11)

Local downwash is given in eq. (2.8) as

$$W(x,t) = U\frac{\partial \eta}{\partial x} - \frac{\partial \Phi_W}{\partial z} + \frac{\partial \eta}{\partial t} .$$ (2.8)

For the motion studied in this work, plate shape function is given in eq. (2.10)

$$\eta(t) = h(t) - \alpha(t)(x - a) .$$ (2.10)

Substitute (2.10) into (2.8), yields

$$\frac{\partial \eta}{\partial x} = -\alpha(t), \quad \frac{\partial \eta}{\partial t} = \dot{h}(t) - \dot{\alpha}(t)(x - a) .$$ (A.12)

Substitute (A.12) in (2.8), yields

$$W(x,t) = -U\alpha(t) + \dot{h}(t) - \dot{\alpha}(t)(x - a) - \frac{\partial \Phi_W}{\partial t} .$$ (A.13)

The wake potential Φ_W is a complex function of the plate motion history. From the work

of Theodorsen (1935) and Von Karman & Sears(1938), effect of Φ_W can be corrected by

using a lift deficiency factor *C(k)* (see Appendix B) to the quasi-steady term. Hence, here

it can be temporarily neglected. (A.13) will be

178

$$W(x,t) = -U\alpha(t) + \dot{h}(t) - \dot{\alpha}(t)(x-a).\tag{A.14}$$

Substitute (A.14) in (A.11), and notice $x = \dfrac{c}{2}(1-\cos\theta)$, yields

$$\left.\begin{aligned}E_o(t) &= \frac{1}{U}[U\alpha(t) - \dot{h}(t) + \frac{c}{2}\dot{\alpha}(1-\frac{2a}{c})],\\[2mm] E_1(t) &= \frac{c\dot{\alpha}}{2U},\\[2mm] E_2(t) &= 0\end{aligned}\right\}.\tag{A.15}$$

Substitute (A.15) in (A.10), yields

$$\boxed{R = \frac{B}{B^{(2)}} = \frac{3}{4}\frac{U\dot{\alpha} - \ddot{h} + (\frac{2c}{3} - a)\ddot{\alpha}}{U\dot{\alpha} - \ddot{h} + (\frac{3c}{4} - a)\ddot{\alpha}}}.\tag{A.16}$$

(2) Application to typical unsteady flows

(2.1) Oscillating plate

For an oscillating plate, eq. (2.13) gives

$$\alpha = \text{constant}; \qquad h = h_0 + h_a \sin(\omega t)\;.\tag{2.13}$$

Substitute it in (A.16), yields

$$\boxed{R = \frac{B}{B^{(2)}} = \frac{3}{4}}.\tag{2.17}$$

(2.2) Plunging plate

For a plunging plate, its motion is given by eq. (2.38)

$$\left.\begin{array}{l} \alpha = const. \\ h(t) = h_0 - (\dfrac{h_0 - h_1}{t_c})t, 0 \le t < t_c \\ h(t) = h_1, \quad t \ge t_c \end{array}\right\} \ .$$

(2.38)

yields $\dot{\alpha} = \ddot{\alpha} = 0, \ddot{h} = 0$, substitute in (A.16), get

$$\boxed{R=0}.$$

(2.39)

(2.3) Pitching plate

For a pitching plate, the plate motion is given as

$$\alpha = \alpha_o + \alpha_a \sin(\omega t); \qquad h = h_0 = cons\tan t \ .$$

(2.40)

yields

$$\ddot{h} = 0, \dot{\alpha} = \omega \alpha_a \cos(\omega t), \ddot{\alpha} = -\omega^2 \alpha_a \sin(\omega t) \ .$$

(A.17)

Substitute (A.17) in (A.16), yields

$$R = \frac{B}{B^{(2)}} = \frac{3}{4} \frac{U \cos(\omega t) - (\frac{2c}{3} - a)\omega \sin(\omega t)}{U \cos(\omega t) - (\frac{3c}{4} - a)\omega \sin(\omega t)} \ .$$

(A.18)

Substitute $\omega = \dfrac{2Uk}{c}$ in (A.18), yields

$$\boxed{R = \frac{B}{B^{(2)}} = \frac{3}{4} \frac{\cos(\frac{2Uk}{c}t) - 2(\frac{2}{3} - \frac{a}{c})k \sin(\frac{2Uk}{c}t)}{\cos(\frac{2Uk}{c}t) - 2(\frac{3}{4} - \frac{a}{c})k \sin(\frac{2Uk}{c}t)}}.$$

(A.19)

Appendix B

Lift Deficiency Factor, *C(k)*

Lift deficiency factor is also called Theodorsen's function (Fung, 1993), it is used to correct the lift obtained from a mathematical manipulation in which the wake effect is temporarily neglected due to the complex mathematical difficulty. It is a function of reduced frequency and it's exact expression is

$$C'(k) = F(k) + iG(k) = \frac{K_1(ik)}{K_0(ik) + K_1(ik)}. \tag{B.1}$$

Where *K(ik)* are modified Bessel functions. Obviously (B.1) is a complex mathematical expression. An approximate expression of *C(k)* can be expressed as

$$C'(k) \doteq \begin{cases} 1 - \dfrac{0.165}{1 - \dfrac{0.0455}{k}i} - \dfrac{0.335}{1 - \dfrac{0.3}{k}i} & ; k \le 0.5 \\[4mm] 1 - \dfrac{0.165}{1 - \dfrac{0.041}{k}i} - \dfrac{0.335}{1 - \dfrac{0.32}{k}i} & ; k \ge 0.5 \end{cases}. \tag{B.2}$$

After some mathematical manipulation, its module can be expressed as

$$C(k) = \begin{cases} \sqrt{\left(1 - \dfrac{0.165}{(1 + \frac{0.0455}{k})^2} - \dfrac{0.335}{(1 + \frac{0.3}{k})^2}\right)^2 + \left(\dfrac{\frac{0.0075}{k}}{(1 + \frac{0.0455}{k})^2} + \dfrac{\frac{0.1005}{k}}{(1 + \frac{0.3}{k})^2}\right)^2} & ; k \le 0.5 \\[6mm] \sqrt{\left(1 - \dfrac{0.165}{(1 + \frac{0.041}{k})^2} - \dfrac{0.335}{(1 + \frac{0.32}{k})^2}\right)^2 + \left(\dfrac{\frac{0.0068}{k}}{(1 + \frac{0.041}{k})^2} + \dfrac{\frac{0.1072}{k}}{(1 + \frac{0.32}{k})^2}\right)^2} & ; k \ge 0.5 \end{cases}. \tag{B.3}$$

(B.3) was used in our work in chapter 2 (equation (2.12)).

References

Anderson, D. (1991), <u>Fundamental of Aerodynamics</u>, 2nd ed., McGraw-Hill, New York, 343.

Anderson, D. (1997), <u>A History of Aerodynamics and Its Impact on Flying Machines</u>, Cambridge Aerospace Series 8, Cambridge University Press, London, England.

Bastedo, et al (1985), "Performance of finite wings at low Reynolds numbers", Proceeding of the Conference on Low Reynolds Number Airfoil Aerodynamics, edited by Muller, T.J, University of Notre Dame, Notre Dame, IN, 195-205.

Bearman, P.W.(1984), "Vortex shedding from oscillating bluff bodies", Ann. Rev. Fluid Mech., **16**, 195-222.

Bearman, P.W., Graham, J.M.R., & Obasaju, E.D. (1984) A model equation for the transverse forces on cylinders in oscillatory flows. Appl. Ocean Res. **6**, 166-172

Bearman, P.W. & Luo, S.C. (1988), " Investigation of the aerodynamic instability of a square-section cylinder by forced oscillation", Journal of Fluids and Structures, **2**, 161-176.

Bhagwat, M.J. & Leishman, J.G. (2000), "Measurement of bound and wake circulation on a helicopter rotor", Journal of Aircraft, **37 (2),** 227-234.

Blevins, R.D. (1984), <u>Flow-induced Vibrations</u>, New York, Van Nortranl Reinhold.

Blevins, R.D. (1988), <u>Applied Fluid Dynamics Handbook</u>, New York, Von Nortranl Reinhold, 322.

Cetiner, O. & Rockwell, D. (2001), " Streamwise oscillation of a cylinder in a steady current. Part 1. Locked-on states of vortex formation and loading", Journal of Fluid Mechanics, **427**, 1-28.

Cetiner, O. & Rockwell, D. (2001), " Streamwise oscillation of a cylinder in a steady current. Part 2. Free-surface effects on vortex formation and loading", Journal of Fluid Mechanics, **427**, 29-59.

Desabrais, K.J. and Johari, H. (1998), "Direct Circulation Measurement of a Wing Tip Vortex Using Ultrasound", AIAA paper 98-0609.

Fung, Y. C. (1993), <u>An Introduction to the Theory of Aeroelasticity</u>, Dover Publication Inc., New York.

Gad-el-Hak, M. (2001), "Micro-Air-Vehicles: Can they be controlled better?" Journal of Aircraft, **38(3),** 419-429.

Giacomelli, R. & Pistolesi, E. (1934), <u>Historical Sketch In Aerodynamic Theor</u>, Vol.1, ed. Durand, W.F. Berlin, Springer.

Glauert, H. (1959), <u>The Elements of Aerofoil and Airscrew Theory</u>, 2nd ed., Cambridge University Press.

Govardhan, R. & Williamson, C.H.K. (2000), " Modes of vortex formation and frequency response of a freely vibrating cylinder", Journal of Fluid Mechanics, **420**, 85-130.

Helmholtz, H. L. (1858), "On the integrals of the hydrodynamic equations corresponding to vortex motions", Crelles Journal fur die reine und angewandte Mathematik, **60,** 23-55.

Hover, F. S., Techet, A. H. & Triantafyllou, M. S. (1998), "Forces on oscillating uniform and tapered cylinder in crossflow", Journal of Fluid Mechanics, **363**, 97-114.

Ikeda, S. & Yamamoto, Y. (1981), "Lift force on cylinders in oscillating flows", Report of Department Foundation of Engineering and Coastal Engineering, Saitama University, Japan, **10**, 1-16.

Iwan, W.D. (1975), "The vortex induced oscillation of elastic structural elements", Journal of Engineering for Industry, Transaction of ASME, 1378-1382.

Johari, H. & Durgin, W. W. (1998), " Direct measurement of circulation using ultrasound", Experiments in Fluids, **25**, 1-10.

Joukowski, N.E., 1906, "Sur les Tourbillons Adjionts", Traraux la Section Physique de la Societe Imperiale des Science Naturales, Vol.13, No. 2.

Kutta, M.W., 1902, "Auftriebskrafte in Stromenden Flussigkeiten", Illustrierte Aeronautische Mitteilungenm Vol. 6, p133.

Katz, J. & Plotkin, A. (1991), <u>Low-speed Aerodynamics, from wing theory to panel methods</u>, McGraw-Hill series in Aeronautical and Aerospace Engineering, McGraw-Hill, Inc.

Lancaster, F.W. (1926), "Sustentation in flight", Journal of Royal Aeronautical Society, **30,** 587-606.

Lasheras, J.C. & Meiburg, E. (1990), "Three-dimensional vorticity modes in the wake of a flat plate", Phys. Fluids A, **2**, 371-379.

Lighthill, J. (1986), " Fundamentals concerning wave loading on offshore structures", Journal of Fluid Mechanics, **173**, 667-681.

Lin, J.-C. & Rockwell, D. (1996), " Force identification by vorticity fields: Techniques based on flow imaging", Journal of Fluids and Structures, **10**, 663-668.

Lin, J.-C. & Rockwell, D. (1997), " Quantitative interpretation of vortices from a cylinder oscillating in quiescent fluid", Exps. Fluids, **23**, 99-104.

Lin, J-C & Rockwell, D. (1999), " Horizontal oscillations of a cylinder beneath a free surface: Vortex formation and loading", Journal of Fluid Mechanics, **389**, 1-26.

Linn, A. (1999), Determination of Average Lift of a Rapidly Pitching Airfoil, M. S. Thesis, Worcester Polytechnic Institute.

Lohner, R. et al (1984), "The solution of non-linear hyperbolic equation systems by the finite element method", International Journal of Numerical Methods in Fluids, **4**, 1043-1052.

Malamataris, N.G. (1991), Computer-aided analysis of flows on moving and unbounded domains: Phase-chage fronts and liquid leveling, PhD thesis, The University of Michigan.

Maull, D.J. & Milliner, M.C. (1978), "Sinusoidal flow past a circular cylinder", Coastal Engineering, **2**, 149-168.

Meiburg, E. & Lasheras, J.C. (1988), "Experimental and numerical investigation of the three-dimensional transition in plane wakes", Journal of Fluid Mechanics, **190**, 1-37.

Moreira, J. & Johari, H. (1997), "Direct measurement of delta wing vortex circulation using ultrasound", AIAA paper 97-0743.

Newman, D. & Karniadakis G. E. (1996), "Simulations of flow over a flexible cable: A comparison of forced and flow-induced vibration", Journal of Fluids and Structures, **10**, 439-453.

Noca, F., Shiels, D. & Jeon, D. (1997), " Measuring instantaneous fluid dynamic forces on bodies, using only velocity fields and their derivatives", Journal of Fluids and Structures, **11**, 345-350.

Nuzzi, F. et al (1992), "Three dimensional vortex formation from an oscillating non-uniform cylinder ", Journal of Fluid Mechanics, **238**, 31-54.

Obasaju, E. D., Bearman, P. W. & Graham, J.M.R. (1988), " A study of forces, circulation and vortex patterns around a circular cylinder in oscillating flow", Journal of Fluid Mechanics, **196**, 467-494.

Olinger, D. J. & Sreenivasan, K.R. (1988), " Nonlinear dynamics of the wake of an oscillating cylinder", Physical Review Letters , **60**, 797-800.

Olinger, D.J., Alexandrou, A.N. and Dutka, J. (1993), " Vortex shedding lock-on in a periodic freestream flow past a circular cylinder", ASME Forum on Unsteady Flows, ed. Keith W. L. and Wei T. 157, 183-188.

Olinger, D.J., Alexandrou, A.N. and Keller, D.R. (1995), " Non-harmonic forcing of a cylinder wake by a periodic freestream flow", Proceeding of the 1995 Symposium on Fluid-Structure Interaction, ed. Coke, T.C. & Williams, D.R., 1995 ASME International Mechanical Engineering Congress & Exposition, San Francisco, CA, 41-52.

Olinger, D.J. (1998), "A low-order model for vortex shedding patterns behind vibrating flexible cables", Physics of Fluids, **10 (8),** 1953-1961.

Pankhurst, R.C. & Holder, D.W. (1952), <u>Wind Tunnel Technique</u>, Pitman, London, 327-427.

Parkinson, G.V. (1974), <u>Mathematical Models of Flow Induced Vibrations</u>, ed. E. Naudascher, 81-127, Berlin, Springer.

Pelletier, A. & Mueller, T. (2000), " Low Reynolds number aerodynamics of low aspect ration thin/flat/cambered plate wings", Journal of Aircraft, **37 (5),** 825-832.

Popp, K. (2000),<u>Experimental investigation of Reynolds number and scale effects on parachute inflation</u>, M.S. Thesis, Worcester Polytechnic Institute, Worcester, MA.

Prandtl, L. (1918), "Tragflugel Theorie", Nachrixhten von der Gesellschaft der Wisseschaften zu Gottingen, Geschaeftliche Mitteilungen, Klasse. 451-477.

Prandtl, L. (1921), "Applications of modern hydrodynamics to aeronautics", NACA 116.

Pritchard, J. Laurence (1958), "Francis Herbert Wenham, Honorary Member, 1824-1908; An Appreciation of the First Lecture to the Aeronautical Society", Journal of Royal Aeronautical Society, **62,** 571-596

Purutyan, H. (1990), <u>Ultrasonic Measurement of Circulation Around a Plunging Airfoil</u>, M. S. Thesis, Worcester Polytechnic Institute.

Rae, W. H. & Pope, A (1984), <u>Low-speed wind tunnel testing</u>, 2nd ed., Wiley, New York, 176-344.

Ramberg, S.E. & Griffin, O.M. (1976), "The effects of vortex coherence, spacing and circulation on flow-induced forces on vibrating cables and bluff structures", Naval Research Laboratory 7945.

Sarpkaya, T. (1975), " An inviscid model of two-dimensional vortex shedding for transient and asymptotically steady separated flow over an inclined plate", Journal of Fluid Mechanics, **68**, 109-128.

Sarpkaya, T. (1979), "Vortex induced oscillation", Journal of Applied Mechanics, **46**, 241-258.

Sarpkaya, T. & Isaacson, M. (1981) <u>Mechanics of Wave Forces on Offshore Structures</u>, Van Nostrand Reinhold Co.

Sarpkaya, T. (1986), "Force on a circular cylinder in viscous oscillatory flow at low Keulegan-Carpenter numbers", Journal of Fluid Mech. **165**, 61-71

Schlichting, H. (1979) <u>Aerodynamics of Airplane</u>, New York : McGraw-Hill

Schmidt, D.W. & Tilmann, P. M. (1970), " Experimental study of sound wave phase fluctuations caused by turbulent wakes", Journal of Acoustic Society, **47**, 1301-1324.

Schmidt, D.W. (1975), "Acoustic methods for fast detection and measurement of vortices in wind tunnel", ICIASF-75 Record, 216-228.

Smith, R. H., Durgin, W. W. & Johari, H. (1995), "The direct measurement of circulation in free surface vortices", AIAA paper 95-0104.

Stansby, P.K. (1974), "The effects of end plates on the base pressure coefficient of a circular cylinder", Aeronautical Journal,**78**, 36-37.

Surry, D. & Stathopoulos, T. (1997), " An experimental approach to the economical measurements of spatially averaged wind loads", Journal of Ind. Aerodynamics, **2**, 385-397.

Szepessy, S. & Bearman, P.W. (1993), "Analysis of a pressure averaging device for measuring aerodynamic forces on a circular cylinder", Experiments in Fluids, **16**, 120-128.

Tani, I. (1964), "Low-speed flows involving bubble separations", Progress in Aeronautical Science, 5, ed. Kuchemann D. & Sterne, L.H.G., Pergamon, New York, 70-103.

Theodorson, T. (1935), "General theory of aerodynamics instability and the mechanism of flutter", NACA Rep. 496.

Triantafyllou, G.S.(1990), "Three dimensional flow patterns in two dimensional wake", Proceeding of the ASME Symposium on Unsteady Flows, University of Toronto, Toronto, Canada, 395-.

Unal, M.F., Lin, J-C & Rockwell, D. (1997), " Force prediction by PIV imaging: A momentum-based approach", Journal of Fluids and Structures, **11**, 965-971.

Van Atta, C.W. & Gharib, M. (1987), "Ordered and chaotic vortex streets behind circular cylinders at low Reynolds numbers", Journal of Fluid Mechanics, **174**, 113-133.

Von Karman, T. & Sears, W.R. (1938), "Airfoil theory for non-uniform motion", Journal of Aeronautical Science, **5 (10),** 379-390

Wagner, H., (1925), "Über die Entstehüng des Dynamischen Aüftriebes von Tragflügeln", Zeitschrift für Angewandte Mathematik und Mechanik, **5 (1),** 17-35.

Walker, P. (1990), <u>The forces on a circular cylinder in oscillatory flow plus a current</u>, Ph.D. Thesis, Department of Aeronautics, Imperial College of Science and Technology, London, England.

Weber, F. J., Durgin, W. W. & Johari, H. (1995), "Direct circulation measurements about a rapidly pitching airfoil using an ultrasonic system", AIAA paper 95-2269.

Williamson, C.H.K. (1996), "Vortex dynamics in the cylinder wake", Ann. Rev., Fluid Mechanics, **28**, 477-.

Wu, J.C. (1981), " Theory for aerodynamic force and momentum in viscous flows", AIAA Journal, **19(4),** 432-441.

Wu, J. Z. et al. (1998), " Post-stall flow control on an airfoil by local unsteady forcing", Journal of Fluid Mechanics, **371**, 21-58.

Yuan, J. K. et al (1994), "The Corrected Investigation of Wall Interference on the Flow Field around Cylinders", ACTA AERODYNAMIC SINICA, Vol. 12, No.2, pp219-224, 1994.

Yuan, J.K. & Olinger, D.J.(1999), "An ultrasonic measurement technique for spatial lift distributions in bluff body flows", Proceeding of the 13th ACSE Engineering Mechanics, Fluid-Structure Interaction Sessions, Paper W1H-3, pp375. John Hopkins University, Baltimore, MD.

Yuan, J.K. & Olinger, D.J. (2002), "Circulation methods for unsteady aerodynamics flows", to appear in 20th AIAA Applied Aerodynamics Conference, Sessions of Unsteady Aerodynamics; St. Louis, June 24-27, AIAA-2002-3057.